©Copyright 2026
Riley Johnson

# Development of an Improved Model for Aeroelastic Response to Gust Excitation: MARGE-II

Riley Johnson

A thesis submitted in partial fulfillment of the requirements for the degree of

Master of Science in Aeronautics & Astronautics

University of Washington

2026

Reading Committee:

Kristi A. Morgansen, Chair

Eli Livne, Chair

Program Authorized to Offer Degree:
William E. Boeing Department of Aeronautics and Astronautics

University of Washington

## Abstract

Development of an Improved Model for Aeroelastic Response to Gust Excitation: MARGE-II

Riley Johnson

Co-Chairs of the Supervisory Committee:
Professor Kristi A. Morgansen
William E. Boeing Department of Aeronautics and Astronautics

Professor Eli Livne
William E. Boeing Department of Aeronautics and Astronautics

The Model for Aeroelastic Response to Gust Excitation II (MARGE-II) was developed to improve on the existing MARGE-I wind tunnel model's capabilities to demonstrate and evaluate active control techniques on a flexible aircraft model. The model has been designed for use in the University of Washington's 3' x 3' low-speed wind tunnel located adjacent to the Kirsten Wind Tunnel at the University of Washington. This thesis details the design and fabrication of the model as well as exploratory test results from a tunnel entry in the summer of 2025.

# TABLE OF CONTENTS

Page

List of Figures . . . . . ii

List of Tables . . . . . vi

Chapter 1: Introduction . . . . . 1
1.1 Aeroservoelastic Wind Tunnel Testing . . . . . 2
1.2 The History and State of the Art of Aeroservoelastic Wind Tunnel Testing . . . . . 2
1.3 MARGE-II Design Goals . . . . . 4

Chapter 2: Design and Fabrication . . . . . 6
2.1 Design Philosophy . . . . . 6
2.2 Structural Design . . . . . 6
2.3 Actuation and Instrumentation . . . . . 14
2.4 Model Control and Data Acquisition . . . . . 21

Chapter 3: Analysis and Initial Test Results . . . . . 27
3.1 Static Tests . . . . . 27
3.2 Wind Tunnel Entry 1 . . . . . 30
3.3 Next Steps . . . . . 90

Chapter 4: Conclusion . . . . . 93

Appendix A: Static Margin Calculations . . . . . 98

# LIST OF FIGURES


| Figure Number | | Page |
|---|---|---|
| 2.1 | Initial spar NASTRAN stress analysis | 7 |
| 2.2 | Major dimensions for base structure | 8 |
| 2.3 | Pitch-axis housing CAD cross-section view | 10 |
| 2.4 | Aeroshell assembly CAD | 11 |
| 2.5 | CAD view of aero shell components | 12 |
| 2.6 | CAD assembly side view | 13 |
| 2.7 | Control surface linkage | 14 |
| 2.8 | Predicted structural mode shapes | 16 |
| 2.9 | MARGE-II in 3x3 wind tunnel CAD model | 17 |
| 2.10 | Full assembly CAD isometric view | 18 |
| 2.11 | Wind tunnel mounting bracket as installed | 19 |
| 2.12 | Servo response test results | 20 |
| 2.13 | Installed servo motor | 21 |
| 2.14 | Sensor locations | 23 |
| 2.15 | Hall effect sensor installed in mount | 24 |
| 2.16 | Installed wingtip accelerometer | 25 |
| 2.17 | MARGE-II control system | 25 |
| 2.18 | MARGE-II data acquisition system | 26 |
| 3.1 | Structural test setup | 28 |
| 3.2 | FFT from wing spar impulse response data | 29 |
| 3.3 | FFT from tail impulse response data | 29 |
| 3.4 | Pitch instability demonstrated | 31 |
| 3.5 | MARGE-II Assembly Aerodynamic Dimensions | 32 |
| 3.6 | 250 Pa elevator sweep 0-25 Hz position vs command data | 34 |
| 3.7 | 250 Pa elevator sweep 0-25 Hz strain gauge data | 35 |
| 3.8 | 250 Pa elevator sweep 0-25 Hz tail accelerometer data | 36 |

3.9 250 Pa elevator sweep 0-25 Hz forward wingtip accelerometer data . . 36
3.10 250 Pa elevator sweep 0-25 Hz aft wingtip accelerometer data . . . . 37
3.11 250 Pa elevator sweep 0-25 Hz pitch data . . . . . 38
3.12 250 Pa elevator sweep 0-25 Hz mid-fuselage strain gauge coherence FRF estimate . . . . . 39
3.13 250 Pa elevator sweep 0-25 Hz mid-fuselage strain gauge gain FRF estimate . . . . . 40
3.14 250 Pa elevator sweep 0-25 Hz mid-fuselage strain gauge phase FRF estimate . . . . . 41
3.15 250 Pa elevator sweep 0-25 Hz mid-wing strain gauge coherence FRF estimate . . . . . 42
3.16 250 Pa elevator sweep 0-25 Hz mid-wing strain gauge gain FRF estimate 43
3.17 250 Pa elevator sweep 0-25 Hz mid-wing strain gauge phase FRF estimate 44
3.18 250 Pa elevator sweep 0-25 Hz forward wing tip accelerometer coherence FRF estimate . . . . . 45
3.19 250 Pa elevator sweep 0-25 Hz forward wing tip accelerometer gain FRF estimate . . . . . 46
3.20 250 Pa elevator sweep 0-25 Hz forward wing tip accelerometer phase FRF estimate . . . . . 47
3.21 250 Pa elevator sweep 0-25 Hz aft wing tip accelerometer coherence FRF estimate . . . . . 48
3.22 250 Pa elevator sweep 0-25 Hz aft wing tip accelerometer gain FRF estimate . . . . . 49
3.23 250 Pa elevator sweep 0-25 Hz aft wing tip accelerometer phase FRF estimate . . . . . 50
3.24 250 Pa elevator sweep 0-25 Hz tail accelerometer coherence FRF estimate 51
3.25 250 Pa elevator sweep 0-25 Hz tail accelerometer gain FRF estimate . 52
3.26 250 Pa elevator sweep 0-25 Hz tail accelerometer phase FRF estimate 53
3.27 250 Pa elevator sweep 0-25 Hz Hall-Effect (pitch) coherence FRF estimate 54
3.28 250 Pa elevator sweep 0-25 Hz Hall-Effect (pitch) gain FRF estimate 55
3.29 250 Pa elevator sweep 0-25 Hz Hall-Effect (pitch) phase FRF estimate 56
3.30 250 Pa elevator sweep 0-25 Hz aft fuselage strain gauge power spectral density . . . . . 57
3.31 250 Pa elevator sweep 0-25 Hz mid-wing strain gauge power spectral density . . . . . 58

3.32 250 Pa elevator sweep 0-25 Hz forward wingtip accelerometer power spectral density . . . . . 59
3.33 250 Pa elevator sweep 0-25 Hz aft wingtip accelerometer power spectral density . . . . . 60
3.34 250 Pa elevator sweep 0-25 Hz tail accelerometer power spectral density 61
3.35 250Pa elevator sweep 0-25Hz Hall-Effect power spectral density . . . 61
3.36 250 Pa outboard aileron sweep 0-25 Hz input data . . . . . 62
3.37 250 Pa outboard aileron sweep 0-25 Hz strain gauge data . . . . . 63
3.38 250 Pa outboard aileron sweep 0-25 Hz forward wingtip accelerometer data . . . . . 63
3.39 250 Pa outboard aileron sweep 0-25 Hz aft wingtip accelerometer data 64
3.40 250 Pa outboard aileron sweep 0-25 Hz tail accelerometer data . . . . 65
3.41 250 Pa outboard aileron sweep 0-25 Hz mid-wing strain gauge FRF coherence estimate . . . . . 66
3.42 250 Pa outboard aileron sweep 0-25 Hz mid-wing strain gauge FRF gain estimate . . . . . 67
3.43 250 Pa outboard aileron sweep 0-25 Hz mid-wing strain gauge FRF phase estimate . . . . . 68
3.44 250 Pa outboard aileron sweep 0-25 Hz aft fuselage strain gauge FRF coherence estimate . . . . . 69
3.45 250 Pa outboard aileron sweep 0-25 Hz aft fuselage strain gauge FRF gain estimate . . . . . 70
3.46 250 Pa outboard aileron sweep 0-25 Hz forward wingtip accelerometer FRF coherence estimate . . . . . 71
3.47 250 Pa outboard aileron sweep 0-25 Hz forward wingtip accelerometer FRF gain estimate . . . . . 72
3.48 250 Pa outboard aileron sweep 0-25 Hz forward wingtip accelerometer FRF phase estimate . . . . . 73
3.49 250 Pa outboard aileron sweep 0-25 Hz aft wingtip accelerometer FRF coherence estimate . . . . . 74
3.50 250 Pa outboard aileron sweep 0-25 Hz aft wingtip accelerometer FRF gain estimate . . . . . 75
3.51 250 Pa outboard aileron sweep 0-25 Hz aft wingtip accelerometer FRF phase estimate . . . . . 76

3.52 250 Pa outboard aileron sweep 0-25 Hz tail accelerometer FRF coherence estimate . . . 77
3.53 250 Pa outboard aileron sweep 0-25 Hz tail accelerometer FRF gain estimate . . . 78
3.54 250 Pa outboard aileron sweep 0-25 Hz tail accelerometer FRF phase estimate . . . 79
3.55 250 Pa outboard aileron sweep 0-25 Hz pitch FRF coherence estimate 80
3.56 250 Pa outboard aileron sweep 0-25 Hz pitch FRF gain estimate . . . 81
3.57 250 Pa outboard aileron sweep 0-25 Hz pitch FRF phase estimate . . 82
3.58 250 Pa outboard aileron sweep 0-25 Hz mid-wing strain gauge power spectral density . . . 83
3.59 250 Pa outboard aileron sweep 0-25 Hz aft fuselage strain gauge power spectral density . . . 84
3.60 250 Pa outboard aileron sweep 0-25 Hz mid-fuselage strain gauge power spectral density . . . 85
3.61 250 Pa outboard aileron sweep 0-25 Hz forward wingtip accelerometer power spectral density . . . 86
3.62 250 Pa outboard aileron sweep 0-25 Hz aft wingtip accelerometer power spectral density . . . 87
3.63 250 Pa outboard aileron sweep 0-25 Hz tail accelerometer power spectral density . . . 88
3.64 250 Pa outboard aileron sweep 0-25 Hz Hall-Effect sensor power spectral density . . . 89
3.65 MARGE-II with updated sensor locations . . . 91
3.66 MARGE-II in 3x3 wind tunnel with updates . . . 92
A.1 MARGE-II Assembly Aerodynamic Dimensions . . . 99

# LIST OF TABLES


Table Number Page

2.1 Structural mode predicted frequencies . . . . . 15
2.2 Sensor instrumentation and placement . . . . . 22
3.1 Structural mode measured vs predicted frequencies . . . . . 30

# ACKNOWLEDGMENTS

This work would not have been possible without the help of my fellow students, John Berg, Eddie Ting, Alex LaFranchi, and Barkin Sarigöl. A special thanks to Dr. Kristi Morgansen and Dr. Eli Livne, whose patience enabled the project's completion.

And of course thank you, Lizzy. You're the best.

# Chapter 1
# INTRODUCTION

Advances in aeroelastic optimization technology and composites have led the aviation industry to develop aircraft with increasingly flexible structures. Such aircraft often exhibit tightly coupled rigid-body and elastic dynamics and additional nonlinearities in structural, aerodynamic, and actuation analysis. Improved sensing and actuation capabilities along with new developments in control law synthesis and ever-expanding computing capacity all contribute to active controllers' capability to impact aircraft response to aeroelastic excitation. Notwithstanding the continued development of computer modeling and simulation of aeroelastic systems, some degree of experimental validation is almost always required to evaluate aeroelastic control systems. In the case of new configurations, active aeroelastic control tests in the wind tunnel provide physical insights and can be used to guide fine-tuning of mathematical models and as risk reduction tests before more expensive wind tunnel tests and flight tests would follow.

Full scale flight testing of new control systems is prohibitively expensive while scaled down flight tests of research unmanned aerial vehicles (UAVs) encounter issues with scaling, repeatability, hardware sizing, and high risks. Wind tunnel testing offers a controlled and repeatable environment for the development of active aeroelastic control systems. However, wind tunnel testing generally relies on precisely scaled and tuned aeroelastic test models that are often still expensive, complex, and fragile.

The original MARGE-I system developed at the University of Washington offered a small-scale low-cost test bed for aeroelastic control testing in an effort to fill this need [1, 2, 3, 4, 5, 6, 7, 8]. The new system described in this thesis, MARGE-II,

was developed as an improvement on MARGE-I, with an eye toward improving the structural characteristics, actuation and sensing capabilities, and simplicity of design of the original.

### *1.1 Aeroservoelastic Wind Tunnel Testing*

Wind tunnel testing is a critical element in the development of active control technologies. Despite significant advances in mathematical modeling of aeroelastic systems, including important advances in CFD, real-world data is critical for the validation of mathematical models. Wind tunnel testing is both the lowest cost and most repeatable way to validate mathematical models. Wind tunnels provide a controlled test environment with access, in general, to more sensing and actuation options than flight tests of the full-size vehicle. In the case of active flutter suppression, wind tunnel tests also provide a testing environment that is safer than flight tests.

Challenges of wind tunnel testing include limitations in their ability to duplicate Mach, to duplicate Reynolds Number, and for proper scaling of full size test articles. The effects of wind tunnel walls and mounting equipment can also introduce interference that can make the application of wind tunnel test results to full scale models difficult. In the case of aeroelastic testing, wind tunnel testing struggles to recreate free-free coupled aeroservoelastic behavior without highly complex model mounting systems.

### *1.2 The History and State of the Art of Aeroservoelastic Wind Tunnel Testing*

The University of Washington has a rich history of wind tunnel testing in both the Kirsten Wind Tunnel and the 3' x 3' wind tunnel. The Kirsten Wind Tunnel, used by Boeing for flutter tests of aircraft for years, hosted testing for Boeing's Solar Eagle (Vulture) wing in the early 2010s which aimed to model a highly elastic nonlinear wing structure.

Tests of simplified tail/rudder systems that focused on damaged composite structures, freeplay, and the effects of damaged actuators were carried out in the 3' x 3' tunnel in the years 2008-2015 as a first step in the development of aeroelastic/aeroservoelastic capabilities in this tunnel [9, 10, 11].

In recent years, MARGE-I [1, 2, 3, 4, 5, 6, 7, 8] has been used to great effect as a low-cost, fast way to test and develop active control capability. The University team also developed the Large Flexible Wing (LFW)[12, 13, 14] for use in the Kirsten Wind Tunnel - the fourth in a series of iterated test articles developed in collaboration with NASA.

For a thorough review of major aeroservoelastic wind tunnel test programs up to 2017, see references 154-157 and 562-623 in [15]. New wind tunnel systems have been developed since the publication of [15]. New materials and manufacturing technologies combined with advances in sensing, actuation, and computational hardware have made low-cost aeroservoelastic wind tunnel models more affordable. They are now within reach for universities and research organizations. At the same time, the development and tests of larger and more expensive wind tunnel models have continued [16], including models that would allow tests in the transonic and supersonic regimes and carry large arrays of control effectors and sensors [17, 18].

With all of MARGE-I's success as a very low-cost accessible test platform, there were some areas of desired improvement. MARGE-I's primary low-frequency structural modes were found at 1.4 Hz and 10.3 Hz, with a fuselage bending mode at around 3 Hz. The actuators used to drive MARGE-I's control surfaces had effective bandwidth up to only around 4 Hz. This bandwidth mismatch leads to difficulties in controlling structural modes, especially ones that are flutter-related, as the system cannot affect modes higher than the 4 Hz servo bandwidth. MARGE-I also had some initial issues with freeplay in the control system actuation. Combined with a lack of direct positional measurement on the control surfaces, this freeplay created uncertainty in control surface position, which made analysis difficult. MARGE-I was

further limited by sensing capacity: it used strain gauges at the base of the fuselage and wing connection, combined with a hall-effect sensor for pitch measurement, and accelerometers on the leading and trailing edge of its tip mass. This sensor arrangement lacked the ability to observe all of the modal activity of the test article, including the fuselage bending and twist modes.

### *1.3 MARGE-II Design Goals*

MARGE-II was designed as a direct improvement on MARGE-I. The configuration was to remain the same, with the exception of adding an additional control surface to the wing which enhances the capability of the model to use more complex active controllers. Structurally, the goal of MARGE-II was to include three structural modes that could be excited or controlled within the bandwidth of the actuators. The first requirement became control surface bandwidth of 10 Hz. The structural design requirements followed: three structural modes below 10 Hz, aiming for a short period mode under 1 Hz, first wing bending around 2 Hz, first wing torsion around 10 Hz, and first fuselage bending around 7 Hz. The specific modal frequencies targeted were accompanied by structural integrity constraints, which were defined as a maximum stress of 67% material yield, with a maximum strain below 3% over the range of angles of attack and dynamic pressures of likely wind tunnel test plans.

Expanding sensing capabilities of the model was another priority in the design of the MARGE-II test article. Work that had been done on the sensing scheme used in MARGE-I contributed to the development of the Large Flexible Wing. This sensing architecture was repurposed for MARGE-II, which allowed expansion of the number of sensors available to 15. The Hall-Effect pitch angle sensing capability was retained, as well as the wingtip accelerometers and root strain gauges for both the wing spar and fuselage. Added to these were additional strain gauges in the middle of the fuselage, at the root in a chordwise orientation on the wing, and span wise in the mid-wing. Potentiometers measuring control surface position for all four control

surfaces and a tail accelerometer were also added. Additional desired sensors were a pitch rate gyro and airspeed sensor to compliment the hall effect sensor data and the wind tunnel's built in airspeed sensor. An important consideration was the desire to significantly increase the quality and capability of the accelerometers from those found on the wing tips of MARGE-I. Along with the expanded sensor suite, MARGE-II's design presented an opportunity to implement lessons learned from MARGE-I and the University of Washington's Large Flexible Wing about anti-aliasing and sensor shielding in the 3' x 3' wind tunnel.

The remainder of the thesis is organized as follows. The design and fabrication of the MARGE-II wind tunnel model will be detailed in Chapter 2 including the structural design, actuator selection, and instrumentation of the model. The model's control and data acquisition systems are then described along with preliminary Ground Vibration Test results and predicted modal characteristics obtained through Finite Element Analysis. In Chapter 3 wind tunnel results from week 1 of the exploratory wind tunnel entry are presented, with lessons learned from the initial shakedown tests, and the next steps taken by the MARGE-II team are described. The thesis concludes in Chapter 4 with a summary and thoughts on future work.

# Chapter 2
# DESIGN AND FABRICATION

## *2.1 Design Philosophy*

The design philosophy of MARGE-II was to build on the success of MARGE-I, increasing the model's structural, actuation, and sensing capabilities while simultaneously simplifying the build (and rebuild) process. Efforts were made to use off-the-shelf parts for the structural build as well as for the sensor suite. One of the biggest strengths of this platform is its low-cost nature both to build and to operate, and its simple design, which allows for rapid changes as desired.

## *2.2 Structural Design*

### *2.2.1 Structural Components*

The structure of MARGE-II is largely similar to MARGE-I, with the aim of making incremental improvements where possible. The principal load-carrying elements of MARGE-II are an aluminum wing beam and a steel fuselage beam. The other main structural components are a cylindrical tip mass attached to the end of the wing beam and a short aluminum tail beam. The wing beam is a plate with holes for the installation of actuators, enabling actuators to sit inside the outer mold line of the wing without bulging out of it.

Sizing these components required consideration of structural modal frequencies, structural loads, and geometric constraints imposed by both the wind tunnel and the actuators used in the final model. Sizing began by considering standard aluminum bar stock sizing for the wing beam. Initially, continuing with the same 1/16" thickness of MARGE-I's wing spar was evaluated, but meeting the stress requirements became

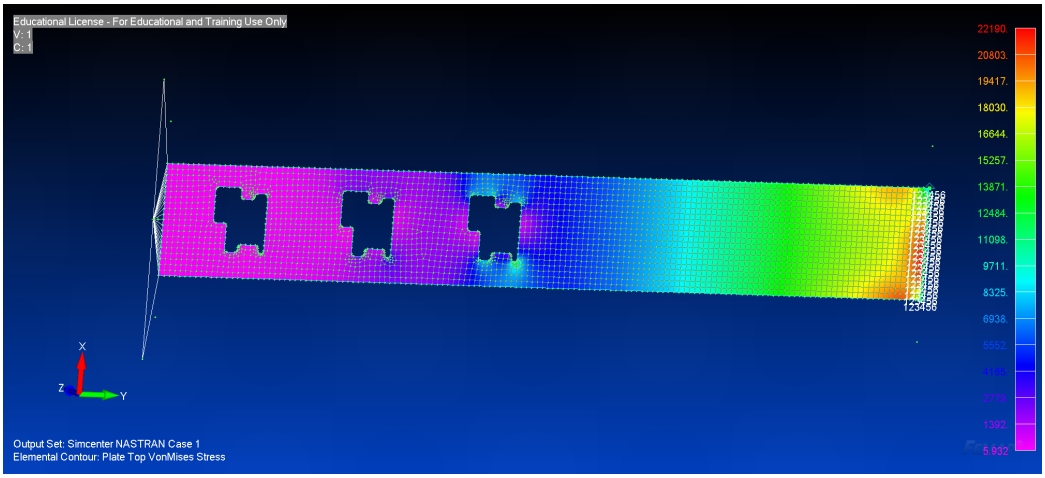



Figure 2.1: Initial spar NASTRAN stress analysis

a challenge. The spar was analyzed in Nastran (see Figure 2.1), with load conditions determined by an initial aero trim at an airspeed of $V = 35$ m/s which is equivalent to a dynamic pressure of $q = 15.67$ psf, at an angle of attack of 10 degrees.

Based on this initial analysis, it was decided that a spar thickness of 1/8" would be the right minimum thickness, as limited by stress considerations.

The beam width was limited by actuator size. Actuator selection is discussed later in this thesis. MARGE-I used hobby helicopter servo motors due to their very low profile. These actuators did not have sufficient frequency bandwidth to excite the desired modal frequencies, so MARGE-II needed higher performance larger servo motors. In order to mount these servo motors inside the aerodynamic shells, the servo motors had to be housed inside cutouts in the wing spar. Spar thickness was selected to accommodate the actuators as well as to provide space to mount the aerodynamic shells. A width of 4" was selected as it was available as a standard off-the-shelf width while meeting actuator sizing requirements.

From there, the fuselage beam was sized to match the 1/8" thickness of the spar for ease of construction. The length of the fuselage was determined by matching the

planform of the MARGE-I configuration. The fuselage was scaled up in proportion to the wingspan increase. Because neither stress due to aerodynamic load nor modal frequency were concerns for the tail spar, it too was sized by scaling relative to the wingspan increase from MARGE-I in the spanwise direction and by actuator sizing requirements in the width direction. The scaling considerations yielded a 5" tail spar length with the off-the-shelf standard size 4" width common to the wing spar (see Figure 2.2).

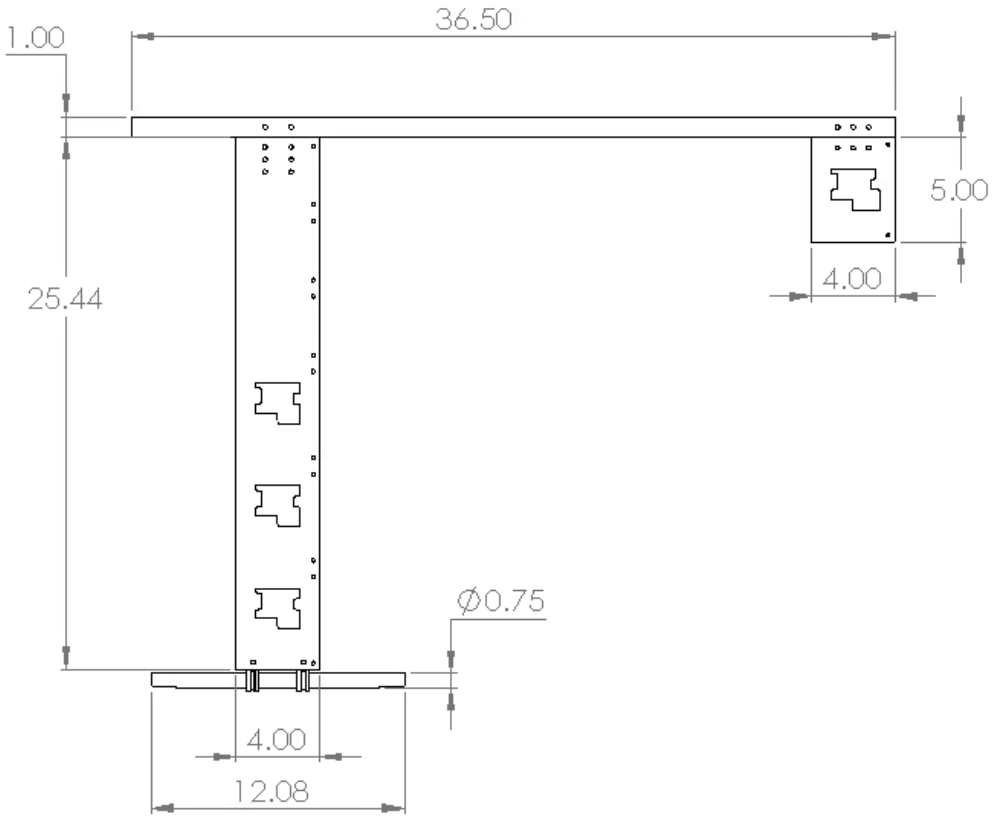



Figure 2.2: Major dimensions for base structure

### *2.2.2 Hanging Subassembly*

MARGE-II is suspended from the wind tunnel in the same manner as MARGE-I: a long U-channel is fixed to the roof of the wind tunnel, to which is bolted a housing containing a pivot mechanism for the model, via a hole pattern machined in the bottom of the U-channel used to affix the pitch axis housing. MARGE-II uses a precision machined shoulder bolt, which is supported by a bearing assembly contained in a solid pitch axis housing, to support the weight of the model. The shoulder bolt is threaded onto another solid aluminum block from which MARGE-II is suspended. To mitigate some of the freeplay present in MARGE-I, the housing supporting the model was machined out of a solid aluminum block, instead of 3D printed plastic. This housing includes two press-fit ceramic bearings spaced as far apart as space would allow in the U-channel. The precision machined shoulder bolt also serves as the pitch axis for MARGE-II. It rests on washers that sandwich a thrust bearing, allowing for free rotation about the model's pitch axis. Freeplay is limited by tight tolerances between the inner diameter of the press-fit bearings and the shoulder bolt's outer diameter. The material choices and design of the pitch axis housing reduce freeplay in the model's yaw direction by limiting plastic deformation of the housing. The freeplay and travel in the yaw direction is further reduced by spacing the support bearings farther apart than their counterparts in MARGE-I (see Figure 2.3). The shoulder bolt is threaded onto another machined aluminum block from which the structure of MARGE-II is suspended.

### *2.2.3 Aerodynamic Sections*

The aerodynamic sections are comprised of two 3D printed pieces designed to attach to the wing spar with minimum contact points and to attach to each other in a clamshell format that enables ease of access to the spar. The initial goal was to maintain the same NACA 0012 airfoil shape used on MARGE-I, but maintaining

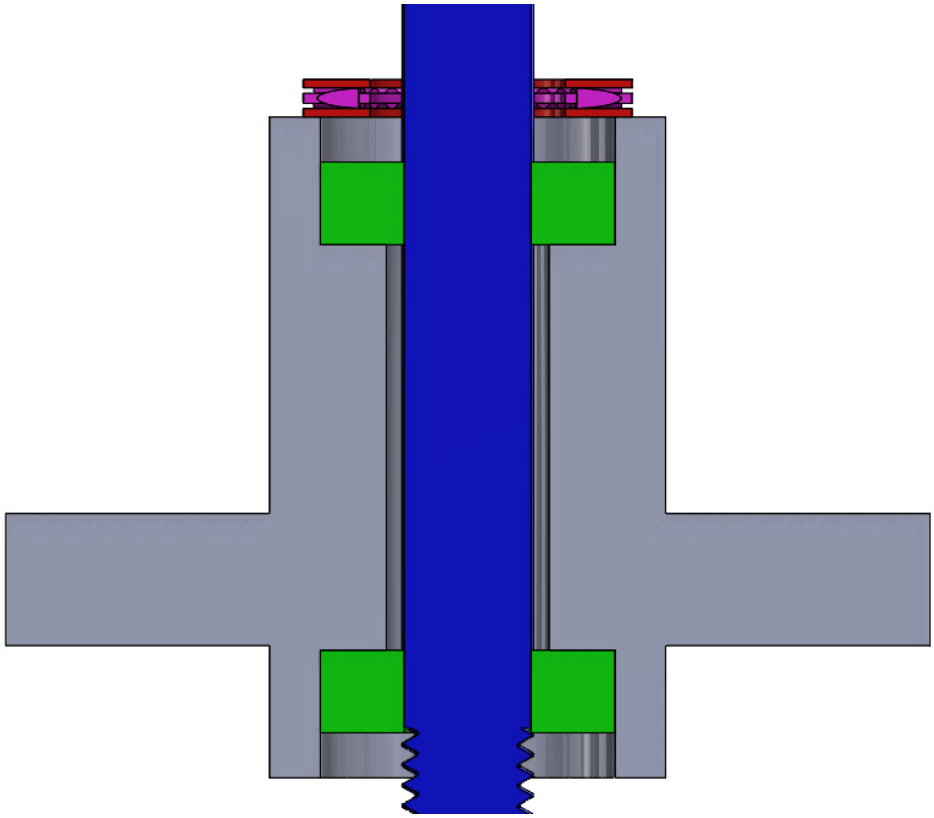


Figure 2.3: Pitch-axis housing CAD cross-section view

the same airfoil shape would have required a 30% increase in chord length, which represents too large of a change in aspect ratio compared to MARGE-I. A NACA 0015 airfoil was selected to increase the space within the airfoil to accommodate the actuators while only increasing the chord relative to MARGE-I by 25% (Figure 2.4). A symmetric airfoil was selected for simplicity and because particular lift characteristics were secondary to structural modal frequency concerns for this model. NACA airfoils are well understood and are sufficient for the goals of MARGE-II. There are three aero shells without control surfaces, equally divided along the span between the innermost control surface and the end of the spar, with a small gap between each aero shell to allow the wing beam to flex with minimal interference to minimize effects on structural stiffness from the aero shells.

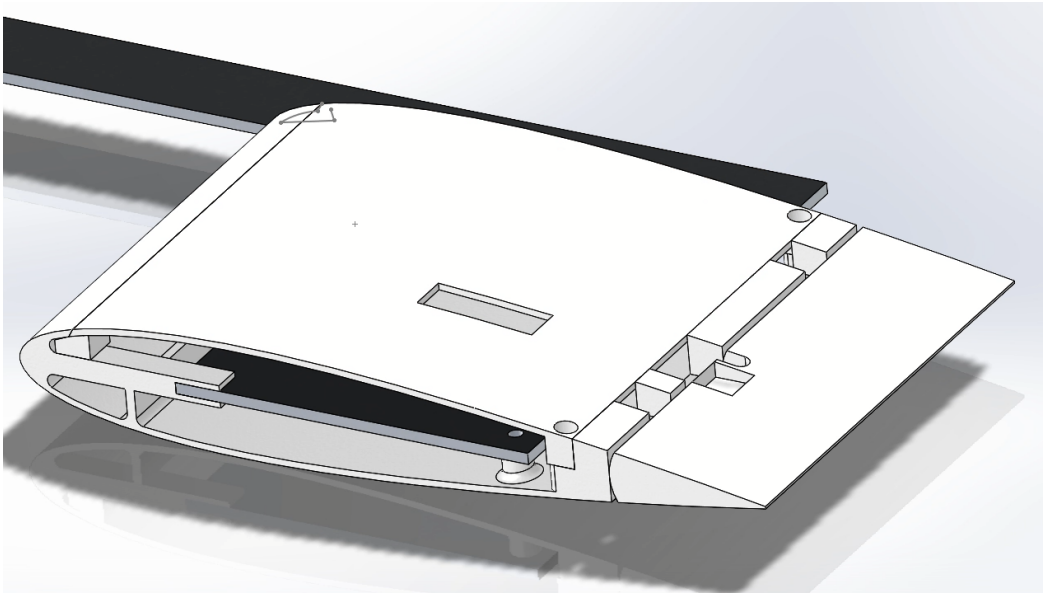


Figure 2.4: Aeroshell assembly CAD

### *2.2.4 Control Surfaces*

There are three control surfaces along the wing trailing edge and one on the tail's trailing edge. The control surfaces were sized at 25% of the chord length with dimensions originally selected so that the three active control surfaces made up half of the wing span. As will be explained later, the original spar was 29 inches long, but had to be trimmed to 25.44 inches in length due to wind tunnel sizing oversights during the design process. Each control surface ended up measuring 4.45 inches spanwise. The surfaces themselves are 3D printed with 100% infill, designed as an extrusion of the trailing edge quarter of a NACA 0015 airfoil, with a fillet on the inside edge to allow for pivoting. The trailing edge is attached to the main aero shell section with two hinges which are super-glued into slots in the control surface, and bolted into the main body of the aero shell (Figure 2.5). The left image shows the bottom clamshell element of the aero shell, which clips onto the wing spar at the leading edge and is further secured with two bolts through the wing spar via heat inserts into the

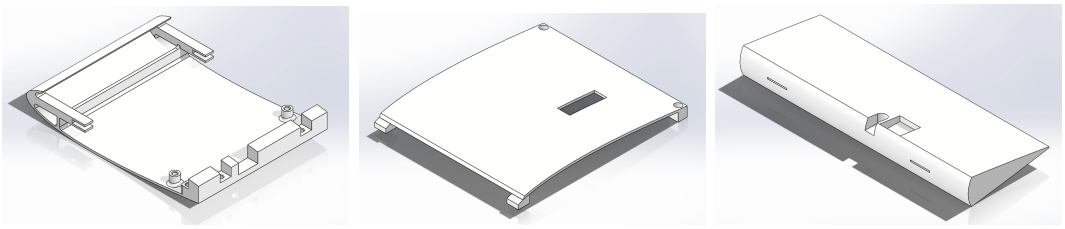


Figure 2.5: CAD view of aero shell components

printed posts from the bottom skin of the aero shell. The center image is the top clamshell element of the aero shell, which has protrusions that fit under the lip for the bottom aero shell at the leading edge, while the trailing edge is secured to the bottom clamshell element again via bolts into heat inserts set into the bottom clamshell element. The right image is a newer control surface design, which has a recessed square where a separate control horn can be attached, which is updated from the version of the control surfaces on the model at the time of testing. Figure 2.6 depicts a CAD assembly of MARGE-II with some of the top clamshell elements removed, to illustrate the ease of access to the model's interior granted by the clamshell assembly design.

The control surfaces include built-in control horns printed as part of the structure. These are linked to the spar-mounted servo motors with a threaded rod and hobby aircraft control horn components which are adjustable and tightened with Loctite (Figure 2.7). The goal was to eliminate as much freeplay as possible in the control surface linkage setup. While an improvement on the original MARGE-I linkages, MARGE-II still ended up with some freeplay in the control surface linkage setup.

### *2.2.5 Initial Modal Analysis*

To guide the development of MARGE-II so that more low-frequency modes would be within the frequency bandwidth of the actuators, NASTRAN Finite Element Analysis

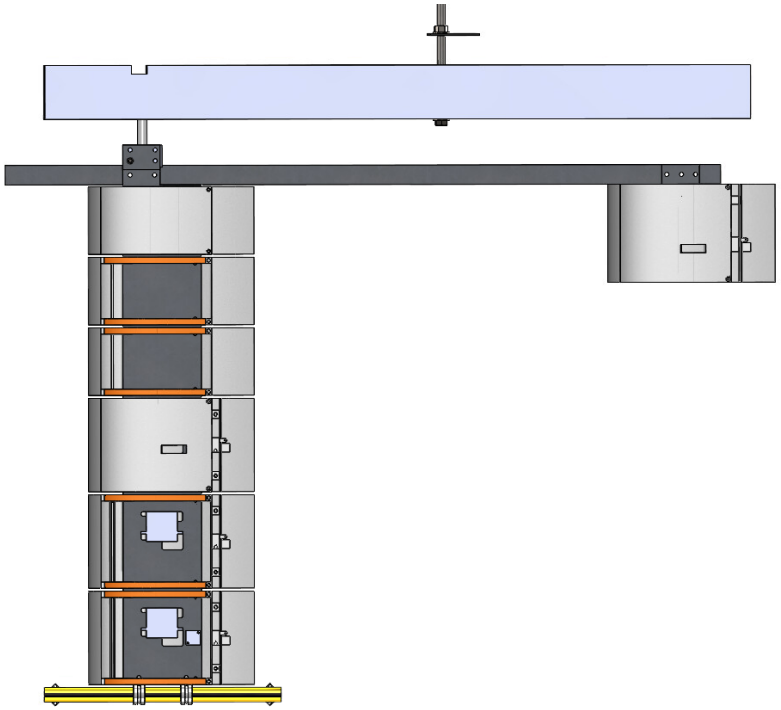


Figure 2.6: CAD assembly side view

was used to study key design features and their effects.[1] The CAD design of the system (in Solidworks) was transferred into NASTRAN. Initial modal analysis results for the final design, as represented by the CAD model, are shown in Table 2.1 and Figure 2.8. These are, of course, not the actual final modal characteristics of the system. The system was analyzed as being fixed at the pivot point, while the finished article can freely rotate in the pitch direction. This early analysis provides enough structural information to be useful, with the mode shapes and frequencies involving fuselage bending being most affected by the attachment point modeling. The mode shapes behaved as expected, with low-frequency wing and fuselage bending modes below 20 Hz. The 11.7 Hz in-plane fuselage bending mode was not of aeroelastic interest, however, and thus was not instrumented for controllability or observability.

[1]The FE analysis was carried out at the very early design stages by Dr. Marat Mor and later by Barkin Sarigöl. See acknowledgment at the end of the thesis.

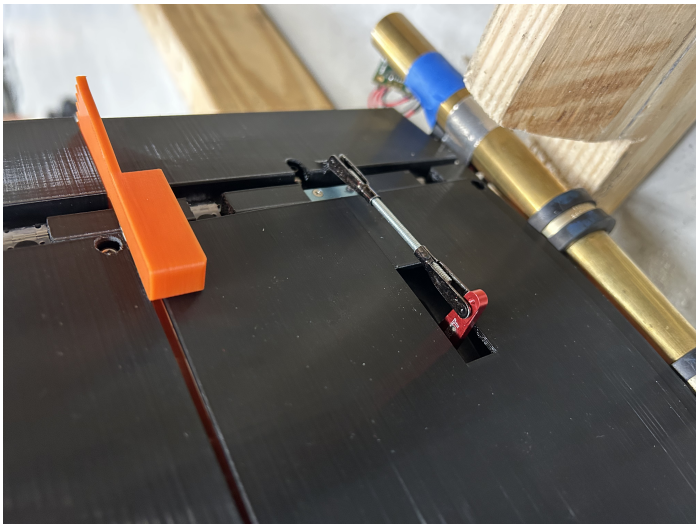


Figure 2.7: Control surface linkage

### *2.2.6 Wind Tunnel Installation and Support*

The model is installed in the wind tunnel in the same manner as MARGE-I (see Figure 2.9): an aluminum U-channel at the top of the model is sandwiched between two plates which are bolted together through an opening in the tunnel's upper plate (see Figures 2.11 and 2.10)). All of the wiring for the model also passes through this opening.

## ***2.3 Actuation and Instrumentation***

### *2.3.1 Actuator Selection*

One of the major differences in MARGE-II's capability as compared to MARGE-I is the selection of more powerful, higher-bandwidth actuators. MARGE-I used the lowest profile servos available, and this led to deficiencies in the frequency range over which the actuators could excite the model, resulting in limits to which flutter modes were accessible for control. MARGE-II uses the next largest standard size of servo motor. There were several servos of different makes and models in stock from use

Table 2.1: Structural mode predicted frequencies

| Mode | Frequency |
|---|---|
| First Wing Bending | 2.3Hz |
| First Fuselage Bending | 6.4Hz |
| In-Plane Fuselage Bending | 11.7Hz |
| First Fuselage Torsion | 15.4Hz |
| Second Wing Bending | 17.3Hz |

in the Large Flexible Wing project, all of which had been found to provide a -3db bandwidth of at least 10Hz in testing performed for the LFW by John Berg and Eddie Ting in 2022. Futaba servos were chosen from the available selection and were installed on MARGE-II.

As model shakedown testing was performed, it was discovered that the Futaba servos exhibit some undesired freeplay when the model is completely assembled. In Figure 2.12, the installed servos are represented as baseline data in dark blue. Figure 2.12 shows a set of tests performed by Alex LaFranchi and Barkin Sarigöl that show that the Savox servos outperformed the Futaba servos installed in the model and replaced the Futaba servos in future tests. This thesis details the build and testing of MARGE-II through week 1 of the first wind tunnel entry in June 2025. The servos were replaced in September 2025.

### *2.3.2 Actuator Mounting*

A key struggle in the physical design process for MARGE-II was mounting the actuators. The limiting factor for MARGE I's actuator selection was sizing - in order to improve actuator performance, there was no way to achieve the necessary effective bandwidth without stepping up the servo size significantly. Mounting these servos on

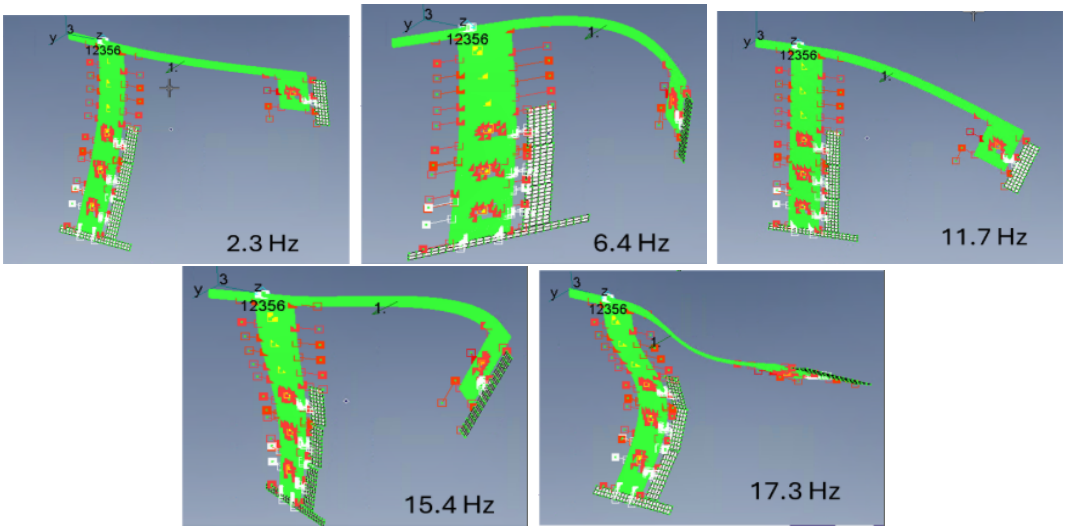



Figure 2.8: Predicted structural mode shapes

top of the wing spar was not possible without drastically increasing the airfoil's thickness, which would create aspect ratio problems for the model. The solution was to cut out holes in the wing spar that could tightly fit the servos and to bond aluminum mounting blocks onto the spar with epoxy so the servo's native hardware attachment points could still be utilized (Figure 2.13). Concerns that cutouts in the spar would lead to problems meeting stress requirements were resolved in the initial structural loading analysis shown in Section 2.2.1.

### *2.3.3 Sensors*

MARGE-II is equipped with a similar data acquisition system to that of the LARGE wing, resulting in expanded capacity of 15 channels for sensor inputs when compared to MARGE-I. The sensors and their locations are detailed in Table 2.2 and shown in Figure 2.14.

All of the sensors on MARGE-II are powered via a custom power distribution board contained in the electronics enclosure, fed by an external power supply. The power distribution board receives ±15V from the external power supply, and reduces

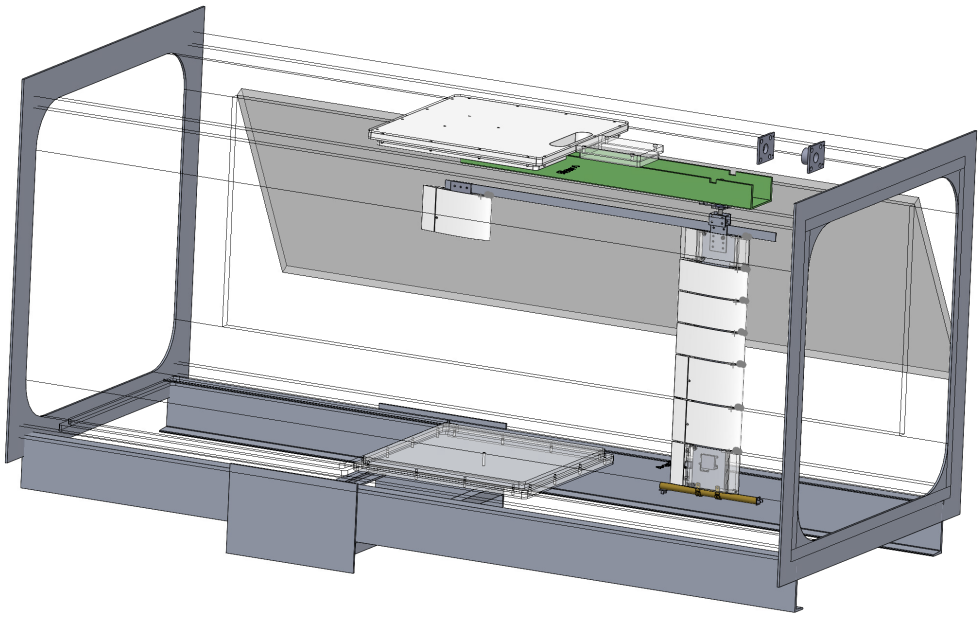


Figure 2.9: MARGE-II in 3x3 wind tunnel CAD model

to the output voltage needed for the various sensors.

This expanded sensor set was chosen to improve on the capabilities of MARGE-I. As noted in the Design Goals section, MARGE-II adds direct measurement of control surface position which enables the model to more accurately command and measure surface position. The expanded number of strain gauges alongside one additional accelerometer, with the improved quality of accelerometers, allows MARGE-II to more accurately measure modal activity of the model. The Hall-Effect sensor and laser vibrometer are unchanged from MARGE-I and are used to measure the model's angle of attack and position of the gust vanes, respectively. Improvements were made in the installation and calibration of the Hall Effect Sensor, improving its reliability from MARGE-I despite being the same sensor (Figure 2.15).

Another sensing advantage MARGE-II has over MARGE-I is derived from its geometry - the longer wingspan and fuselage, as well as the longer wing tip mass, all

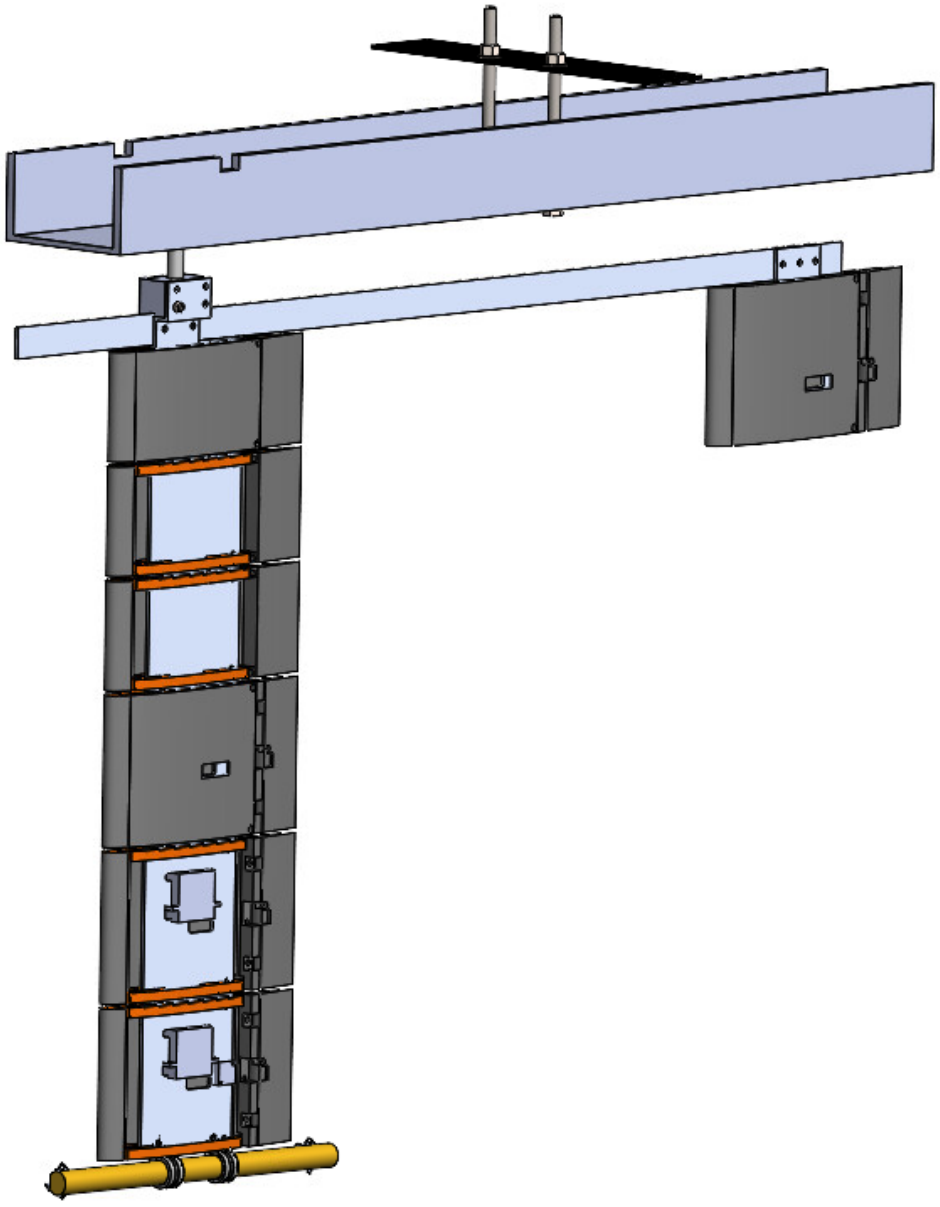


Figure 2.10: Full assembly CAD isometric view

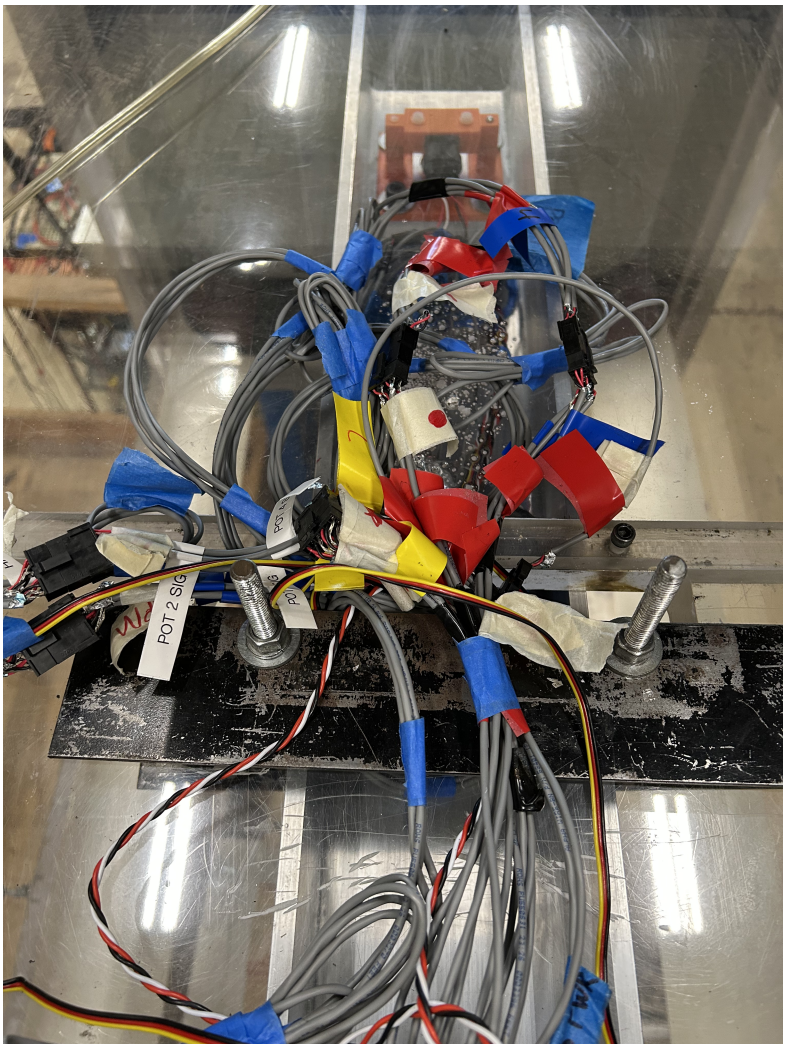



Figure 2.11: Wind tunnel mounting bracket as installed

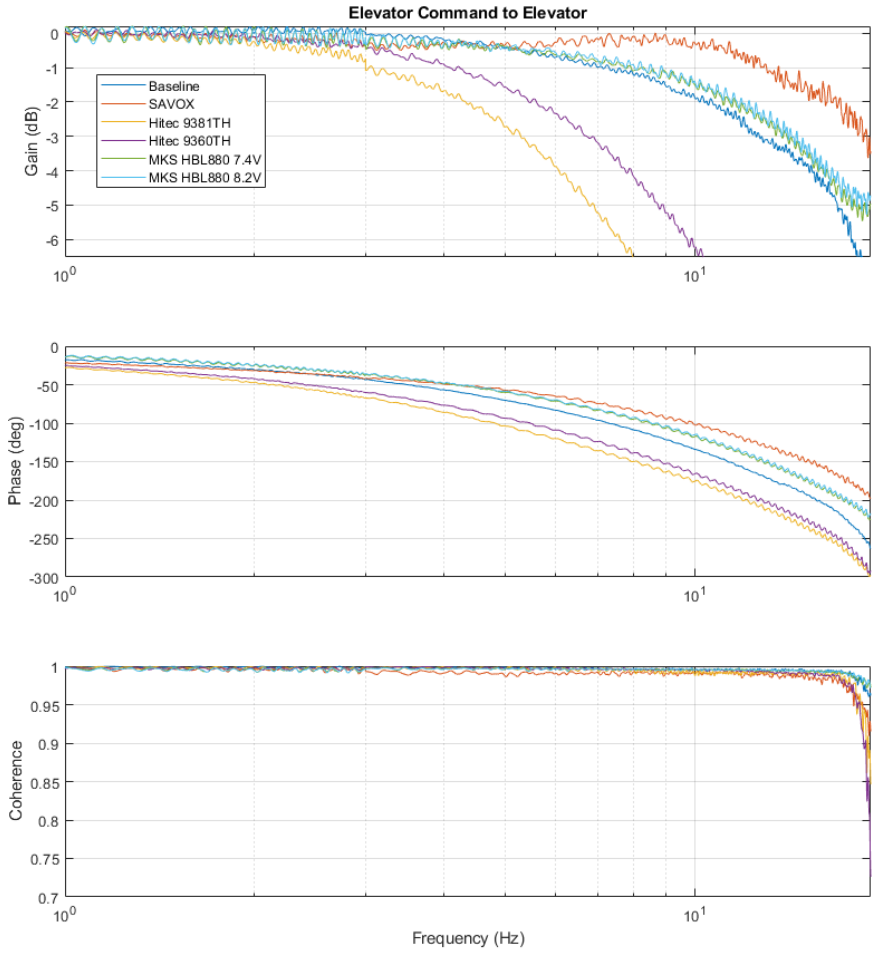



Figure 2.12: Servo response test results

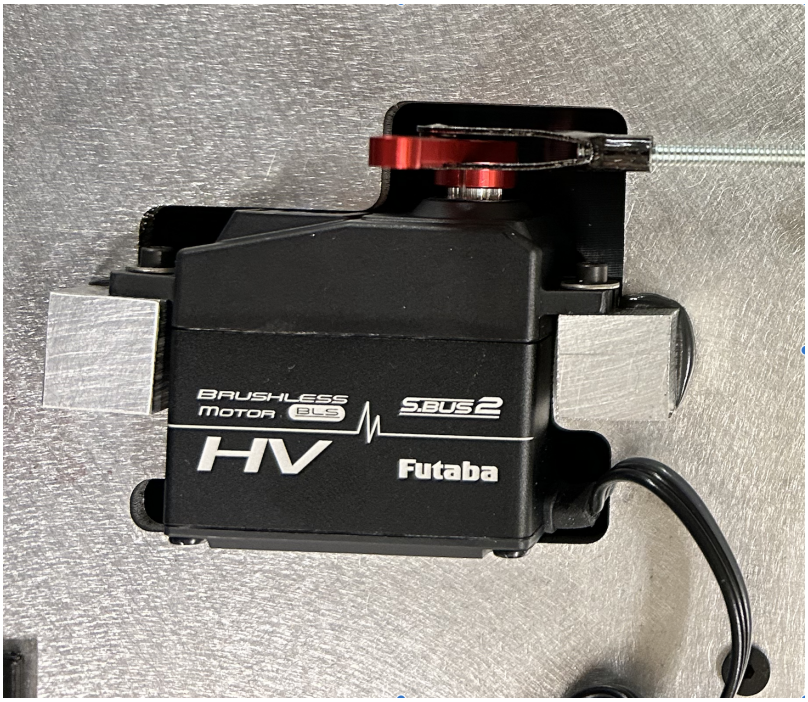



Figure 2.13: Installed servo motor

contribute to higher amplitude motion experienced by the model resulting in higher amplitude signals from the sensors. A wingtip accelerometer is pictured as installed in Figure 2.16.

## *2.4 Model Control and Data Acquisition*

### *2.4.1 Model Control*

The control surface actuators are commanded by Simulink Desktop Real-Time via a Pololu Servo Controller through the computer's Serial port (Figure 2.17). The Simulink model and project also command the gust-generation system which will not be discussed in detail as a new gust generation control system was still in development in the period of MARGE-II development described in this thesis. The servo motors share a power supply but are controlled via independent signals from the Pololu Mini Maestro controller.

Table 2.2: Sensor instrumentation and placement

| **Sensor** | **Qty** | **Location** |
|---|---|---|
| Hall Effect Sensor (Honeywell RTP060LVEAA) | 1 | U-channel above Pitch Axis |
| 3-Axis MEMS Accelerometer (ADXL356BZ) | 3 | Fwd and Aft Wing Tip, Fuselage |
| Strain Gauge | 5 | Wing (Root Spanwise, Root Chordwise, Mid) and Fuselage (Mid, Aft) |
| Potentiometer (ZX-PA-1.5-A) | 4 | Each Control Surface |
| Laser Vibrometer | 1 | External to Tunnel |

### *2.4.2 Data Acquisition*

All of the sensors on MARGE-II were selected to provide analog voltage output. The system is shown in Figure 2.18. The analog voltage output is used to create a voltage differential, comparing the "Out +" signal from the sensor against "Out -" directly from the power distribution board. This voltage differential is fed into a custom anti-aliasing circuit board which performs three functions: differentially remove sensor noise, provide a second order filter to serve as a form of anti-aliasing, and add gain to the signal, which is then sent to the DAQ. Each sensor has its own anti-aliasing circuit which provides a clean signal to the data acquisition system. Each sub-circuit can be individually tuned by means of a trim-potentiometer to remove voltage bias, which is extremely useful given the stacked resistance variation in the individual circuit

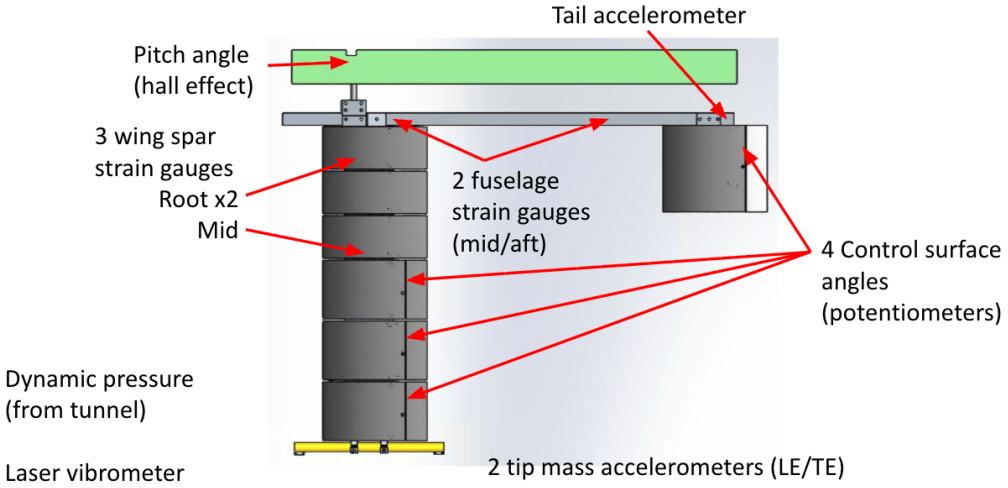



Figure 2.14: Sensor locations

components. This capability is particularly important for the strain gauge circuits which are also sensitive to external conditions such as ambient temperature.

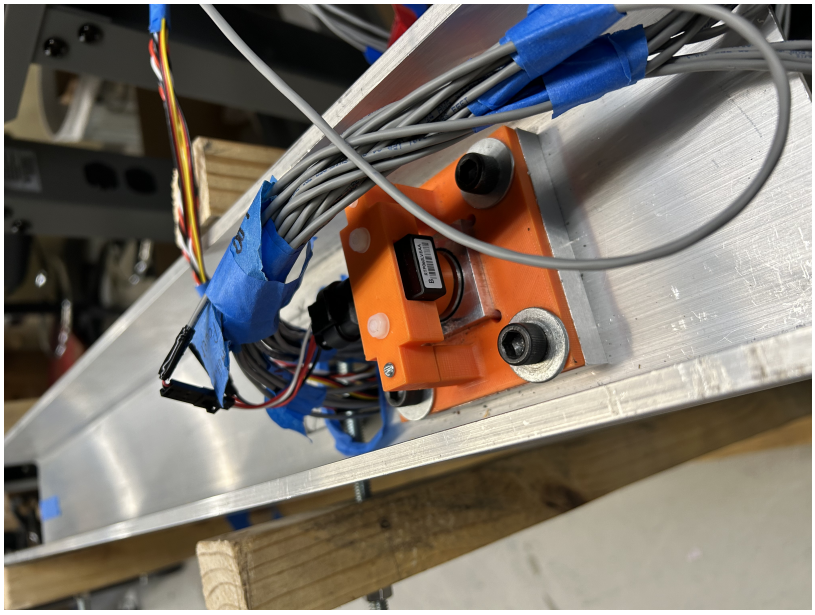


Figure 2.15: Hall effect sensor installed in mount

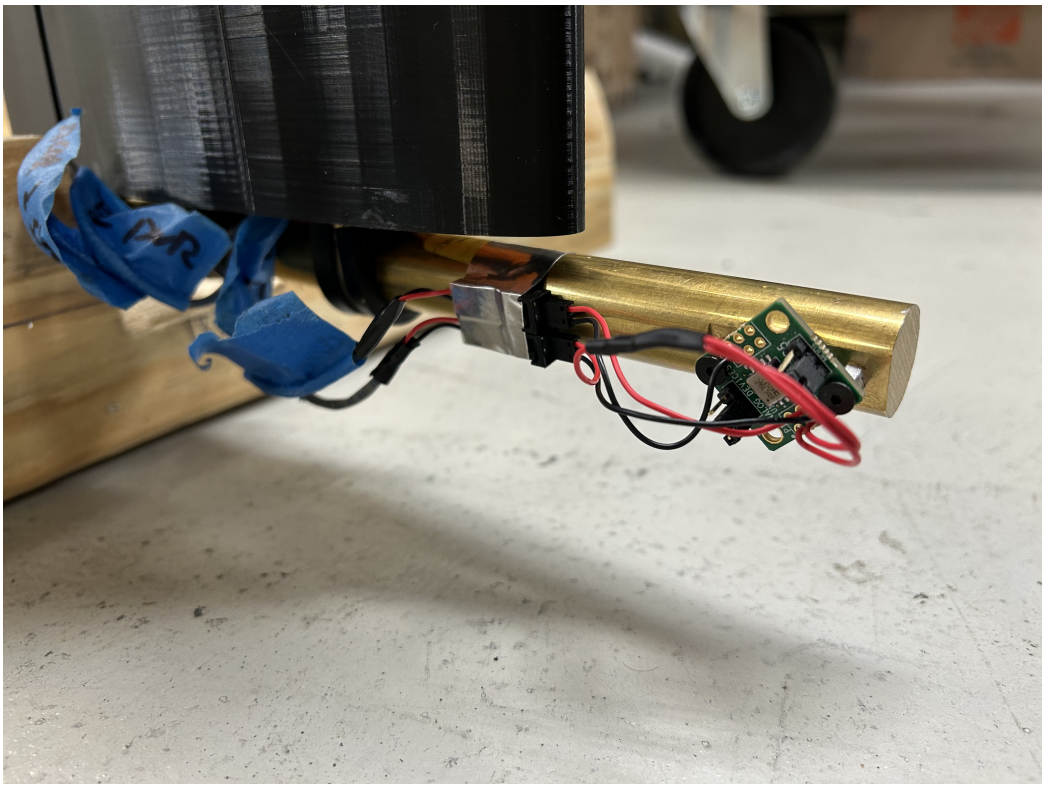


Figure 2.16: Installed wingtip accelerometer

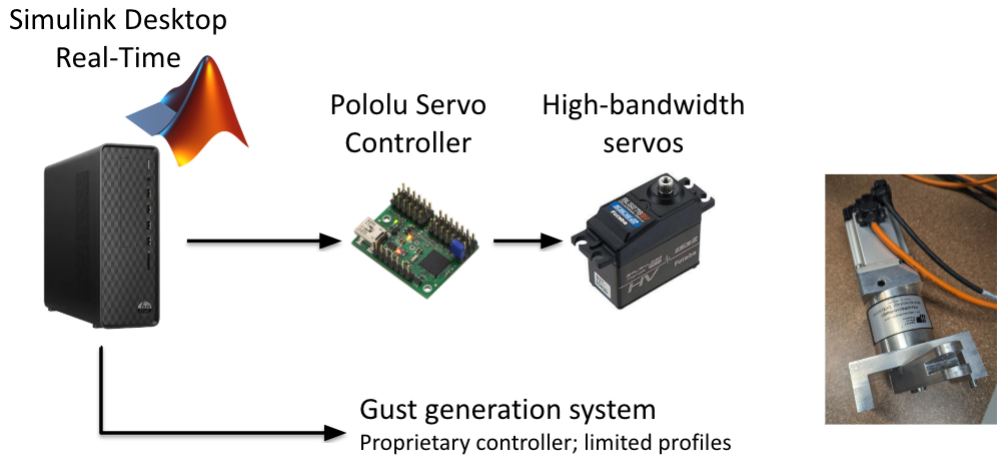



Figure 2.17: MARGE-II control system

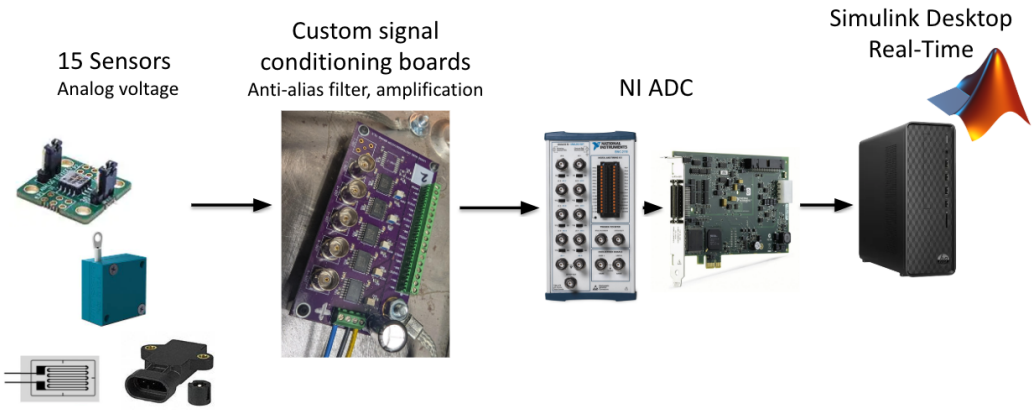



Figure 2.18: MARGE-II data acquisition system

# Chapter 3
# ANALYSIS AND INITIAL TEST RESULTS

This chapter details the early ground vibrational test performed on the underpinning structural elements of MARGE-II. The first week of the initial, exploratory wind tunnel test performed in Summer 2025 is also discussed, including explanation of the pitch instability discovered upon tunnel entry. Selected results from the two most instructive wind tunnel runs are then presented and analyzed, followed by discussion of key lessons learned from the tunnel entry, and required next steps.

## *3.1 Static Tests*

MARGE-II's internal structure was put through a vibrational test early in its development to confirm that the model's structural modal content was suitable. This test was performed by exciting the model, clamped in place at the wing root (see Figure 3.1), with a piezoelectric impact hammer and measuring the response with a laser vibrometer pointed at reflective tape on the tail and wing spar of the model. The signals from both the hammer and the vibrometer were fed into a Simulink model in real time to collect positional data that were synced with the impulse from the hammer.

A Fast Fourier Transform (FFT) was then performed in Matlab to extract the frequency content from the vibrational data. Results are shown in Figures 3.2 and 3.3. This data confirmed that the model's underlying structure had at least three modes under 20 Hz that would be within the bandwidth of the model's control surfaces. More extensive testing was not performed at this time because significant changes in mass and stiffness from the additions of the actuating system, sensors and wiring



Figure 3.1: Structural test setup

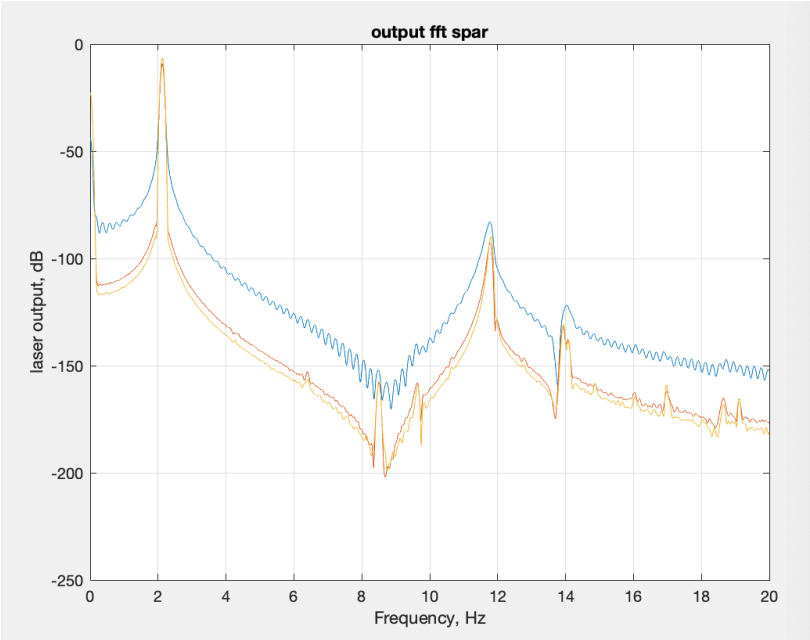



Figure 3.2: FFT from wing spar impulse response data

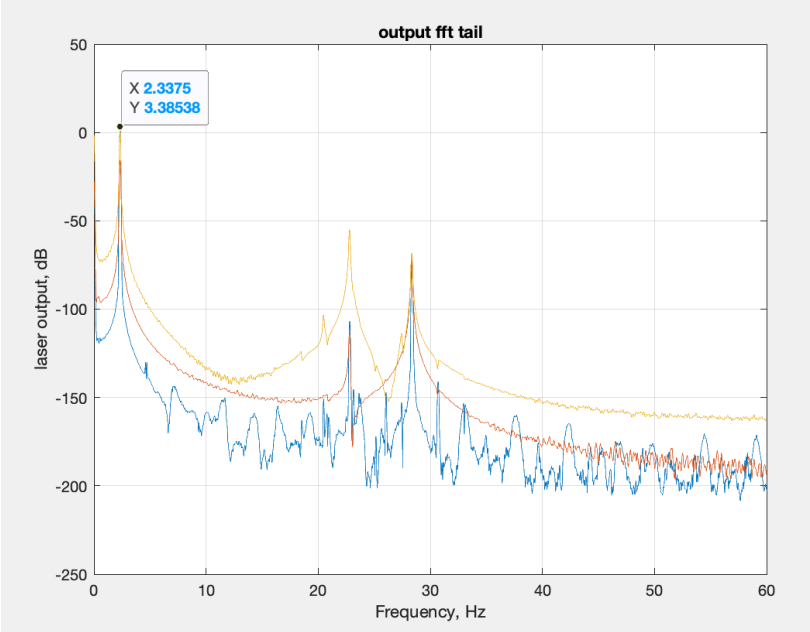



Figure 3.3: FFT from tail impulse response data

Table 3.1: Structural mode measured vs predicted frequencies

| Mode | Predicted Frequency | Measured Frequency |
|---|---|---|
| First Wing Bending | 2.3 Hz | 2.3 Hz |
| First Fuselage Bending | 6.4 Hz | 6.5 Hz |
| In-Plane Fuselage Bending | 11.7 Hz | 11.9 Hz |
| First Fuselage Torsion | 15.4 Hz | 14 Hz |
| Second Wing Bending | 17.3 Hz | not observed |

harnesses, and aero-shells were expected. The test successfully confirmed that the model's characteristics were reasonably within the desired final scope. Table 3.1 shows the estimated frequencies determined by examining the peaks found in the FFT plots in Figures 3.2 and 3.3. The NASTRAN modeling and analysis were performed chronologically after the structural vibrational test and are documented in Figures 2.1 and 2.8. Notably, the peak for first fuselage bending was not well observed in the FFT plots due to the positioning of the reflective tape on the tail surface of the model which was much more sensitive to fuselage torsion. The second wing bending mode was also not observed in the FFT data because the position of the reflective tape on the wing spar was on, or close to, a node for the second wing bending mode.

### *3.2 Wind Tunnel Entry 1*

In Summer 2025, MARGE-II entered the 3' x 3' wind tunnel at the University of Washington for the first in a series of exploratory model identification and shake-down tests. Week 1, beginning on 6/16/2025, included wind-on preparations, initial attempts at system identification, and general shakedown. Shakedown runs were performed with wind off to test the doublet and sweep functionality for each control surface and the gust vane system with the full data acquisition system engaged.

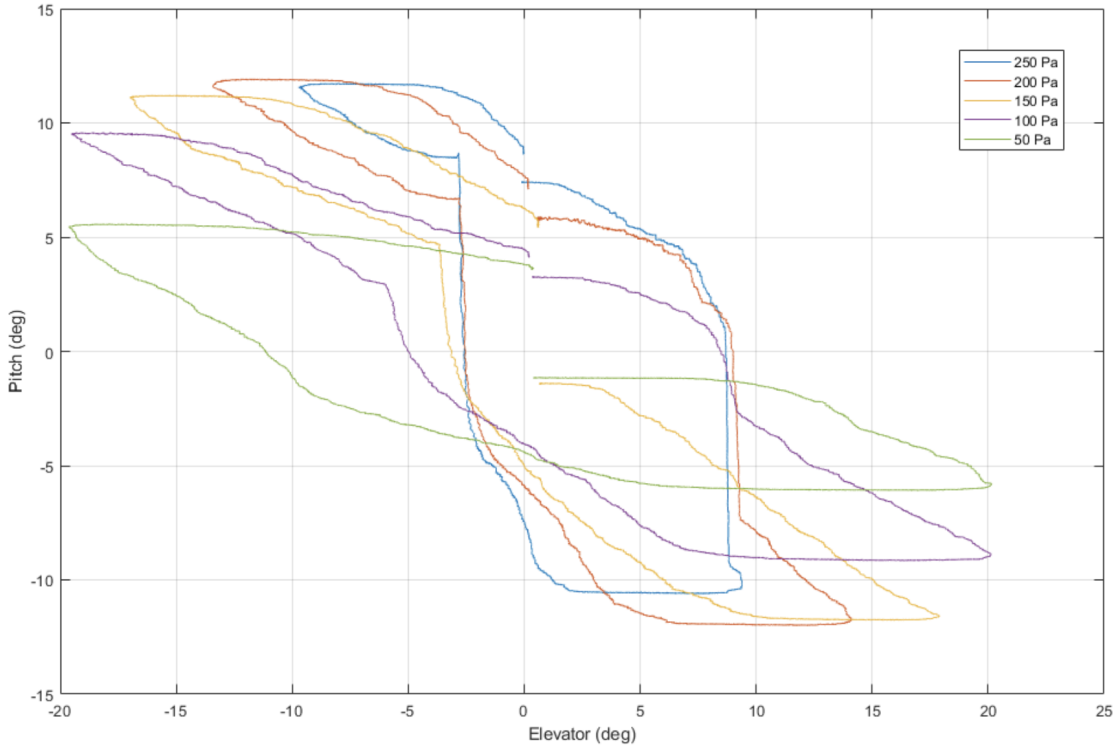



Figure 3.4: Pitch instability demonstrated

Wind-on runs were performed with no additional excitation, attempting to trim the model to 0 degrees angle of attack. The model proved difficult to trim consistently, pointing to pitch instability. Upon investigation, the pitch axis of the model was set at 44.5% of the chord due to a structure-centric design, which led to longitudinal instability. Figure 3.4 shows pitch angle for a slow elevator ramp input at different dynamic pressures from 50Pa - 250Pa with the near vertical lines pointing to small angle pitch instability.

### *3.2.1 Pitch Instability Discussion*

MARGE-II's design was built to emphasize ease of construction which resulted in missing the static margin analysis that would have shown the pitch instability dis-

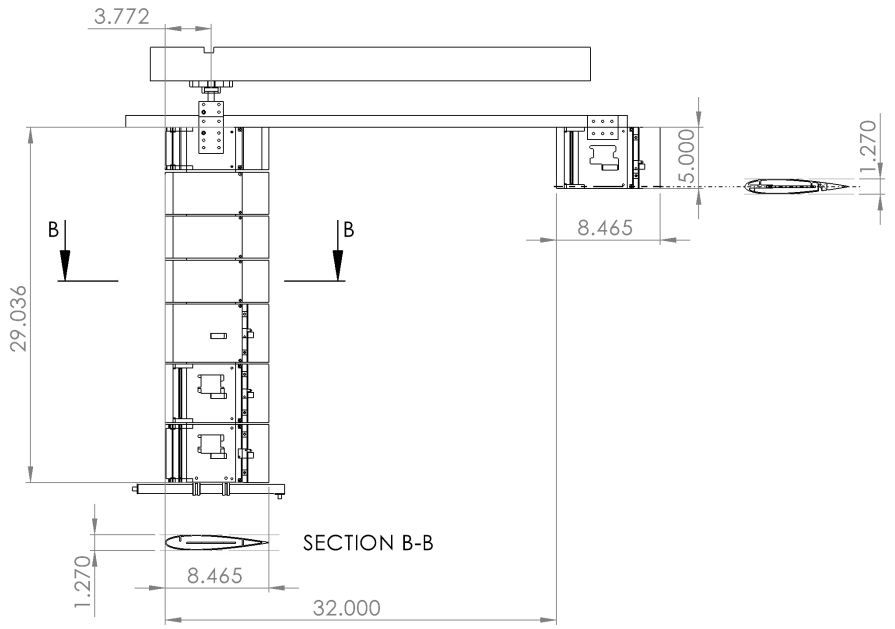



Figure 3.5: MARGE-II Assembly Aerodynamic Dimensions

covered upon tunnel entry. As initially configured for week 1 of the exploratory wind tunnel entry (see Figure 3.5), MARGE-II's static margin was approximated to be -10.00%.[1] As a negative static margin results in longitudinal instability, the model was adjusted in several ways during week 2 of the exploratory wind tunnel entry. First, the wing was moved forward by 1.25 inches, placing the pivot point, which is effectively the model's center of gravity, forward to 29% of the wing Mean Aerodynamic Chord (MAC). Moving the wing forward also increased the tail arm, which also improves static margin. Additionally, the tail aero shells were re-printed and extended from a 5-inch span to a 7-inch span. These changes increased the estimated static margin of MARGE-II to +7.40%, which was sufficient to stabilize the model. This work was performed by Barkin Sarigöl and Alex LaFranchi, and the wind tunnel

[1]Detailed calculations are shown in Appendix A, using approximations found in [19].

results obtained by their testing are out of the scope of this thesis. Their work can be found in [20, 21].

### *3.2.2 Wind Tunnel Entry 1 Results*

After low-speed wind on shakedown and trim runs, testing progressed in blocks: slowly increasing dynamic pressure, collecting data with the model unexcited, then with a doublet with each control surface, then with a discrete gust generated by the gust vanes, then sweeps with each control surface, and finally with a continuous gust generated by the gust vanes at frequencies targeting the model's structural modes. The amplitudes for the control surface and gust inputs were adjusted by starting at low amplitudes and increasing the amplitudes until an adequate response was observed from the model.

The pattern of dwells, doublets, sweeps, discrete and continuous gusts was repeated from 50-250 Pa of dynamic pressure in increments of 50 Pa. The recorded data was post-processed and used to generate Frequency Response Function (FRFs) estimates and Power Spectral Densities (PSD) for use in model identification work.

The following set of plots shows results from runs 118 and 119 which are elevator and outboard aileron sweeps performed at 250 Pa dynamic pressure with an expanded frequency sweep of 0 to 25 Hz, also at 5 degrees. These runs were selected as the demonstrations for this thesis because they were the highest dynamic pressure and highest amplitude runs performed in the initial shakedown testing block. This condition and sweep show the control surfaces operating at their most effective manner, resulting in the highest level of excitation in the model from this block of testing and the highest amplitude signals from all of the available sensors. Including both the outboard aileron and elevator sweep conditions was necessary to excite the model along the two principal axes of motion in the model - along the length of the fuselage and along the span of the wing.

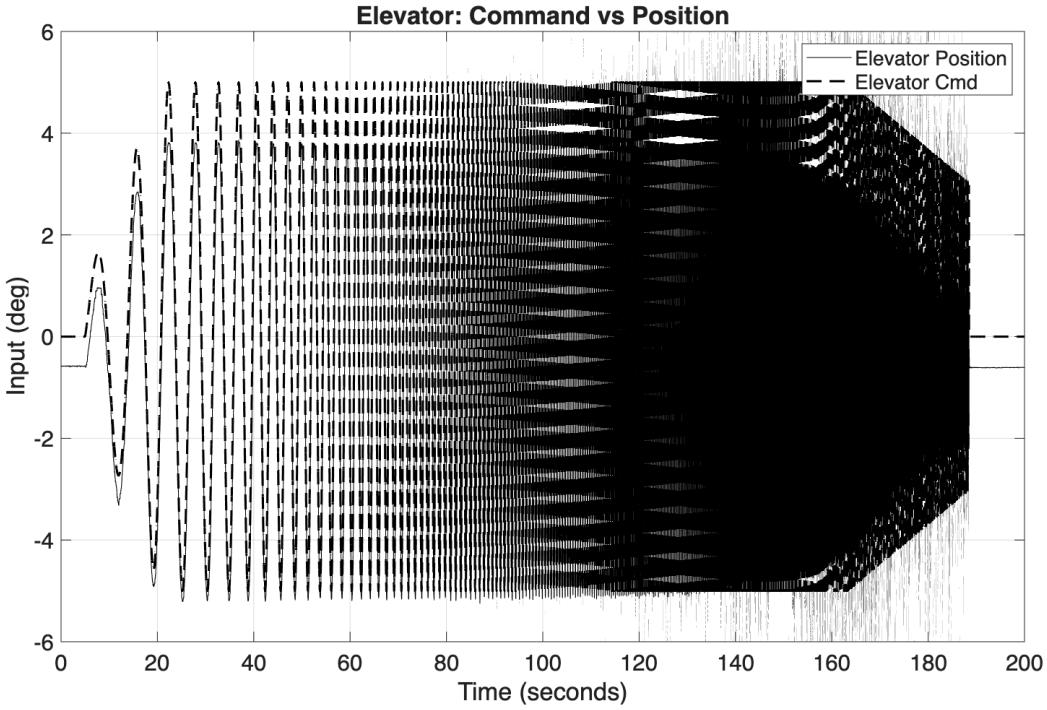



Figure 3.6: 250 Pa elevator sweep 0-25 Hz position vs command data

*Run 118 Time History Data*

Run 118 was an elevator frequency sweep from 0-25 Hz at 250 Pa of dynamic pressure. Figure 3.6 shows the commanded position for the elevator tracks very closely in phase with the commanded input but does not reach the plus 5 degree input. This amplitude deficiency was not noticed during the test and was not chased down as there were more pressing issues to address during the shakedown test, and because the goal of these initial runs was to characterize the aeroelastic modes of the model. These aeroelastic modes are still excited by this type of input, as the frequency matters more than amplitude of input here. There is expected roll off towards the higher end of the frequency range also demonstrated here. Differences between commanded and actual control surface position are also, of course, affected by imperfections inherent in actuator nonlinearities and by some freeplay between the actuator and control

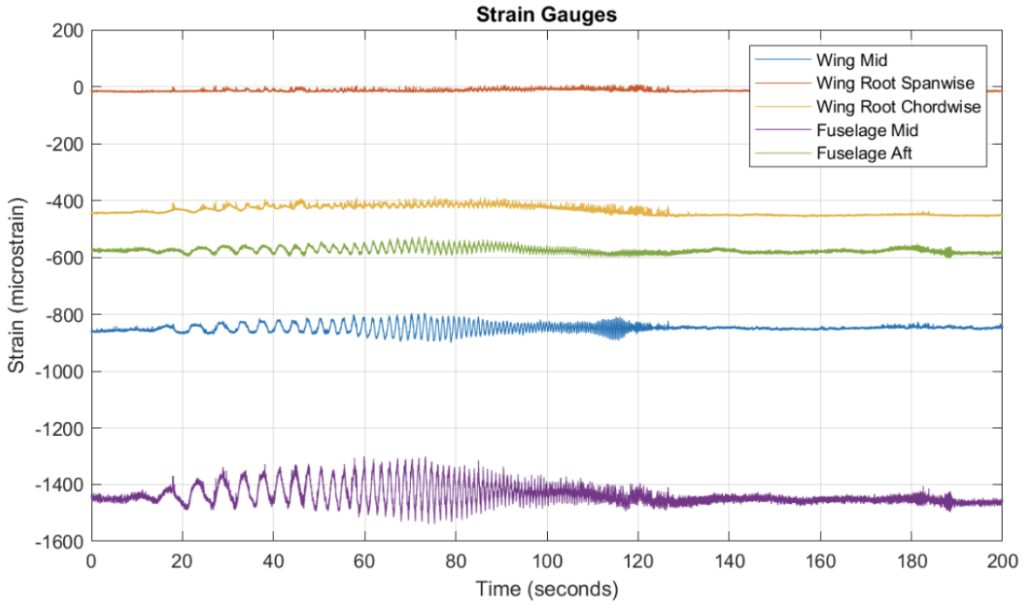



Figure 3.7: 250 Pa elevator sweep 0-25 Hz strain gauge data

surface.

*Run 118 Strain Gauge Time History Data*

The mid-fuselage strain gauge exhibited the highest amplitude excitation from the elevator frequency sweep in run 118 (Figure 3.7) followed by the mid-wing strain gauge and the aft fuselage strain gauge. This figure demonstrates problems with strain gauge distribution - the wing root strain gauges do not respond with enough amplitude to be useful to elevator excitation input.

*Run 118 Accelerometer Time History Data*

Here, the accelerometer data has been split into separate plots (Figures 3.8, 3.9, 3.10) for clarity. However, the data across all three accelerometers is uniformly noisy. Despite the noise, there are still clear peaks, indicating aeroelastic modes being excited at various frequencies during the sweep. The run 118 elevator frequency sweep

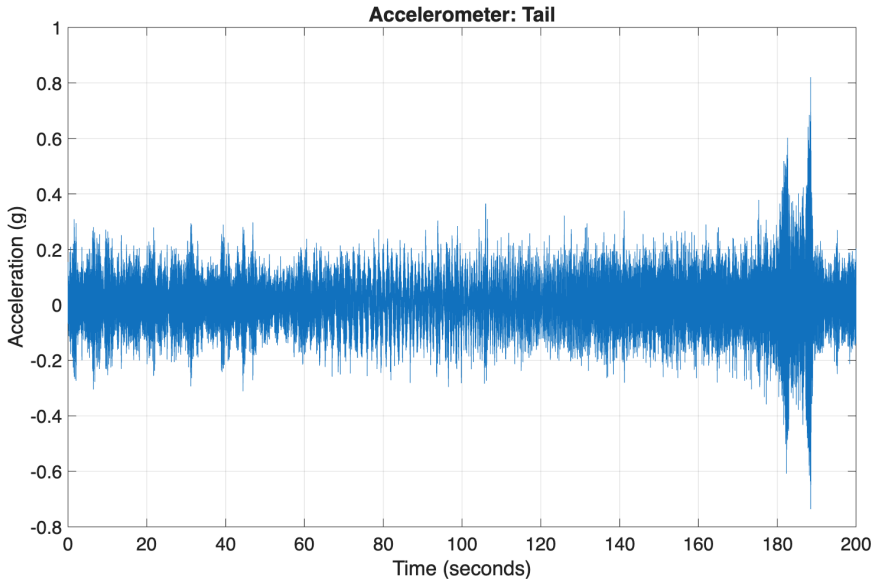



Figure 3.8: 250 Pa elevator sweep 0-25 Hz tail accelerometer data

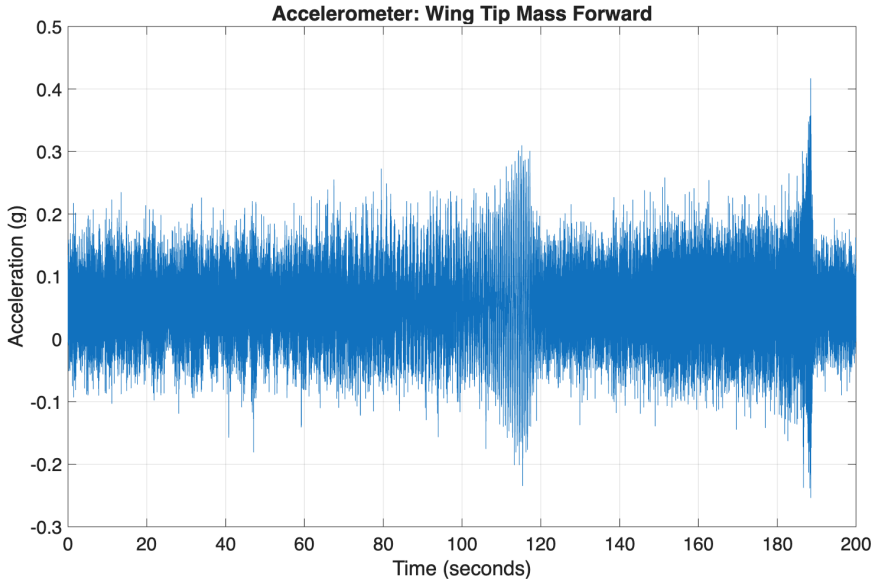



Figure 3.9: 250 Pa elevator sweep 0-25 Hz forward wingtip accelerometer data

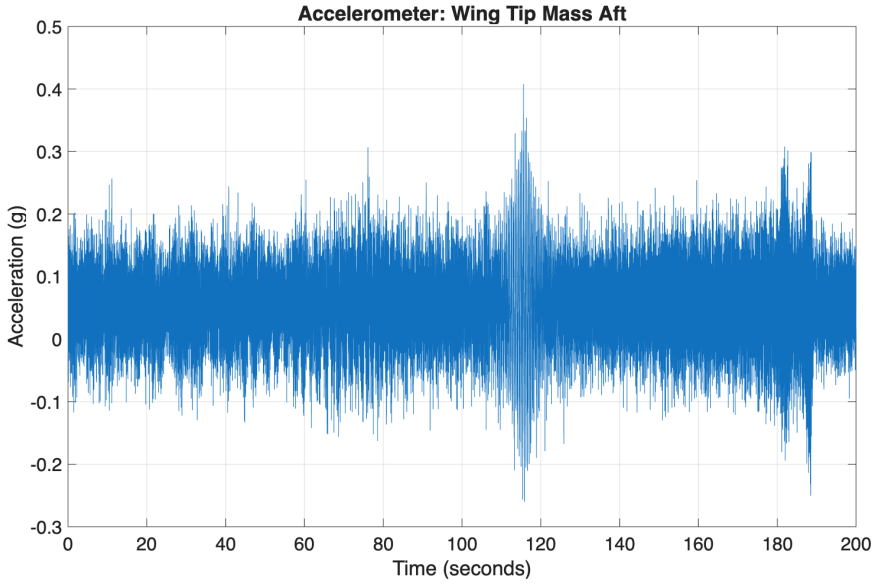



Figure 3.10: 250 Pa elevator sweep 0-25 Hz aft wingtip accelerometer data

generates clearer peaks in the wingtip accelerometers than in the tail accelerometer. Ideally, the wingtip accelerometers are spaced far enough apart to observe wing twist in structural modes.

*Run 118 Pitch Time History Data*

The Hall-Effect sensor pitch time history data in Figure 3.11 demonstrates a clear peak pitch excitation in the model with a sharp roll-off, as would be expected by actuating control surfaces faster than the whole model can respond at this relatively low dynamic pressure.

*Run 118 Post-Processed Data*

The time history data collected from the wind tunnel run via Simulink was post-processed in Matlab using a script, written by Alex LaFranchi, which calculates a weighted average composite Frequency Response Function (FRF) using the chirp z

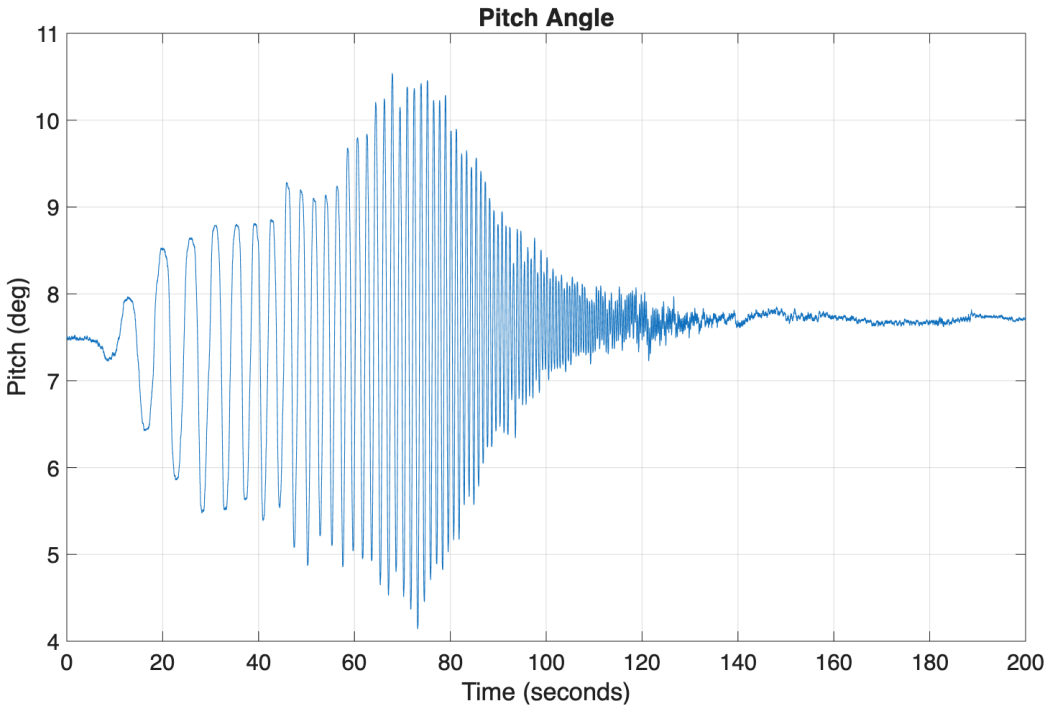



Figure 3.11: 250 Pa elevator sweep 0-25 Hz pitch data

transformation following calculations detailed in [22]. The script returns the coherence, gain, and phase for the FRF estimate, which can be plotted. The coherence plots show a measure of how much of the sensor output is caused by the control surface input on a scale of 0 to 1. The gain plots show the magnitude of the response with peaks indicating the frequencies where the structure resonates with the input. The phase plots show time delay measured in degrees from -180 to 180, with 0 degrees meaning the sensor response happens at the same time as the input, and 180 degrees meaning the response is in the exact opposite direction of the input. When resonance peaks are passed, the phase shifts by 180 degrees.

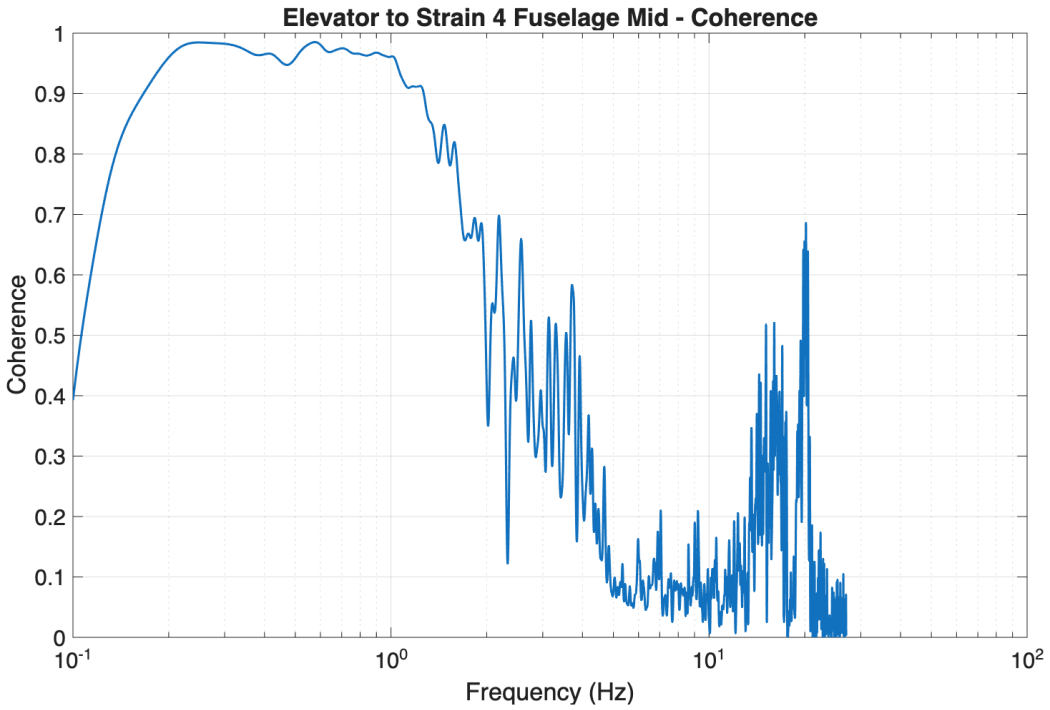



Figure 3.12: 250 Pa elevator sweep 0-25 Hz mid-fuselage strain gauge coherence FRF estimate

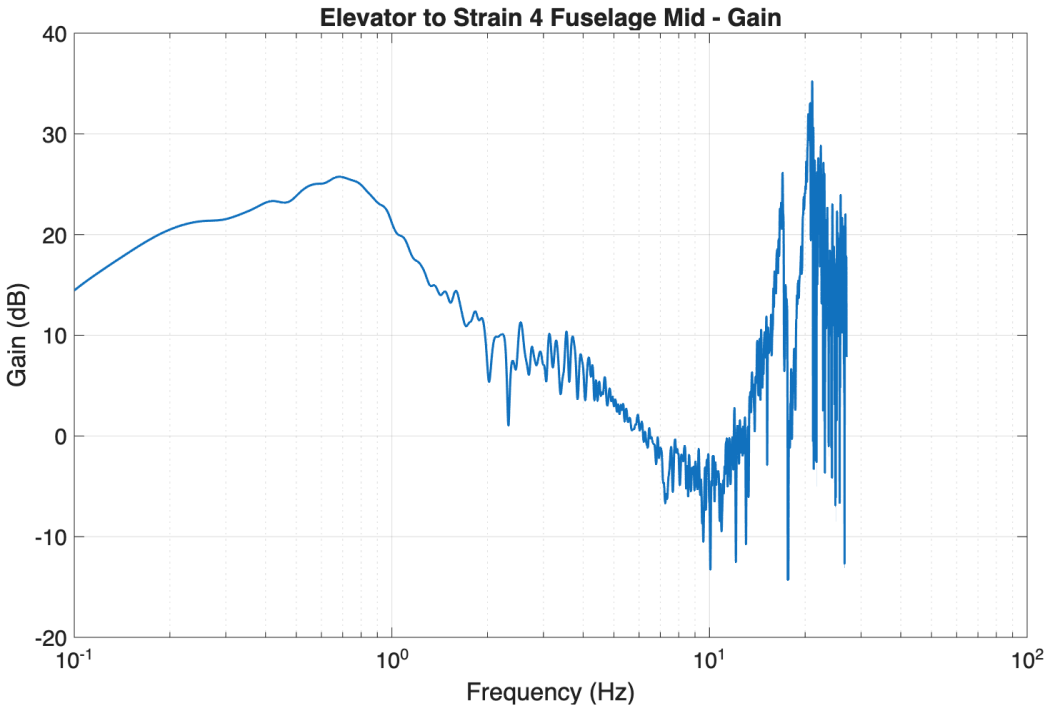



Figure 3.13: 250 Pa elevator sweep 0-25 Hz mid-fuselage strain gauge gain FRF estimate

*Mid-Fuselage Strain Gauge FRF Estimates*

Beginning with the coherence plots will inform where the following gain and phase plots are reliable. This mid fuselage strain gauge coherence plot (Figure 3.12) illustrates that the strain gauge response is not coherent much past 1 Hz, making the data unreliable.

The FRF in Figure 3.13 shows gain response for the mid fuselage strain gauge, where we are looking for gain peaks at aeroelastic modes as shown in Table 3.1. While there is some increasing response until 0.7 Hz, there are not significant peaks in the gain response, and anything below 2.3 Hz does not correspond directly to structural modes. The hump in this gain plot probably corresponds to rigid body pitch.

The phase response (Figure 3.14) for the mid fuselage strain gauge shows a peak at 2.3 Hz, where the phase hits -180 degrees, which corresponds to the first wing

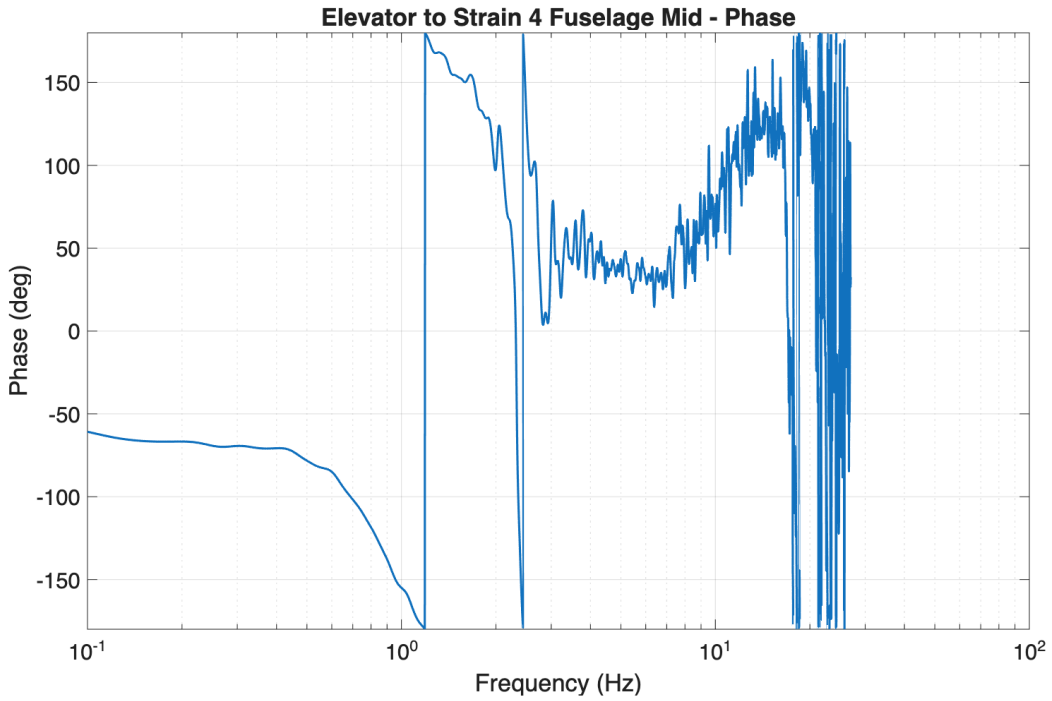



Figure 3.14: 250 Pa elevator sweep 0-25 Hz mid-fuselage strain gauge phase FRF estimate

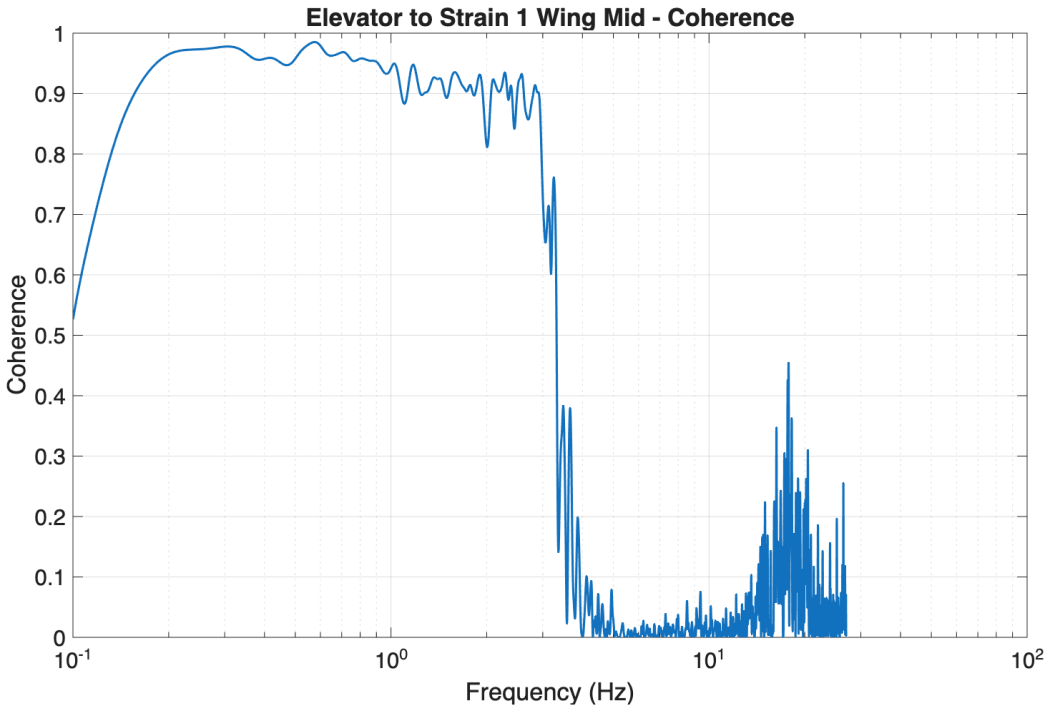



Figure 3.15: 250 Pa elevator sweep 0-25 Hz mid-wing strain gauge coherence FRF estimate

bending mode, despite no peak showing in the gain plot (Fig. 3.13). However, the strain gauge responses overall are of small enough amplitude, and are noisy enough that there are not a lot of lessons learned after about 3 Hz.

*Mid Wing Strain Gauge FRF Estimates*

The mid-wing strain gauge exhibits reasonable coherence up to 3 Hz in Figure 3.15, making it more useful than the fuselage strain gauge (Figure 3.12) despite the lower amplitude of overall response.

The gain FRF estimate (Figure 3.16) shows a peak around 2.3 Hz, corresponding to where we would expect to see the first wing bending which is the structural mode this sensor is expected to pick up. There are no other peaks in the plot that correspond to structural modes. The hump at around 0.6 Hz is related to rigid body "short period"

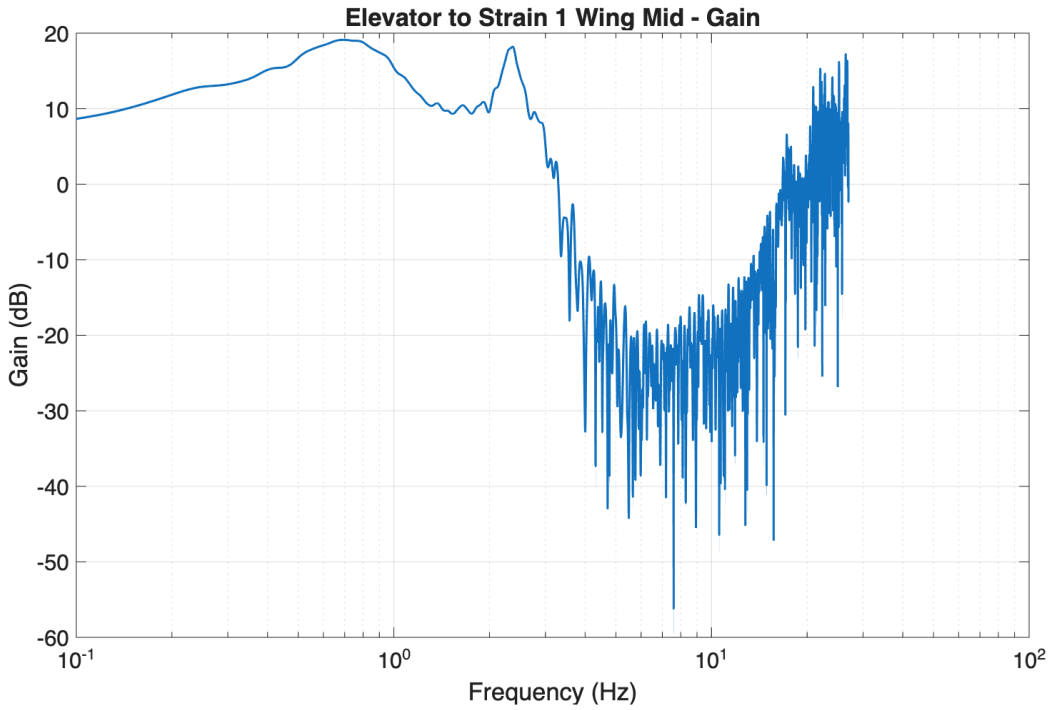



Figure 3.16: 250 Pa elevator sweep 0-25 Hz mid-wing strain gauge gain FRF estimate

pitching motion.

Again, this run demonstrated a phase lag that increases with frequency until the sensor's coherence drops and the noise makes any output unusable (Figure 3.17). We do, however, see the 180 degree phase shift that occurs after passing a natural resonance peak near 2 Hz for first wing bending.

*Wing Tip Mass Forward Accelerometer FRF Estimates*

Overall, we expect to see clearer responses from the model's accelerometers as they are less sensitive to noise than the strain gauges due in large part to the higher amplitude of signal they return. The wing tip forward accelerometer shows good coherence again, in Figure 3.18 up to 2 Hz, with a noticeable notch around 0.6 Hz which is attributable to the model's inherent pitch instability at the time of testing. At low

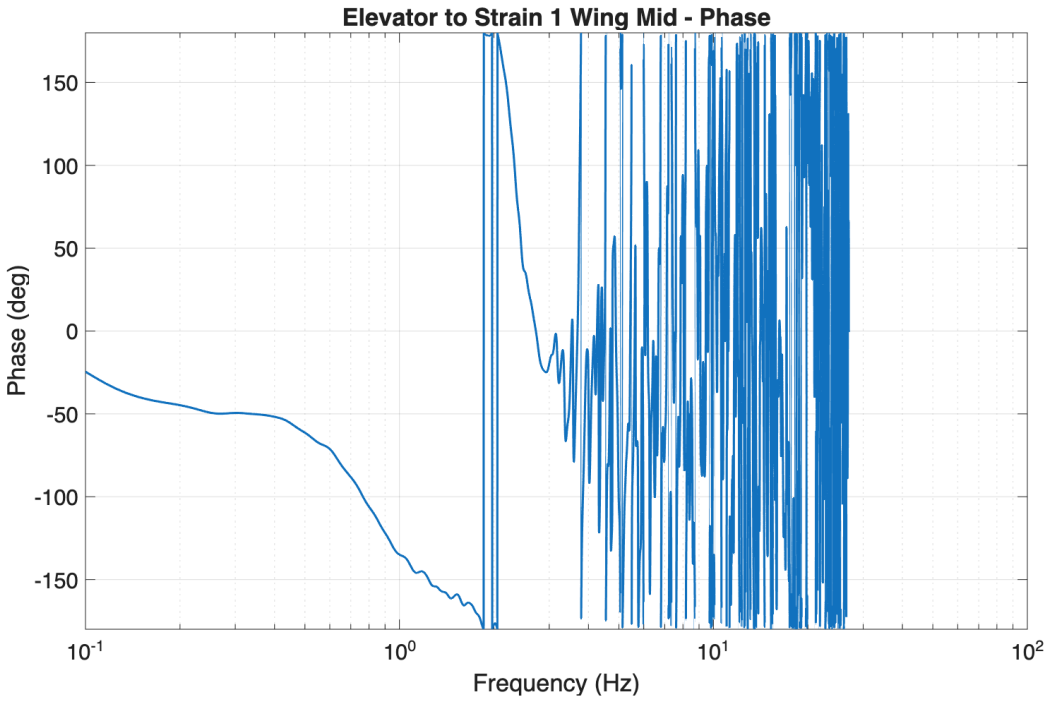



Figure 3.17: 250 Pa elevator sweep 0-25 Hz mid-wing strain gauge phase FRF estimate

frequencies, the instability results in pitching motion that is partially uncoupled from the elevator input as demonstrated by the slow ramps from 3.4. The coherence drops off after first wing bending.

The forward wing tip accelerometer gain response (Figure 3.19) shows a peak at 2.3 Hz and a notch at about 0.66 Hz following what we see in the coherence plot with the notch possibly representing the model's longitudinal stability in the rigid body frequency space and the peak occurring at the first wing bending mode.

Figure 3.20 again shows the 180 degree phase shift at the model natural resonance peak around 2 Hz. Additionally, the first fuselage bending mode introduces a large phase lag with respect to elevator inputs which follows from the mode shape - the structure is effectively "fighting" the elevator control input at the fuselage bending frequency between the elevator and the wingtip sensors, so the wingtip accelerometers would not be able to capture the input generated by the elevator.

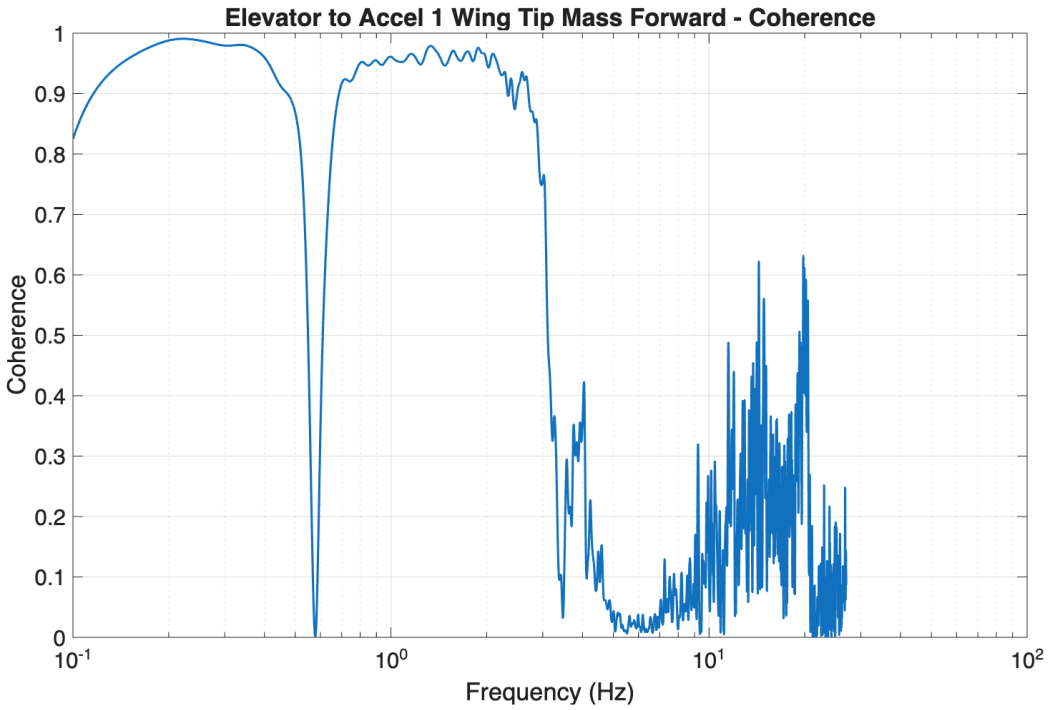



Figure 3.18: 250 Pa elevator sweep 0-25 Hz forward wing tip accelerometer coherence FRF estimate

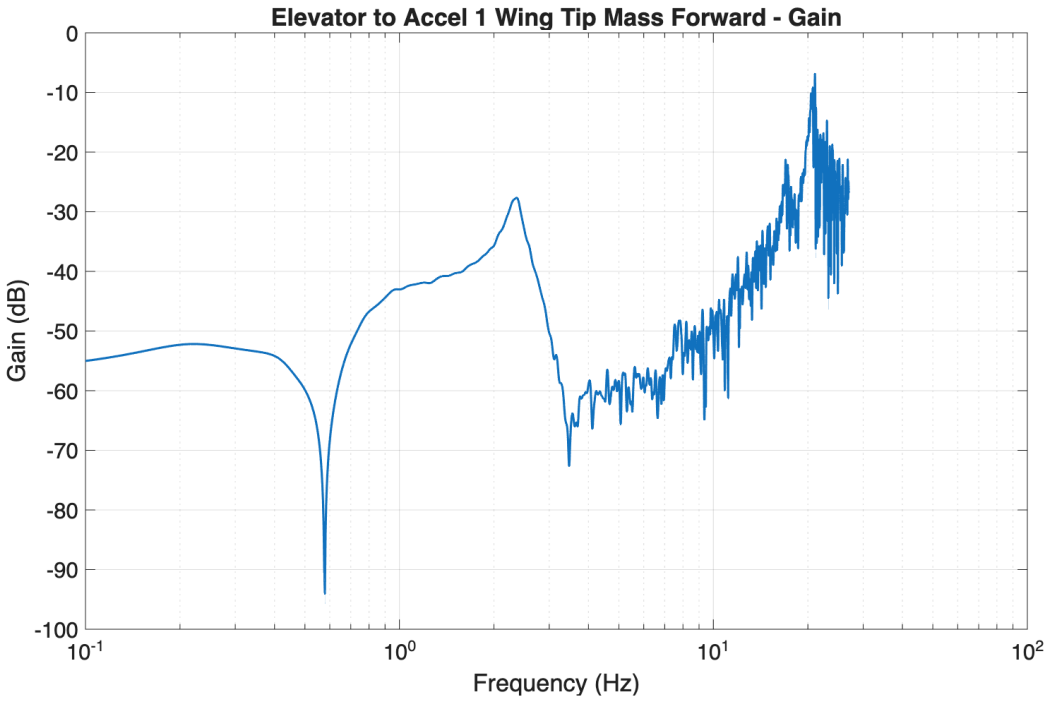



Figure 3.19: 250 Pa elevator sweep 0-25 Hz forward wing tip accelerometer gain FRF estimate

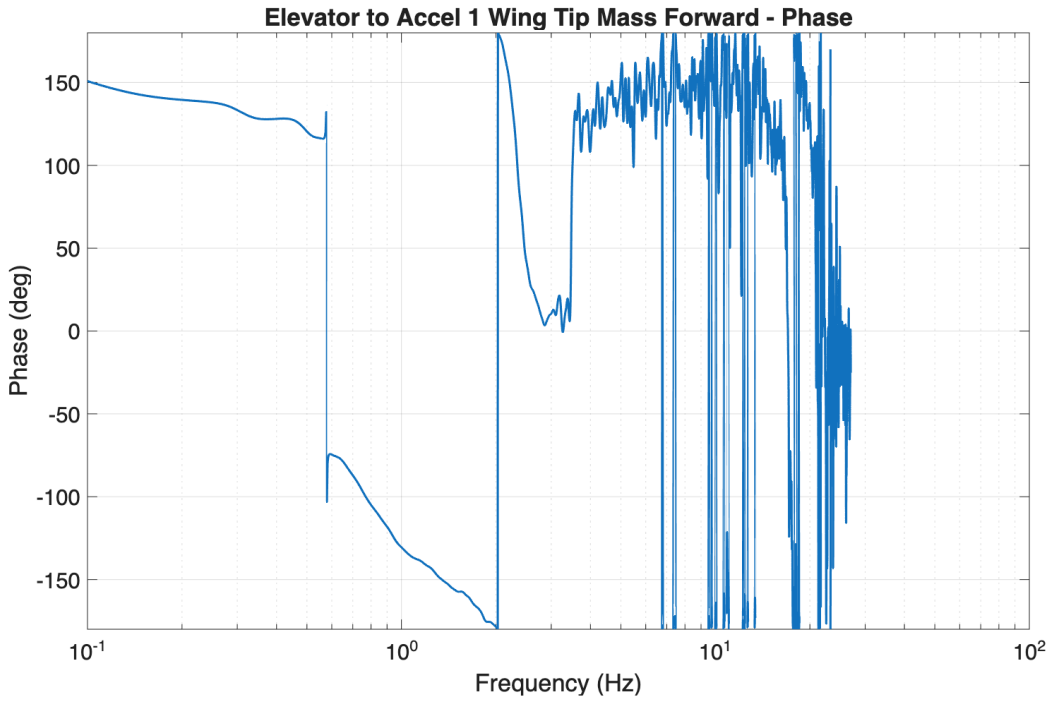



Figure 3.20: 250 Pa elevator sweep 0-25 Hz forward wing tip accelerometer phase FRF estimate

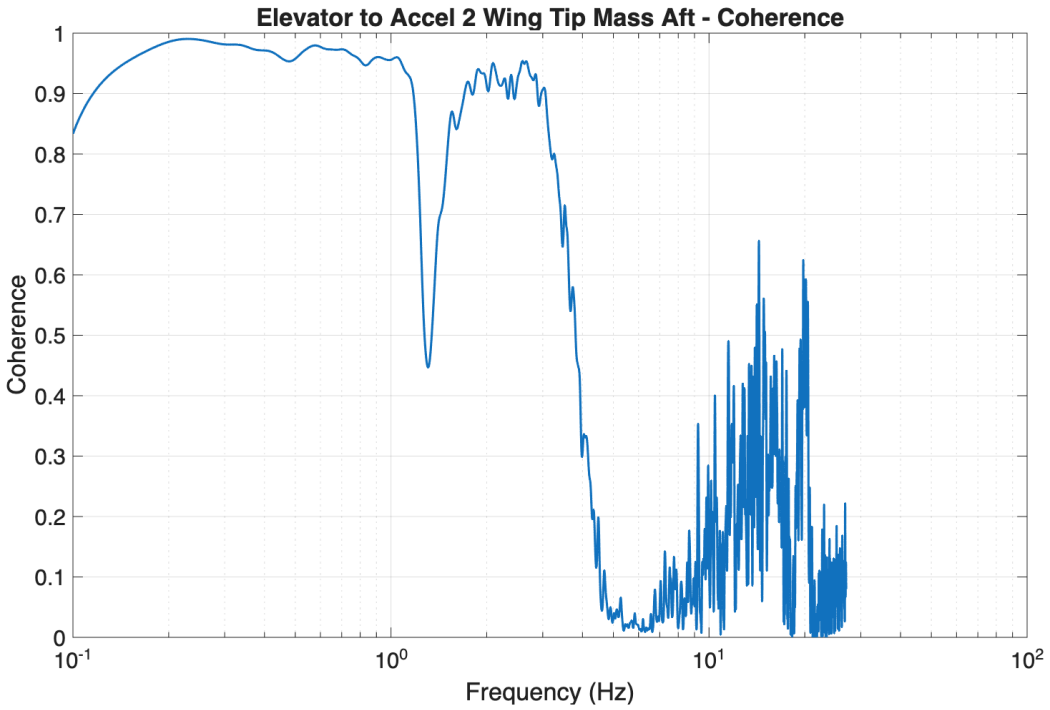



Figure 3.21: 250 Pa elevator sweep 0-25 Hz aft wing tip accelerometer coherence FRF estimate

*Wing Tip Mass Aft Accelerometer FRF Estimates*

The aft wingtip accelerometers tell a similar story to the forward accelerometer (Figure 3.21) except that the notch where the coherence drops out around 1 Hz. Again, this occurs more in the rigid body region of the model's response.

The aft wingtip accelerometer gain FRF estimate in Figure 3.22 shows us a similar story to the one shown in the coherence plot - the only poles that are clearly identifiable are the short period around 0.7 Hz and the first wing bending mode around 2 Hz.

The phase plot (Fig. 3.23) shows again the expected result of a 180 degree phase shift at the natural frequency around 2 Hz.

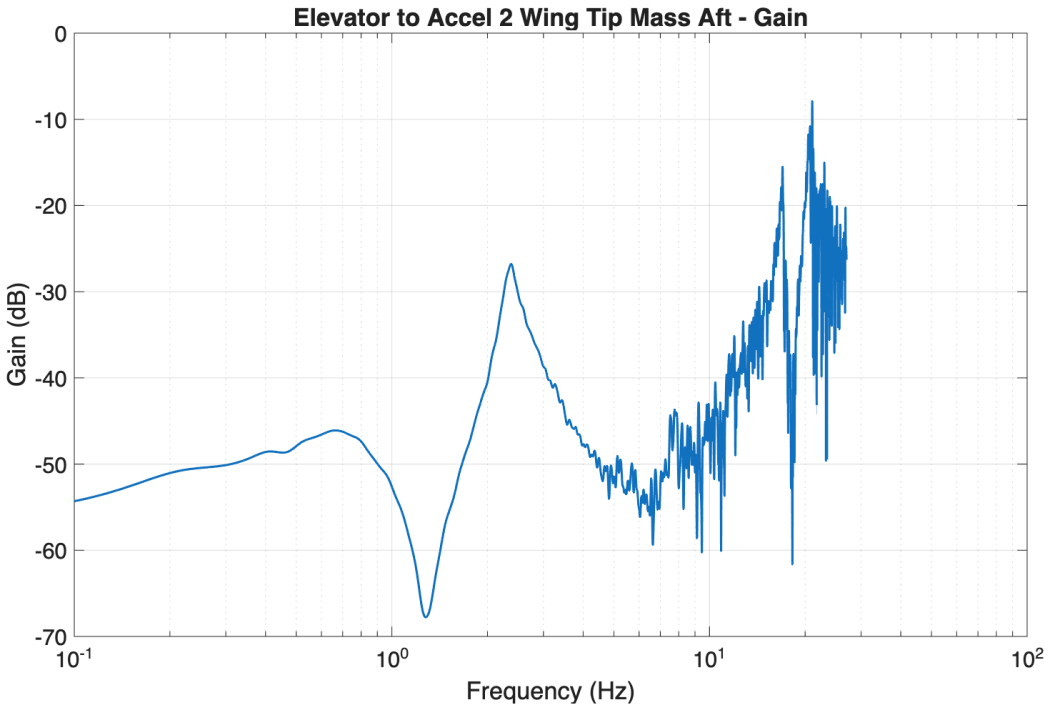



Figure 3.22: 250 Pa elevator sweep 0-25 Hz aft wing tip accelerometer gain FRF estimate

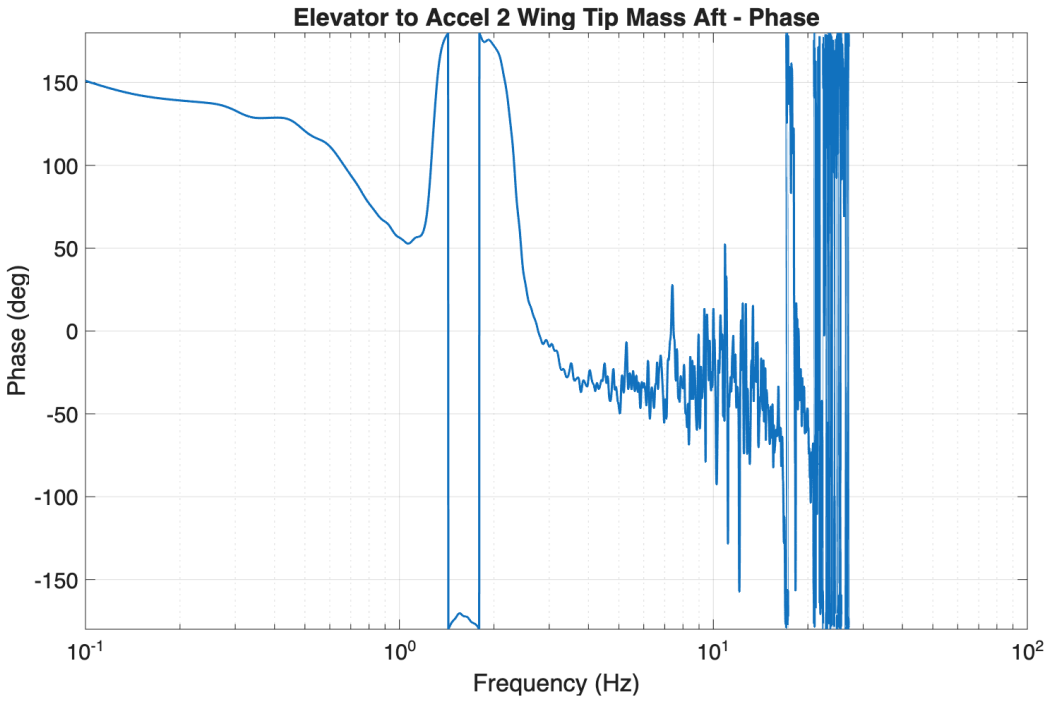



Figure 3.23: 250 Pa elevator sweep 0-25 Hz aft wing tip accelerometer phase FRF estimate

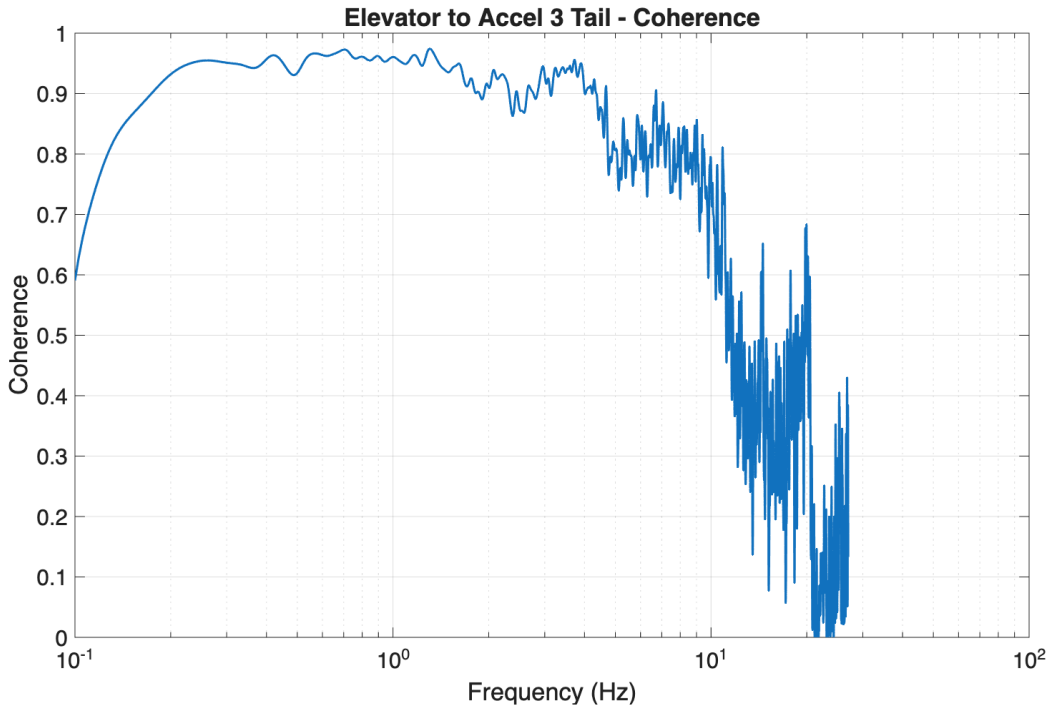



Figure 3.24: 250 Pa elevator sweep 0-25 Hz tail accelerometer coherence FRF estimate

*Tail Accelerometer FRF Estimates*

The tail accelerometer displays the best coherence of the sensor set examined thus far as shown in Figure 3.24, demonstrating reasonable coherence up to around 4 Hz before beginning to fall off.

The gain FRF in Figure 3.25 is somewhat disappointing for the tail accelerometer, failing to display any notable peaks within the reasonable coherence range for the sensor. This failure could be attributed to the placement of the sensor. Placing the sensor so close to the elevator, which is driving the aeroelastic excitation, prevents it from showing the structural excitation separate from the excitation that would occur if the structure were completely rigid. This lack of sensor response was an indicator for the research team that the tail accelerometer needed to be moved to adequately capture structural modes, and following week 1, this accelerometer was moved to a

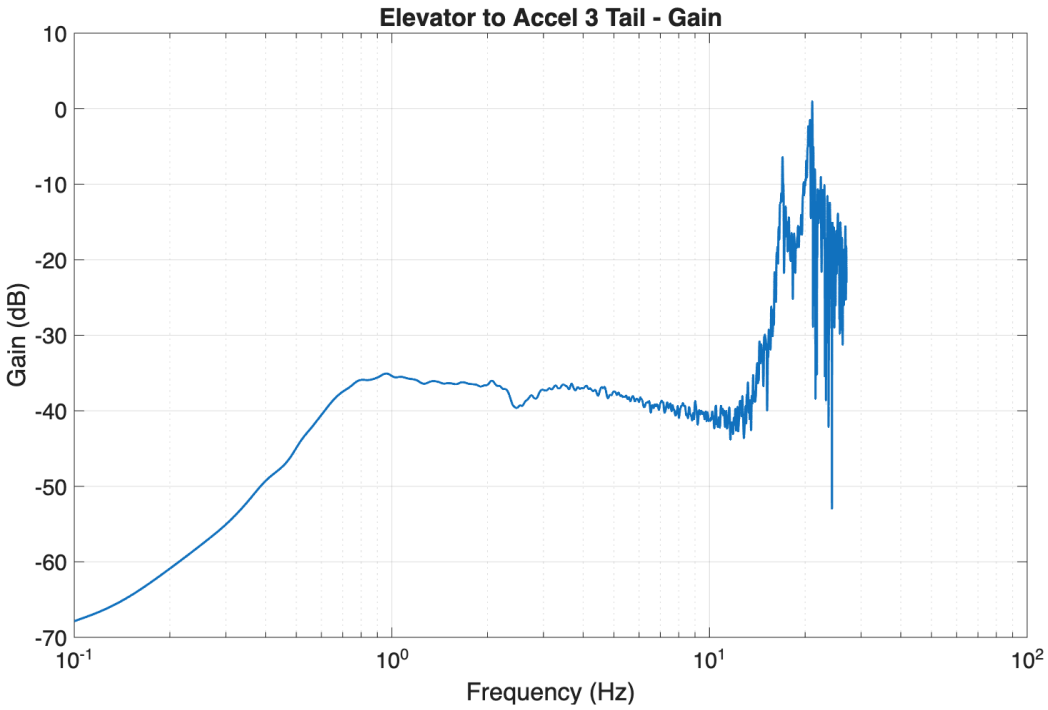



Figure 3.25: 250 Pa elevator sweep 0-25 Hz tail accelerometer gain FRF estimate

location around the midpoint of the model's fuselage which will allow better capture of the first fuselage bending mode shape being excited primarily by the elevator. The lack of gain response is reflected in the coherence plot - the input from the elevator is not actually driving gain response at the frequencies relevant to this model.

The phase FRF estimate (Figure 3.26) also fails to show much useful information, following the trends described in the gain plot FRF estimate discussion.

*Hall-Effect (pitch) FRF Estimates*

The Hall Effect sensor displays reasonable coherence up to around 3 Hz as shown in Figure 3.27, similar to other sensors examined previously in this section.

The gain FRF estimate shown in Figure 3.28 does not indicate any notable peaks that would be of interest to us in examining the aeroelastic mode shapes of the model.

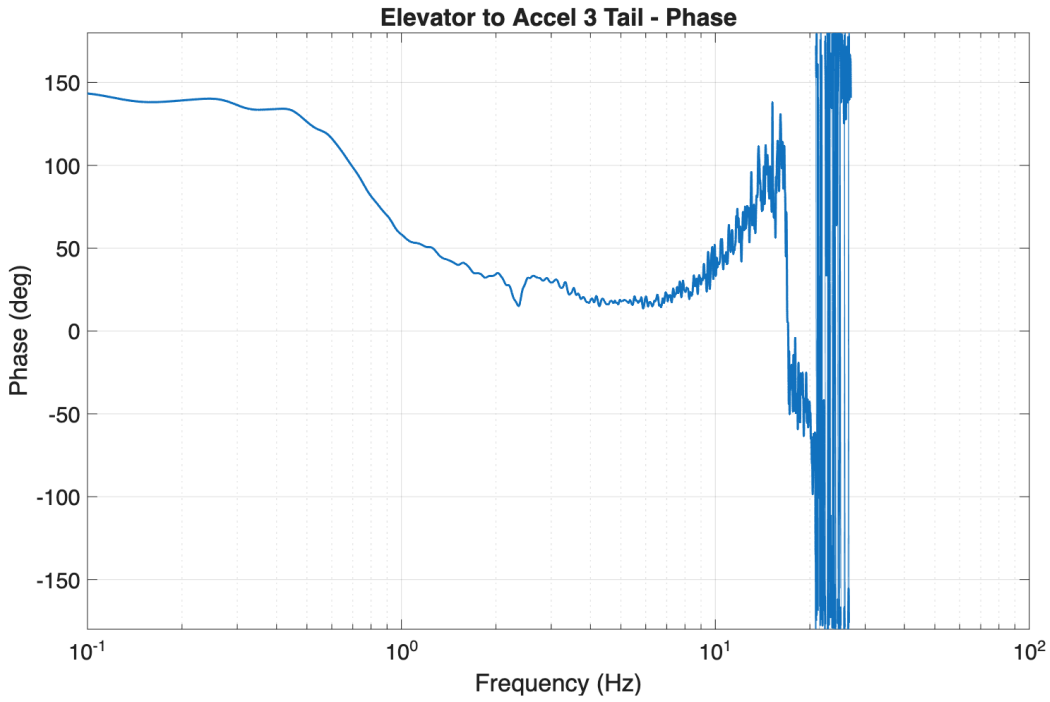



Figure 3.26: 250 Pa elevator sweep 0-25 Hz tail accelerometer phase FRF estimate

However, as this sensor is mostly tracking the rigid body "short-period" pitch of the model, we would not expect to see significant modal content captured by the Hall-Effect Sensor.

The phase FRF estimate plot (Figure 3.29) indicates a smooth roll off, representing increasing phase lag up until the coherence in the sensor measurement is lost, again not demonstrating capability to sense mode shapes in particular.

*Power Spectral Density (PSD) Analysis*

Power Spectral Density (PSD) analysis of test data was carried out using MATLAB's built in Welch's power spectral density estimate function. The data is divided into frequency windows with some overlap. A Discrete Fourier Transform was applied over each window. PSD is obtained in $V^2/Hz$ but for legibility the data is presented on a log scale as $dB/Hz$. Since the excitation is created to have a fixed amplitude,

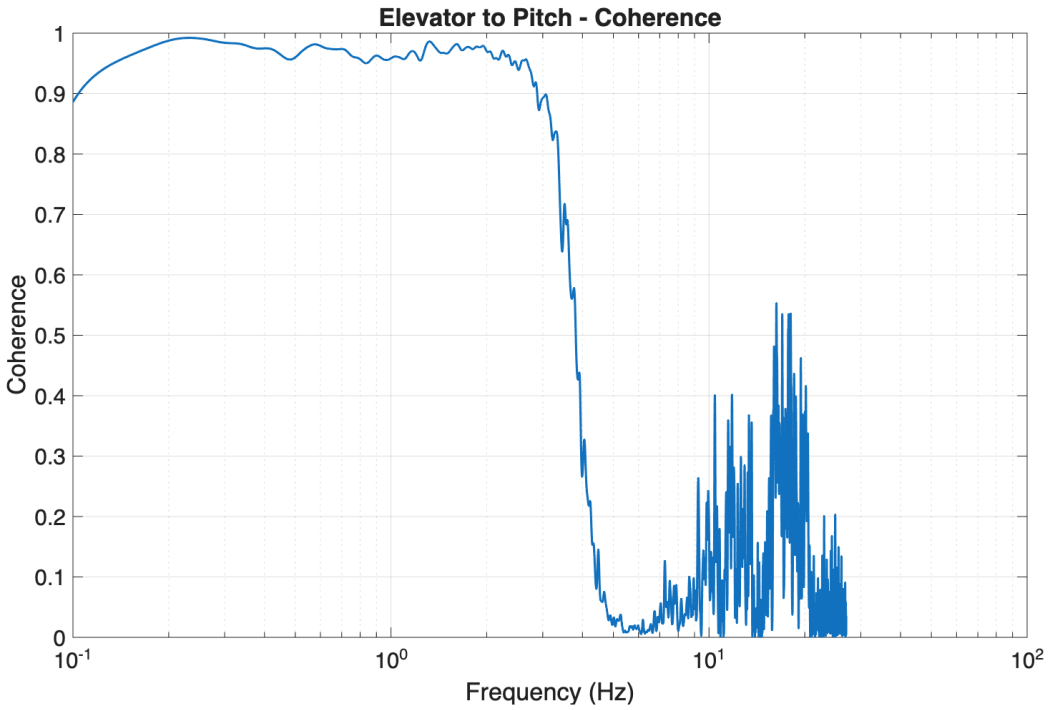



Figure 3.27: 250 Pa elevator sweep 0-25 Hz Hall-Effect (pitch) coherence FRF estimate

the peaks in the resulting PSD plots that are based on the sweep data correspond to the frequencies of aeroelastic poles that are being excited most and observed by each particular sensor.

In Figure 3.30, the aft fuselage strain gauge PSD shows a prominent peak around 17.3 Hz, where we would expect to see the second wing bending mode.

The mid wing strain gauge PSD shows a peak at 2.3 Hz in Figure 3.31 which is the first place so far that the first wing bending mode has been clearly captured. This plot shows the second wing bending mode around 17.3 Hz. It also shows the short-period peak at about 0.7 Hz.

In Figure 3.32, the forward wingtip accelerometer PSD plot shows a clear peak at the first wing bending mode around 2.3 Hz with another peak at the second wing bending mode around 17.3 Hz. These modes are the main modes the wingtip ac-

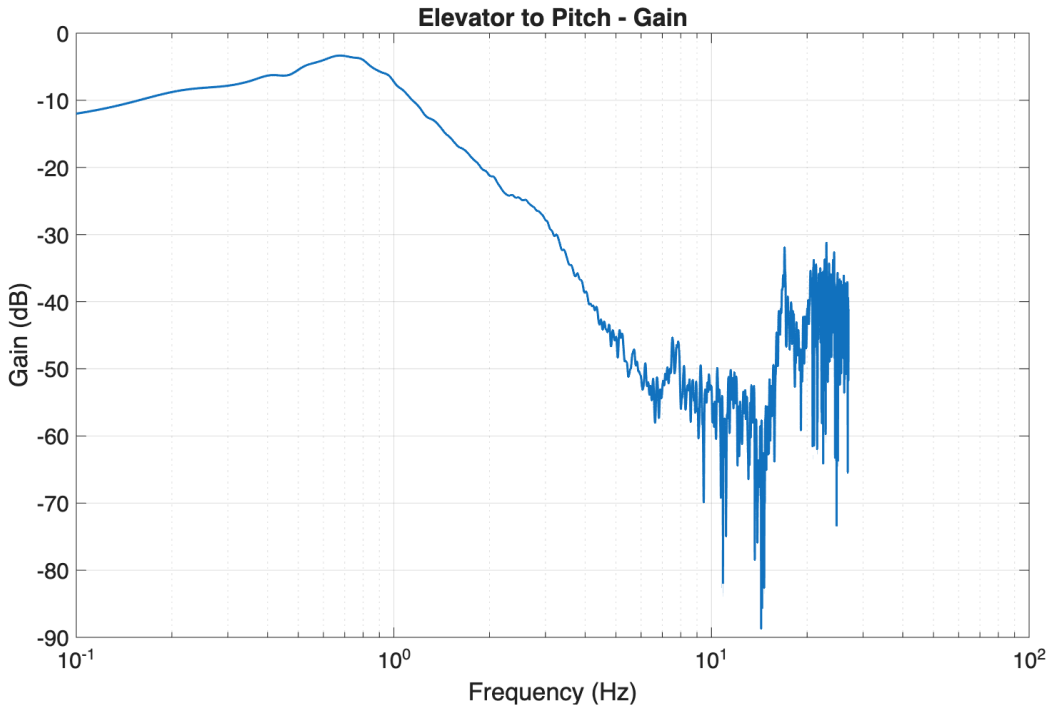



Figure 3.28: 250 Pa elevator sweep 0-25 Hz Hall-Effect (pitch) gain FRF estimate

celerometers should pick up on, as the wing torsion mode that would be captured by these sensors occurs at too high of a frequency to be useful while working with this model.

The aft wingtip accelerometer PSD plot (Figure 3.33) looks very similar to the forward wingtip accelerometer PSD plot in Figure 3.32, also capturing the two wing bending modes at 2.3 and 17.3 Hz.

The PSD of the tail accelerometer response in Figure 3.34 captures the short period and 17.3 Hz poles. The initial results from this sensor led to its subsequent relocation. In its initial location, the accelerometer was too close to the nodes of the fuselage modes that it was expected to observe.

The Hall-Effect sensor PSD plot in Figure 3.35 also shows the 17.3 Hz pole and the short period pole.

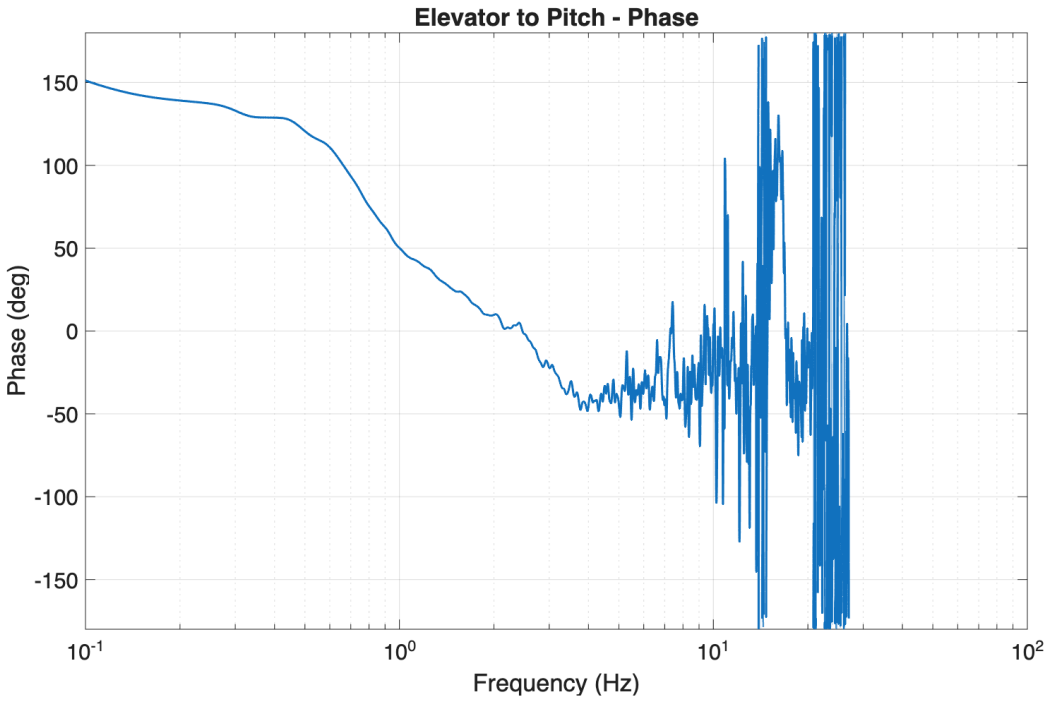



Figure 3.29: 250 Pa elevator sweep 0-25 Hz Hall-Effect (pitch) phase FRF estimate

It should be noted here that the FRF and PSD results presented so far are for wind-on conditions. The goal is to study the capability of the sensors to capture the low-frequency poles of the system. Naturally, aeroelastic wind-on pole frequencies are different from the wind-on "pure" structural dynamic frequencies and so some differences between the ground vibration (modal) test results and the wind-on results were expected.

*Run 119 Time History Data*

Run 119 was an outboard aileron frequency sweep from 0-25 Hz at 250 Pa of dynamic pressure. Figure 3.36 shows the aileron commanded position vs actual position during run 119. While difficult to see in the figure due to the length of the run, the traces closely match in both frequency and amplitude for most of the run, breaking down as expected towards the upper frequency limit.

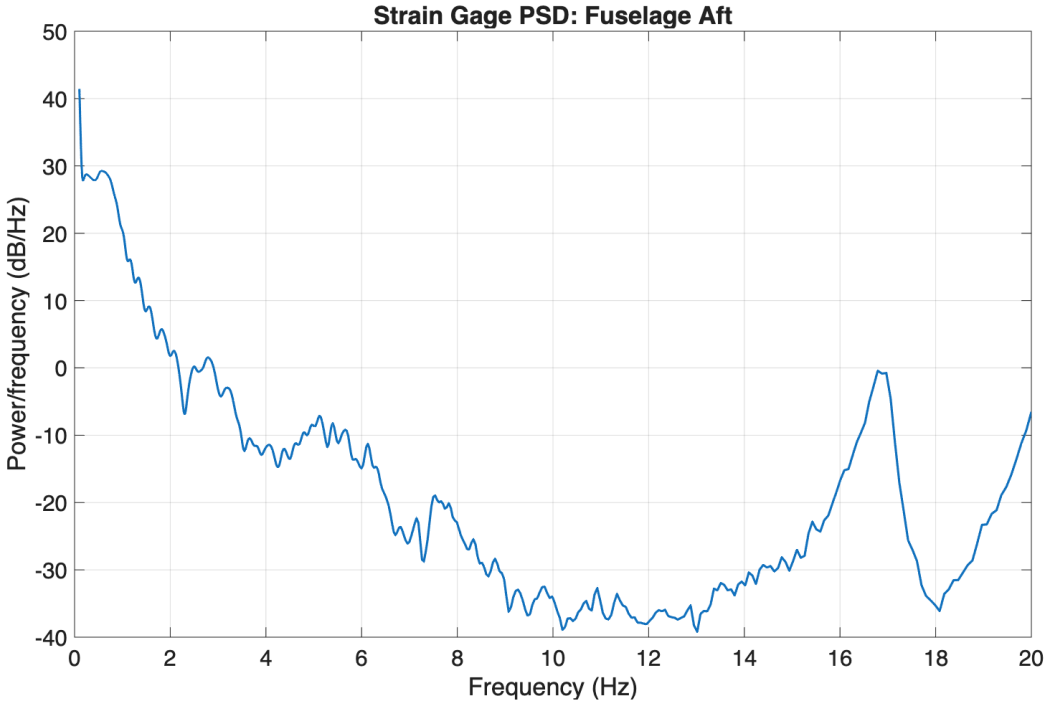



Figure 3.30: 250 Pa elevator sweep 0-25 Hz aft fuselage strain gauge power spectral density

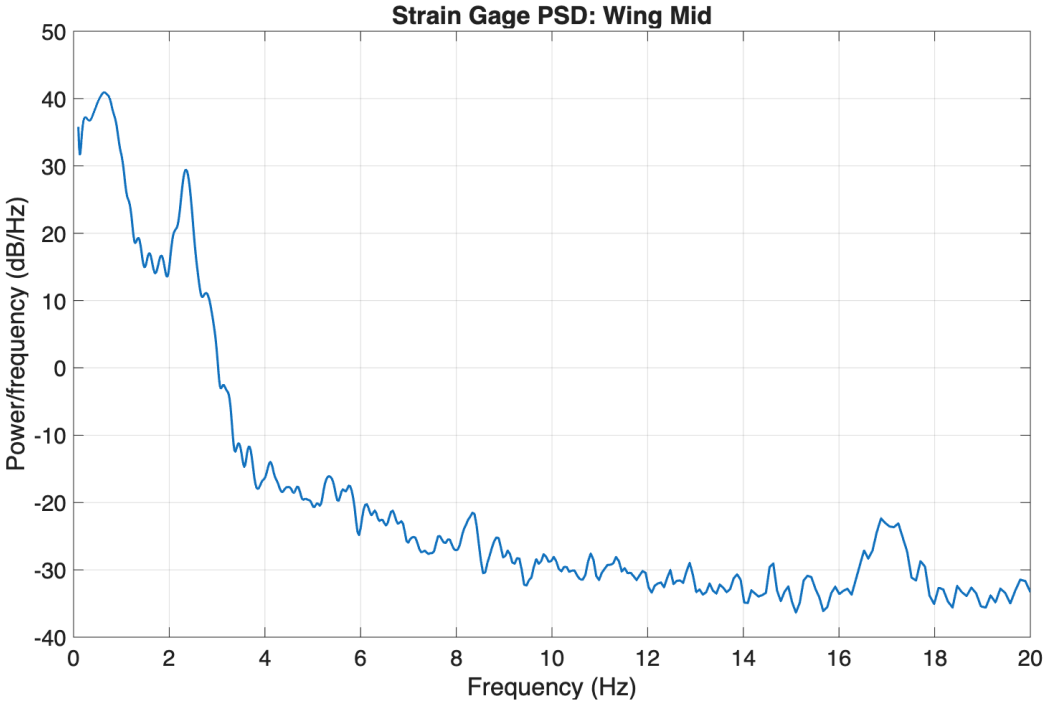



Figure 3.31: 250 Pa elevator sweep 0-25 Hz mid-wing strain gauge power spectral density

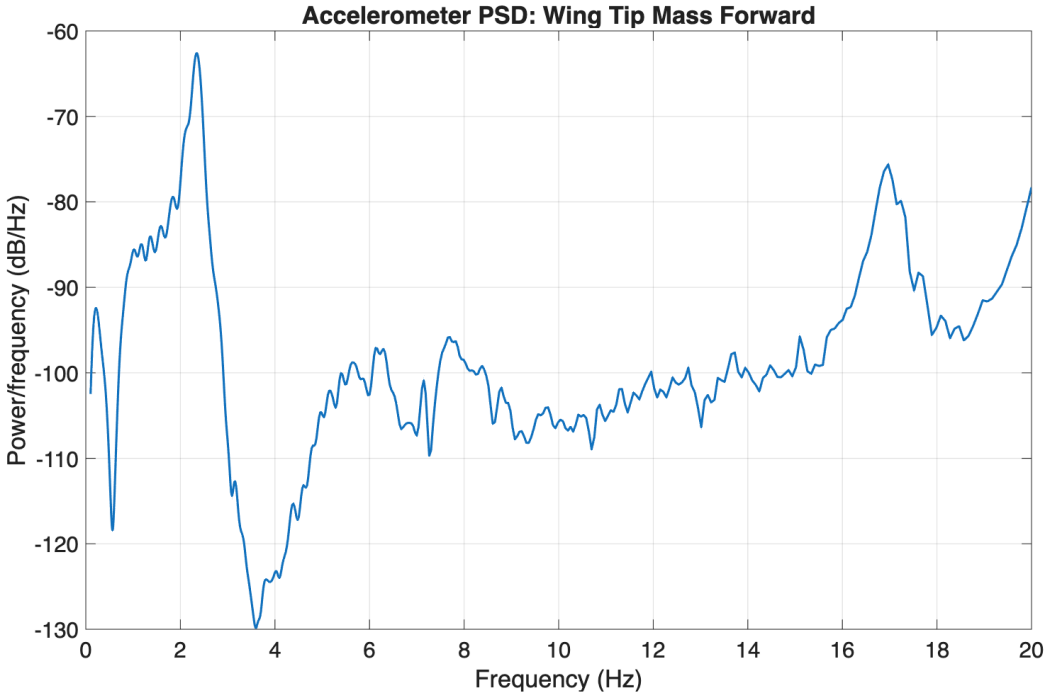



Figure 3.32: 250 Pa elevator sweep 0-25 Hz forward wingtip accelerometer power spectral density

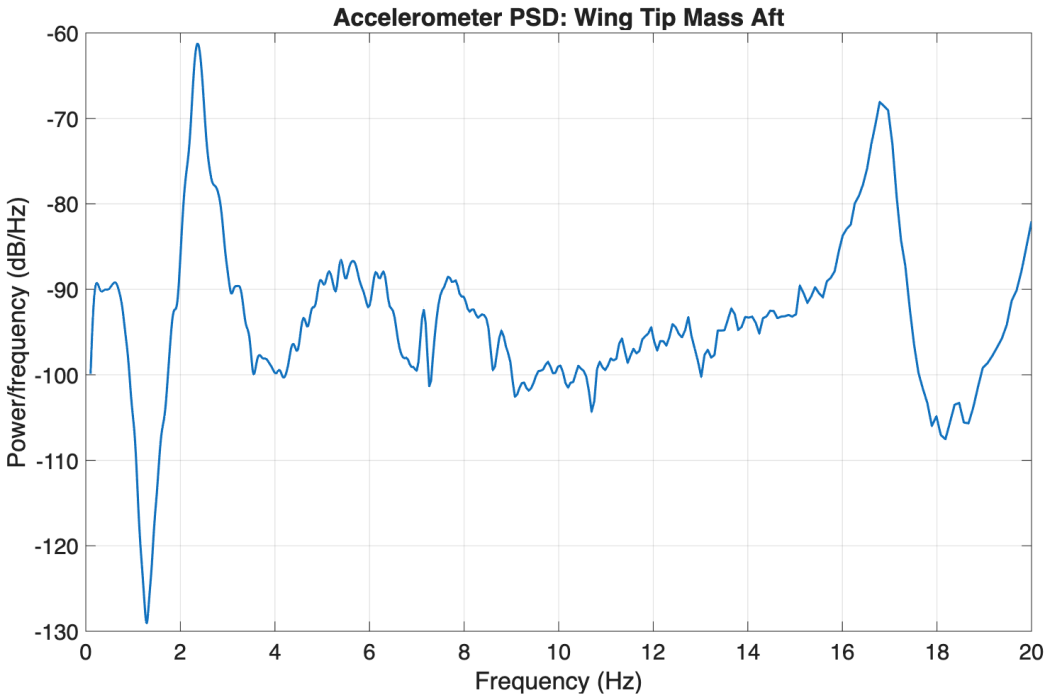



Figure 3.33: 250 Pa elevator sweep 0-25 Hz aft wingtip accelerometer power spectral density

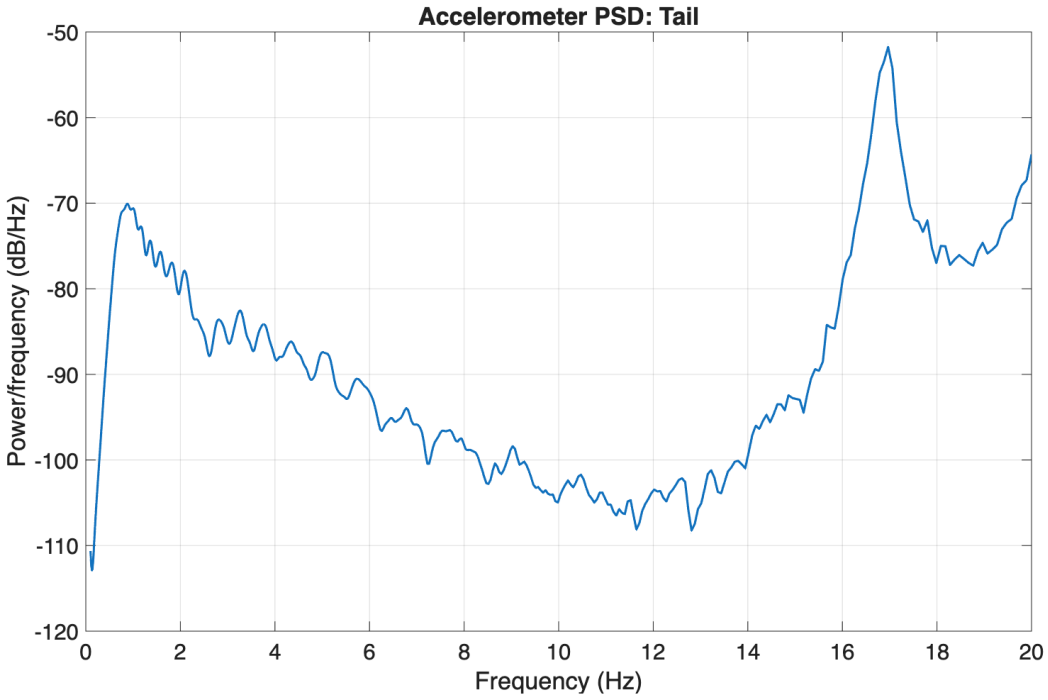



Figure 3.34: 250 Pa elevator sweep 0-25 Hz tail accelerometer power spectral density

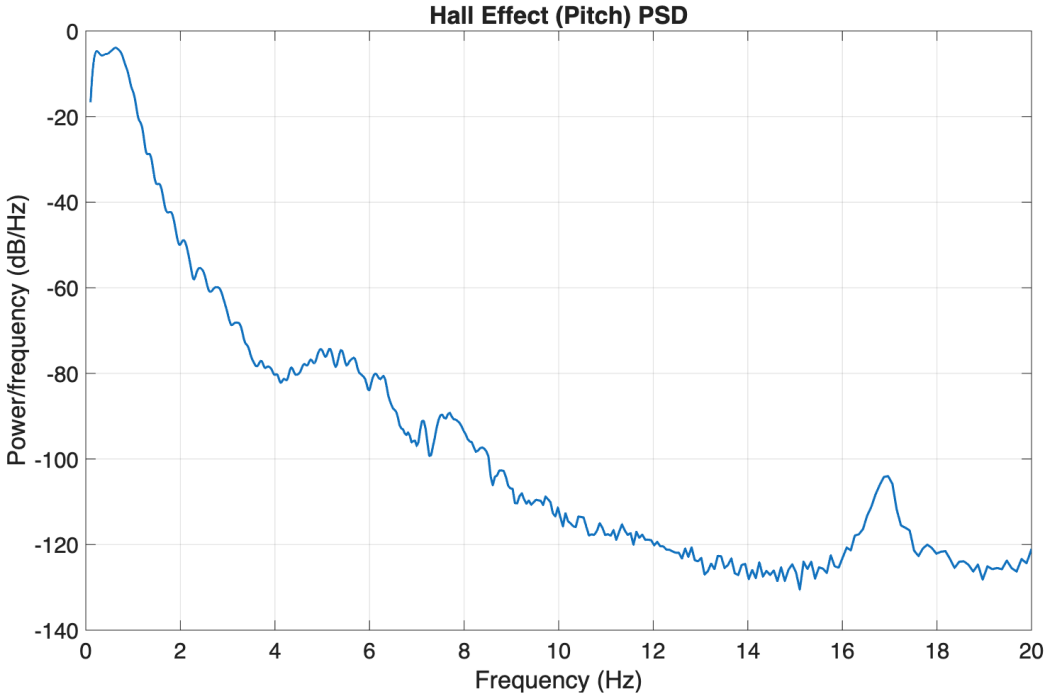



Figure 3.35: 250Pa elevator sweep 0-25Hz Hall-Effect power spectral density

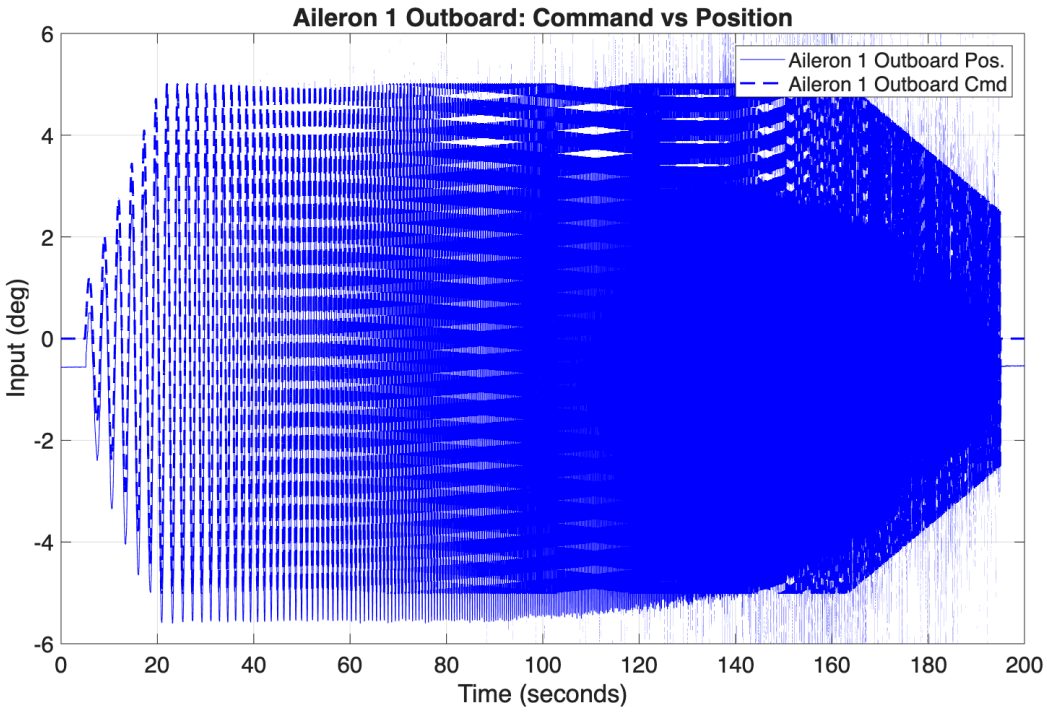



Figure 3.36: 250 Pa outboard aileron sweep 0-25 Hz input data

*Run 119 Strain Gauge Time History Data*

The strain gauge time histories in Figure 3.37 are useful on the same plot to demonstrate their relative effectiveness in terms of response. This plot shows that the mid wing strain gauge can be expected to be the most useful for analysis, followed by the mid fuselage, and then the aft fuselage strain gauges. This data demonstrate, again, the response ineffectiveness of the wing root strain gauges. This led to the relocation of the wing root chordwise strain gauge to to an outboard position on the wing for subsequent weeks of testing.

*Run 119 Accelerometer Time History Data*

The forward wingtip accelerometer frequency-sweep time history (Figure 3.38), while noisy overall, does show one clear peak in activity near the 100 second mark which

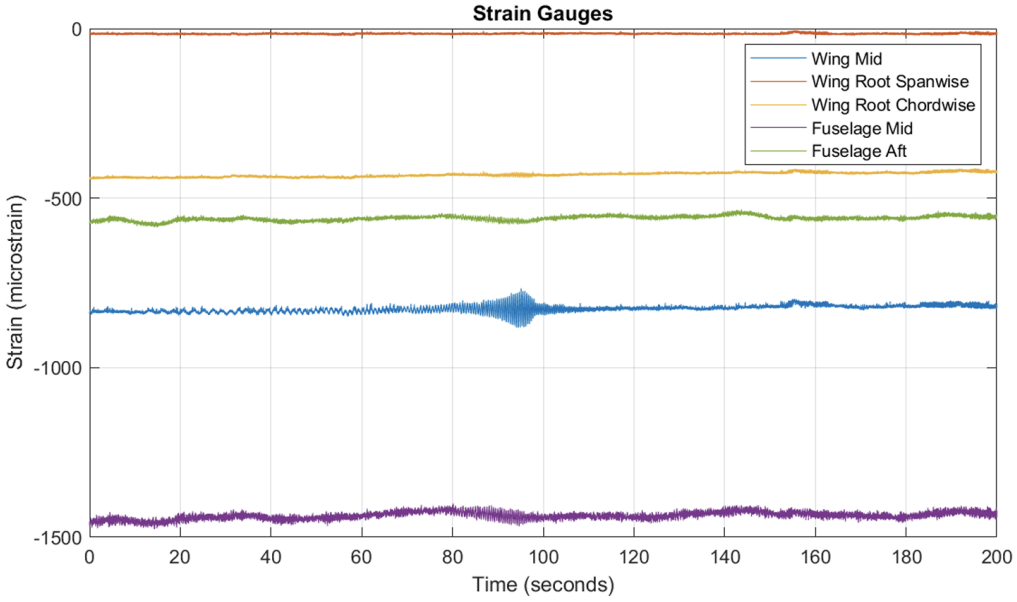



Figure 3.37: 250 Pa outboard aileron sweep 0-25 Hz strain gauge data

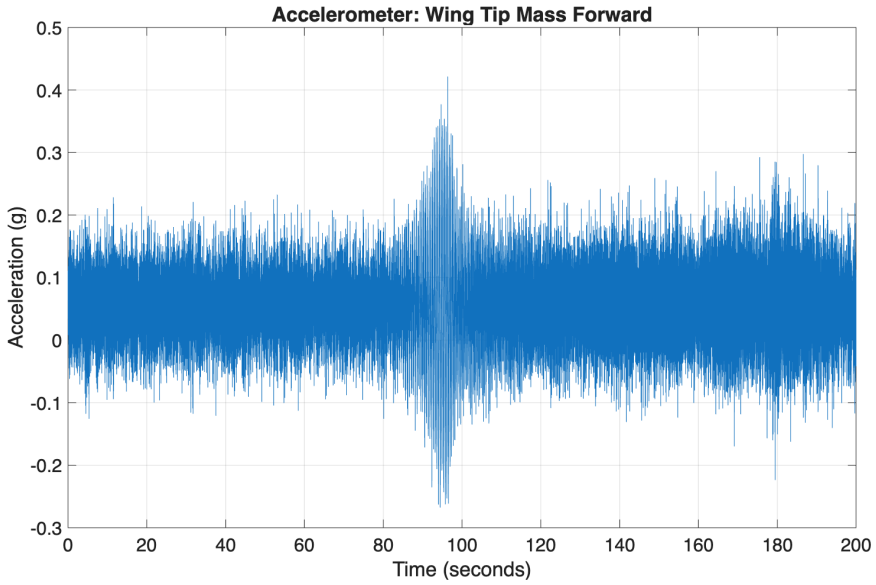



Figure 3.38: 250 Pa outboard aileron sweep 0-25 Hz forward wingtip accelerometer data

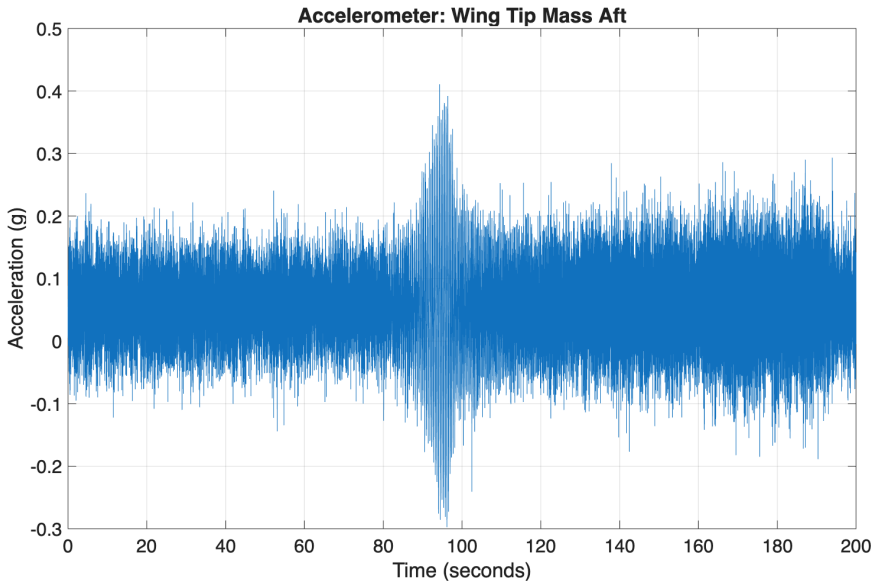



Figure 3.39: 250 Pa outboard aileron sweep 0-25 Hz aft wingtip accelerometer data

corresponds to the time period where the aileron sweep stepped through the 2.3 Hz first wing bending mode, with a second softer peak around the 180 second mark, corresponding to the aileron frequency sweep passing through the 17.3 Hz second wing bending mode.

The aft wingtip accelerometer time history plot (Figure 3.39) shows similar behavior as the forward wingtip accelerometer.

The tail accelerometer time history (Figure 3.40) shows that in the case of the aileron frequency sweep run from run 119, the tail accelerometer does not experience a clear peak in the same way as the wingtip accelerometers do. This difference in response between the tail and wing accelerometers makes sense as the main aeroelastic modes expected to be excited by the aileron are wing based modes while the tail accelerometer would not. Frequency domain analyses (FRFs and PSD) are required to study the makeup of the frequency content.

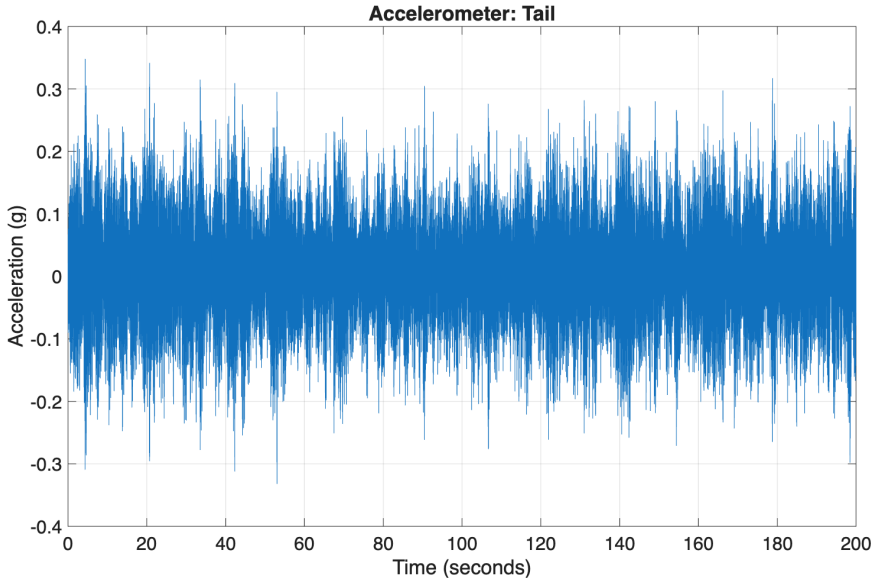



Figure 3.40: 250 Pa outboard aileron sweep 0-25 Hz tail accelerometer data

*Run 119 Post Processed Frequency Domain Data*

*Mid-Wing Strain Gauge FRF Estimates*

Figure 3.41 shows a coherence FRF estimate for the mid-wing strain gauge. Generally, reasonable coherence appears between 0.3 and 3 Hz. It envelopes the short period and the 2.3 Hz first wing bending mode.

Figure 3.42 shows a clear gain peak around 2.3 Hz corresponding to the first wing bending mode that the aileron frequency sweep would be expected to excite well.

The mid-wing strain gauge FRF phase estimate (Figure 3.43) shows the expected rapid drop around 2.3 Hz.

*Aft Fuselage Strain Gauge FRF Estimates*

The aft fuselage strain gauge (Figure 3.44) shows poor coherence with the aileron input. Poor strain gauge coherence will be the subject of future efforts aimed at improving sensor coherence in the model.

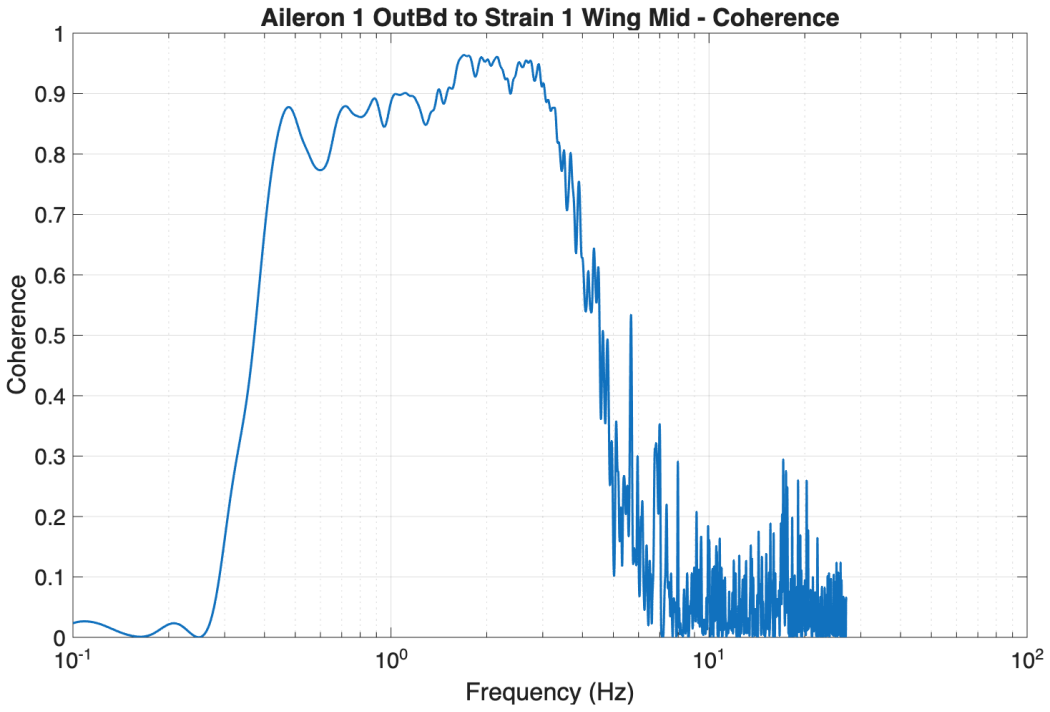



Figure 3.41: 250 Pa outboard aileron sweep 0-25 Hz mid-wing strain gauge FRF coherence estimate

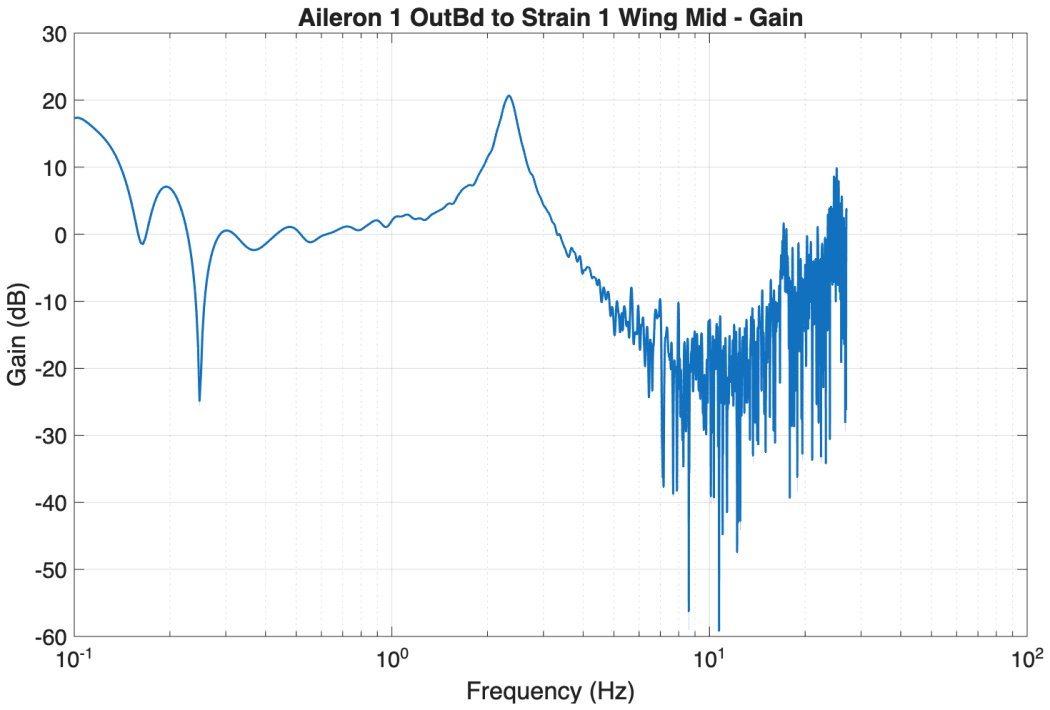



Figure 3.42: 250 Pa outboard aileron sweep 0-25 Hz mid-wing strain gauge FRF gain estimate

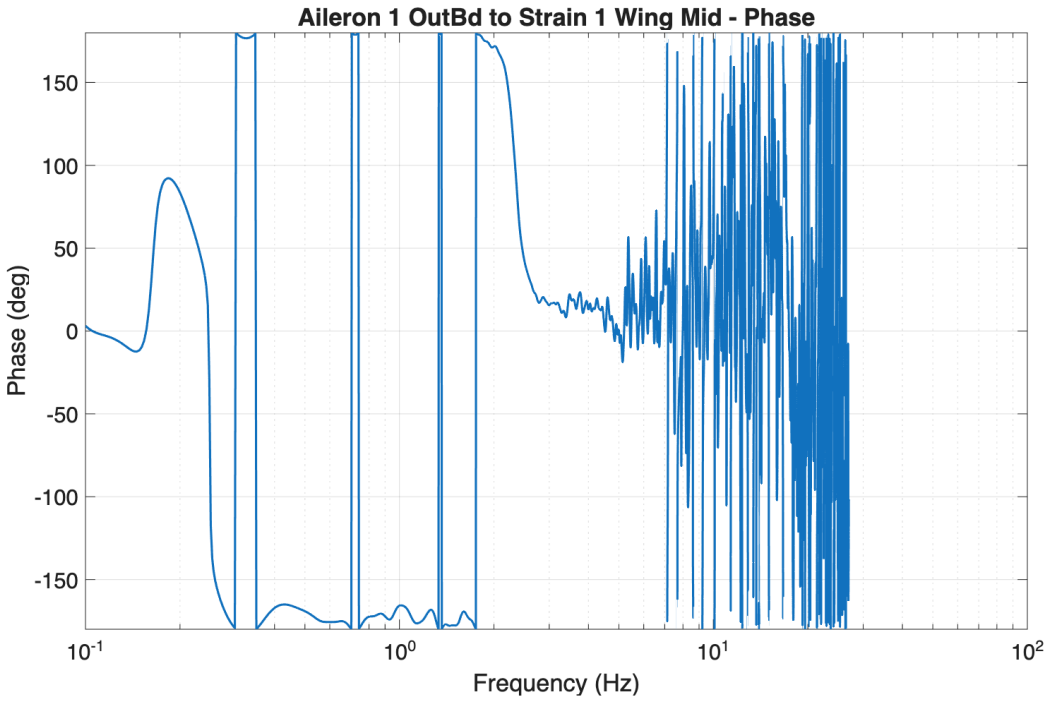



Figure 3.43: 250 Pa outboard aileron sweep 0-25 Hz mid-wing strain gauge FRF phase estimate

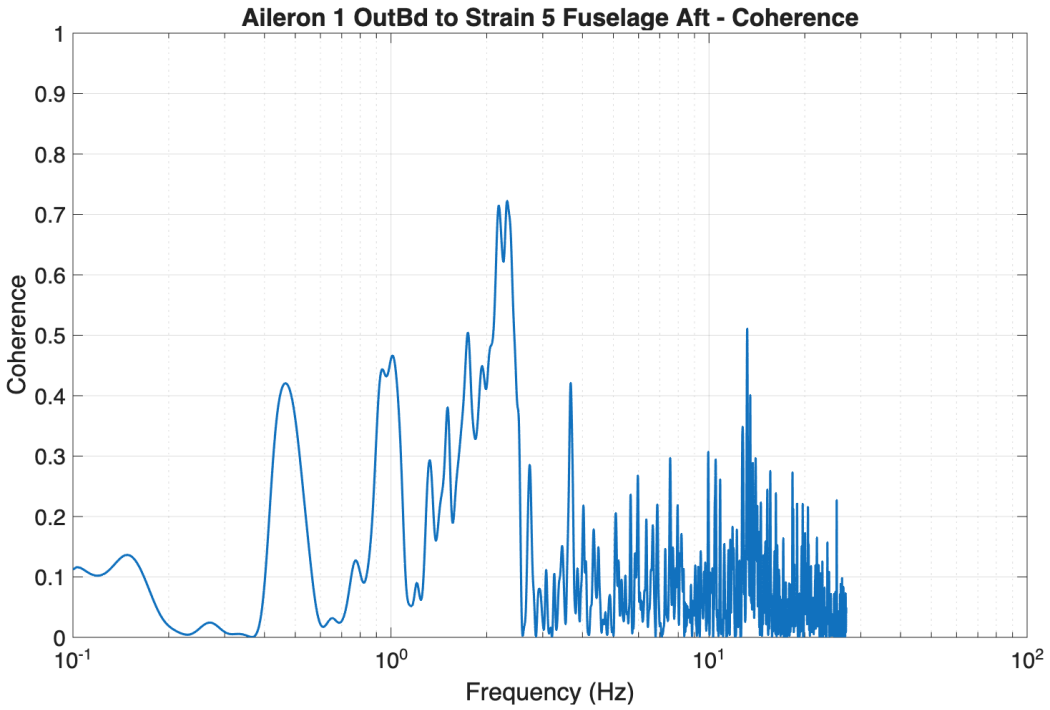



Figure 3.44: 250 Pa outboard aileron sweep 0-25 Hz aft fuselage strain gauge FRF coherence estimate

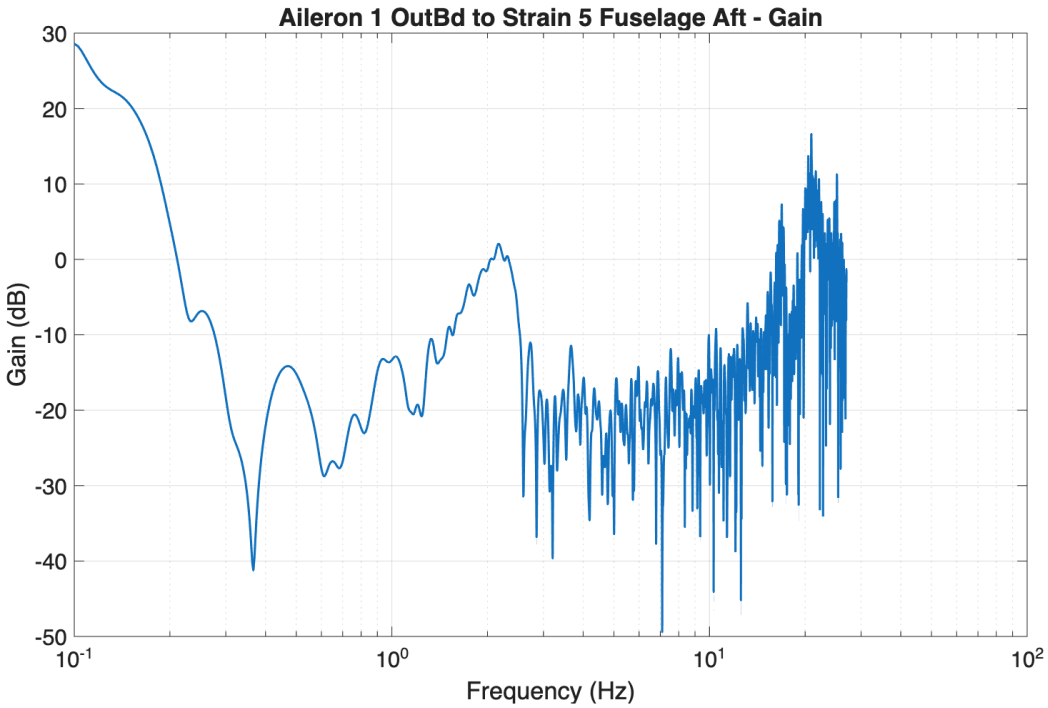



Figure 3.45: 250 Pa outboard aileron sweep 0-25 Hz aft fuselage strain gauge FRF gain estimate

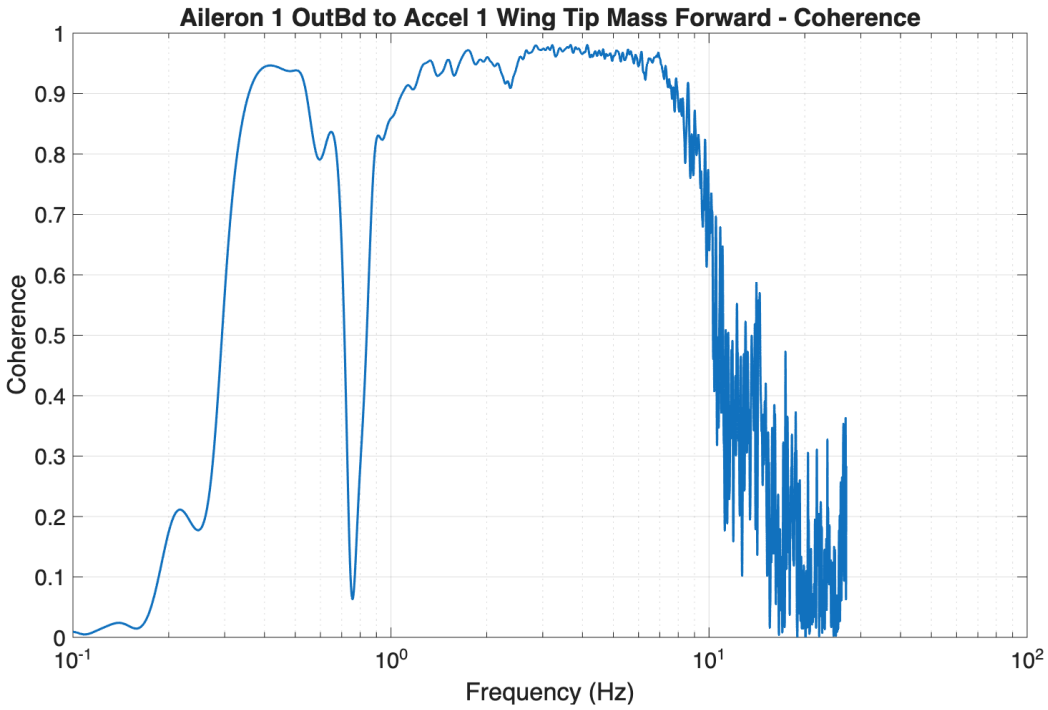



Figure 3.46: 250 Pa outboard aileron sweep 0-25 Hz forward wingtip accelerometer FRF coherence estimate

The gain FRF estimate plot (Figure 3.45), although taken with a grain of salt due to the poor sensor coherence, still shows a peak around 2.3 Hz - the first wing bending mode excited by the aileron sweep in run 119.

*Forward Wingtip Accelerometer FRF Estimates*

The forward wingtip accelerometer FRF coherence estimate plot (Figure 3.46) shows reasonable coherence from around 3 Hz to around 10 Hz with a notch around 0.7 Hz (which is close to the short period frequency).

The gain FRF estimate plot (Figure 3.47) again shows a clear peak at the 2.3 Hz first wing bending mode, as expected.

Again, as expected, the forward wingtip accelerometer phase FRF estimate (Figure 3.48) shows increasing lag around the first wing bending aeroelastic modal frequency.

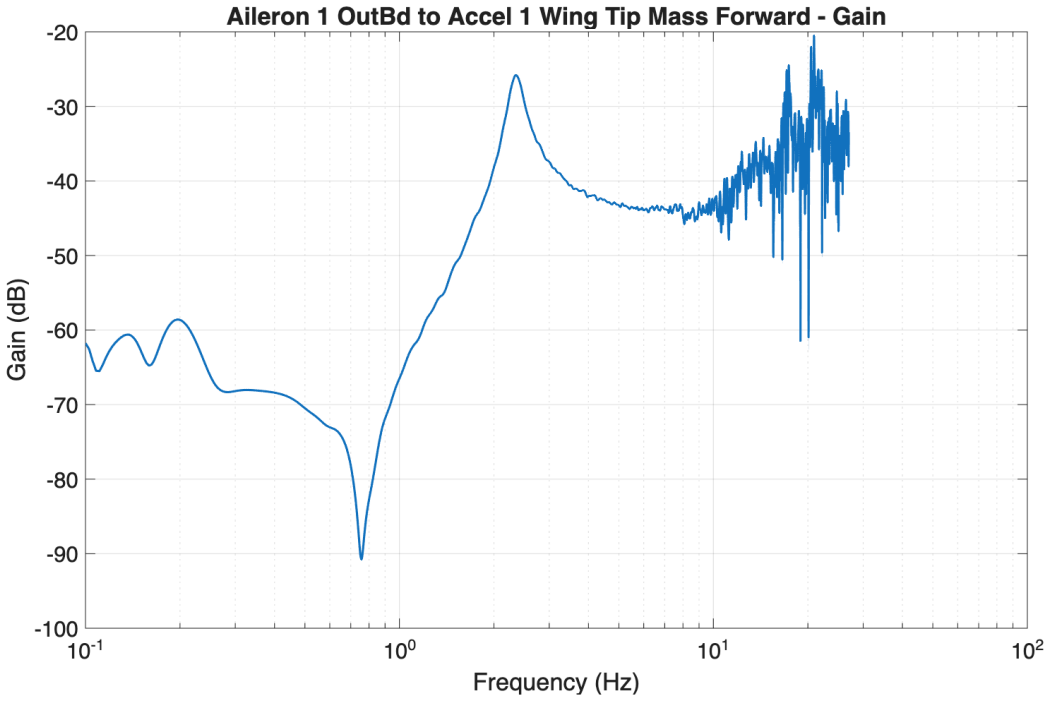



Figure 3.47: 250 Pa outboard aileron sweep 0-25 Hz forward wingtip accelerometer FRF gain estimate

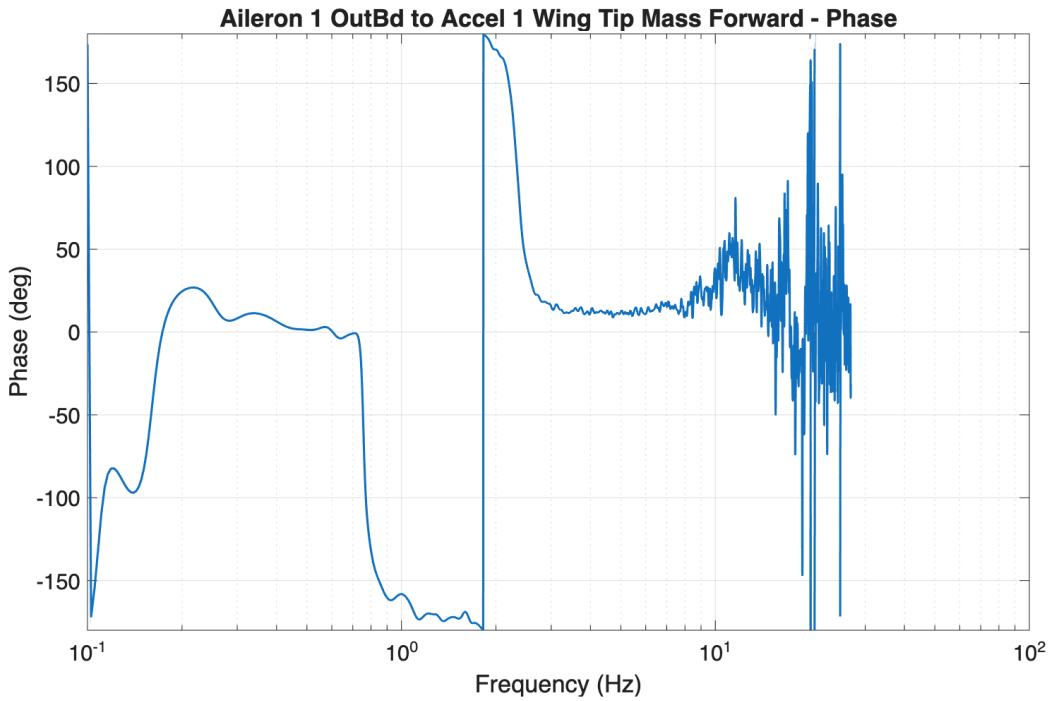



Figure 3.48: 250 Pa outboard aileron sweep 0-25 Hz forward wingtip accelerometer FRF phase estimate

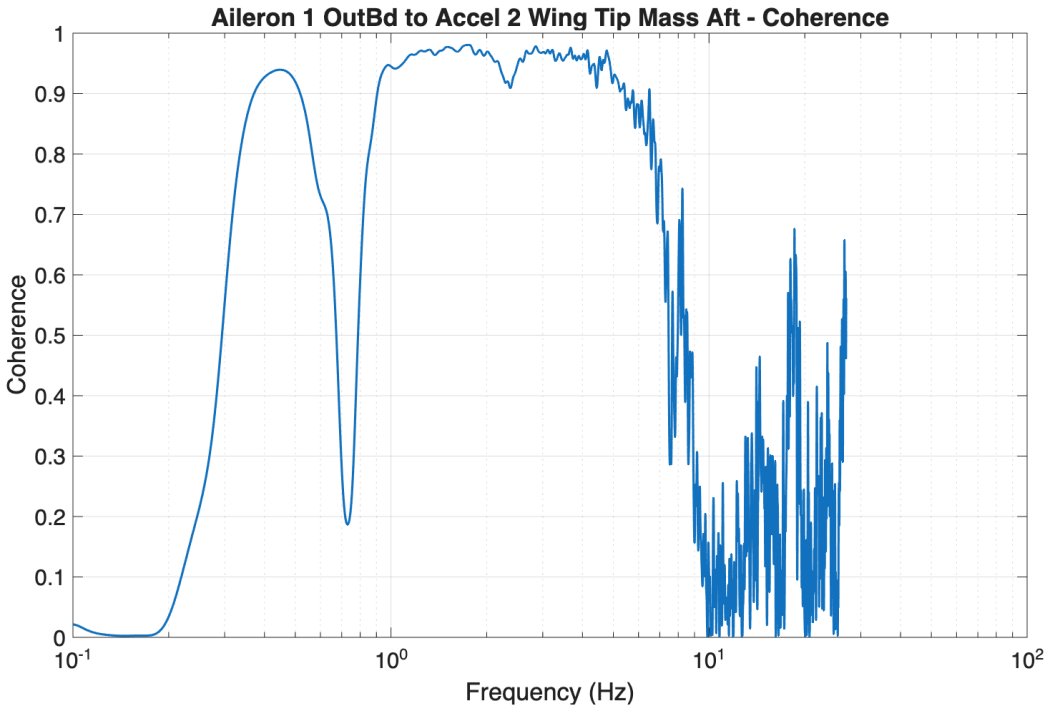



Figure 3.49: 250 Pa outboard aileron sweep 0-25 Hz aft wingtip accelerometer FRF coherence estimate

A significant drop in phase is also evident around the short period frequency.

*Aft Wingtip Accelerometer FRF Estimates*

The aft wingtip FRF estimate plots are discussed below. They illustrate the same points as the forward wingtip accelerometer plots.

The coherence FRF estimate for the aft wingtip accelerometer (Figure 3.49) is actually worse than the forward wingtip accelerometer, holding reasonable coherence only up to around 7 Hz.

Like the forward wingtip accelerometer FRF estimate (Figure 3.47), the aft wingtip accelerometer (Figure 3.50) shows a gain peak at the 2.3 Hz first wing bending aeroelastic mode, but the content is noisy otherwise.

The phase FRF estimate for the aft wingtip accelerometer (Figure 3.51) also shows

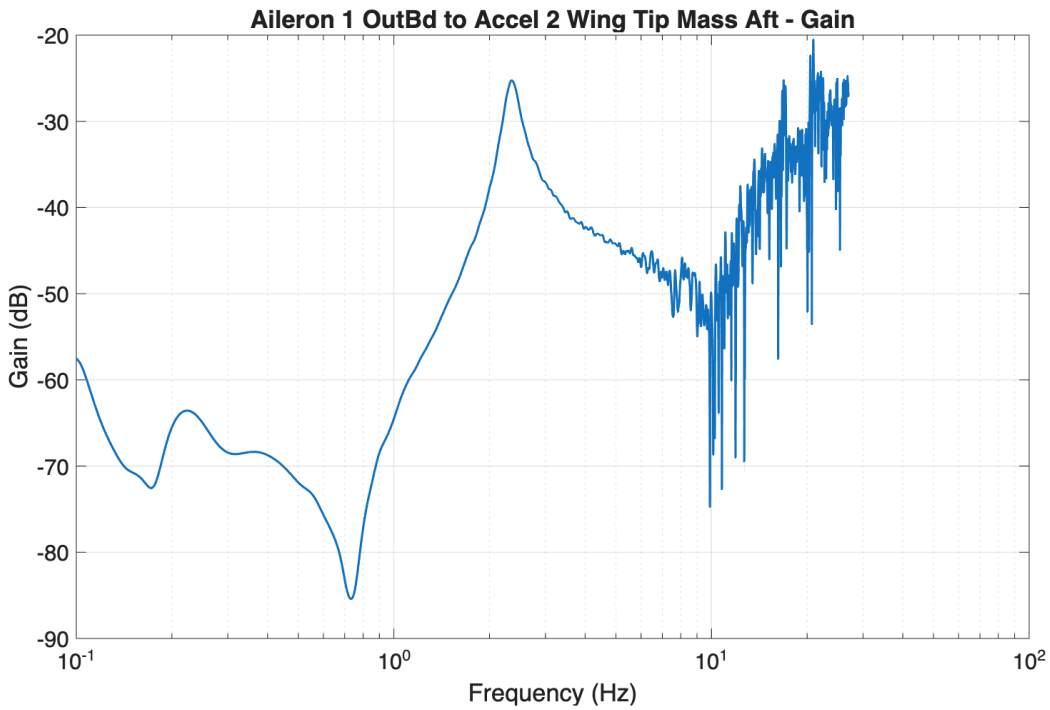



Figure 3.50: 250 Pa outboard aileron sweep 0-25 Hz aft wingtip accelerometer FRF gain estimate

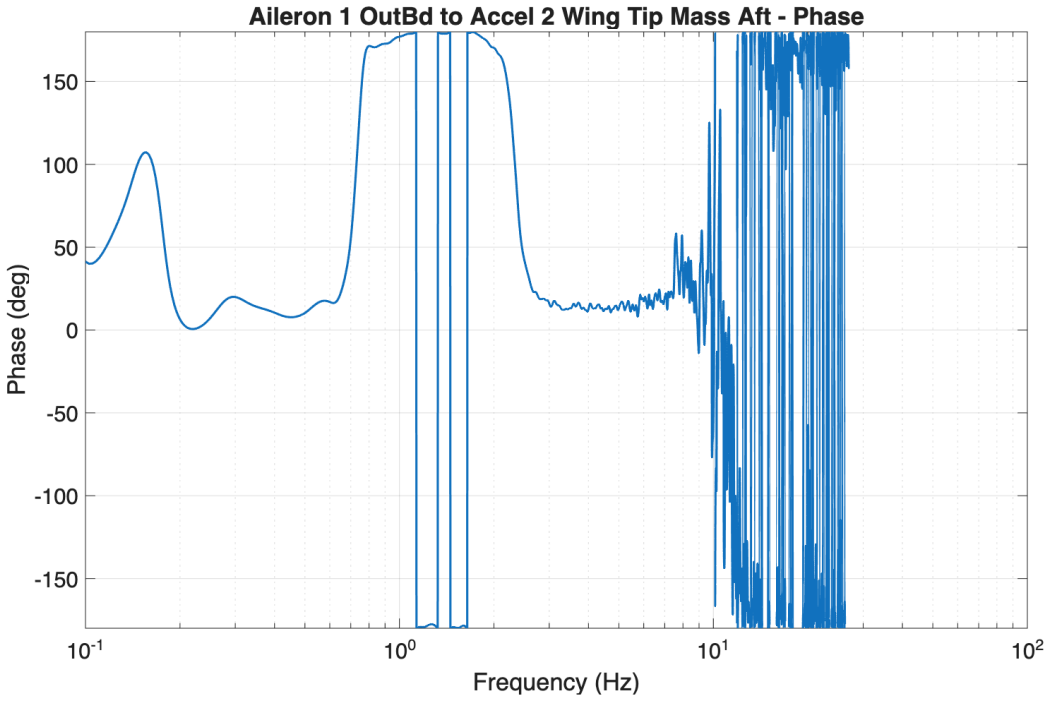



Figure 3.51: 250 Pa outboard aileron sweep 0-25 Hz aft wingtip accelerometer FRF phase estimate

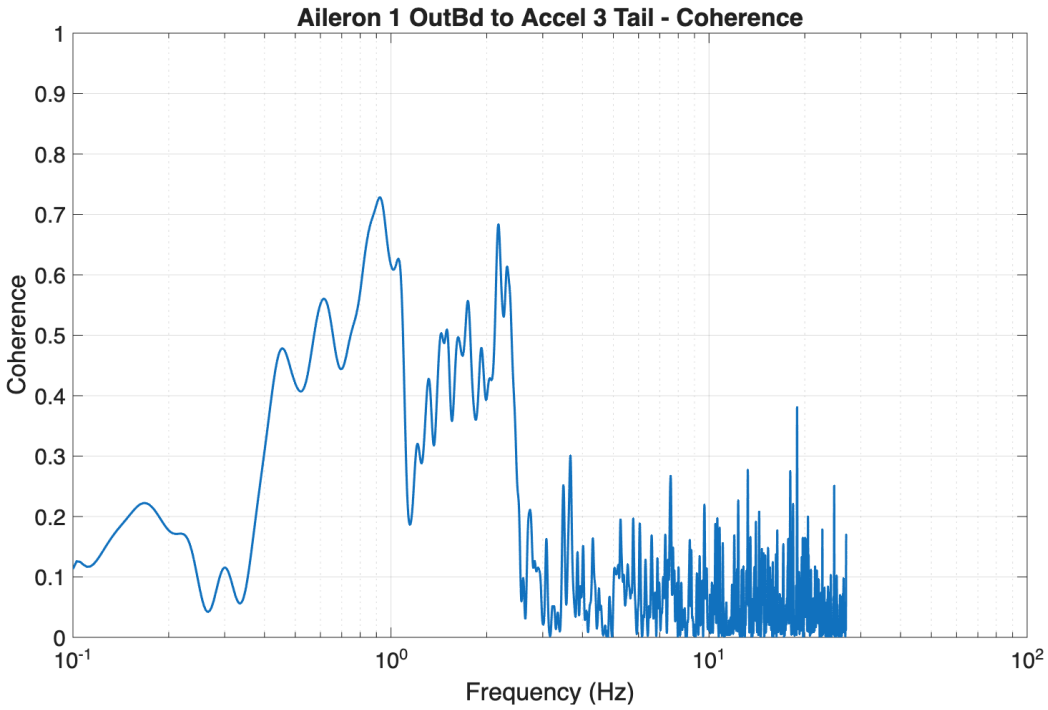



Figure 3.52: 250 Pa outboard aileron sweep 0-25 Hz tail accelerometer FRF coherence estimate

a phase lag around the peak frequency of 2.3 Hz for the wing bending aeroelastic mode.

*Tail Accelerometer FRF Estimates*

The tail accelerometer I/O data show poor coherence in Figure 3.52. Like the aft fuselage strain gauge (Figure 3.44), this sensor is poorly placed to observe the main poles of interest.

Although there is a peak in the gain FRF estimate plot (Figure 3.53) for the tail accelerometer around the first wing bending mode frequency, there is not much more useful content.

The phase FRF estimate plot (Figure 3.54) is too noisy. The location of the tail accelerometer sensor had to be changed in later work.

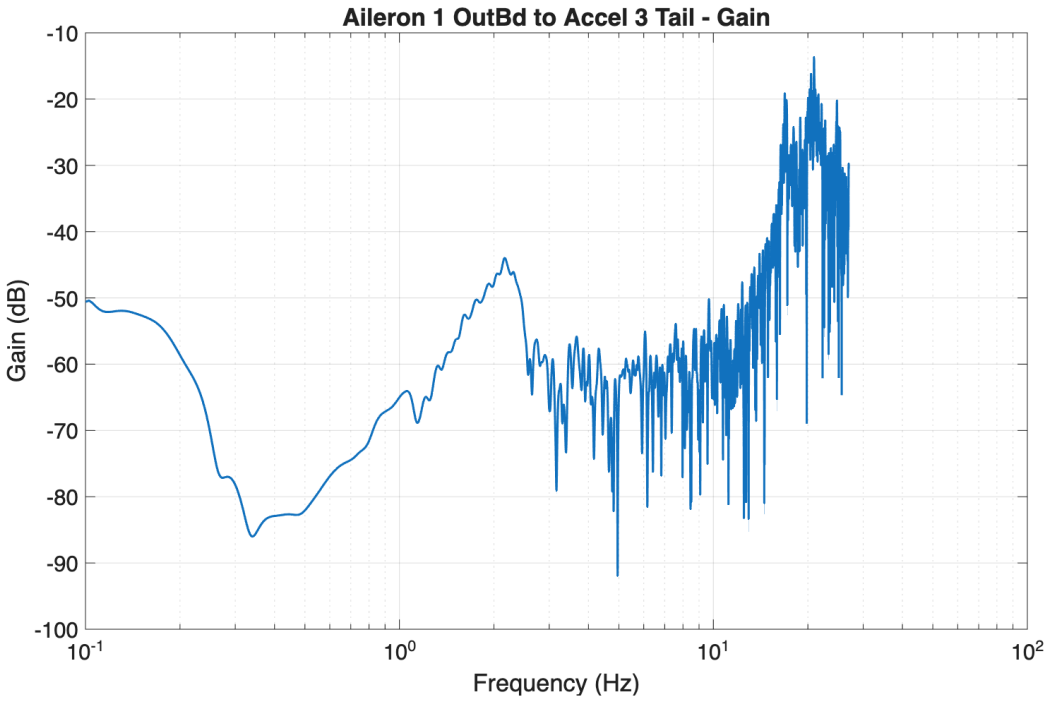



Figure 3.53: 250 Pa outboard aileron sweep 0-25 Hz tail accelerometer FRF gain estimate

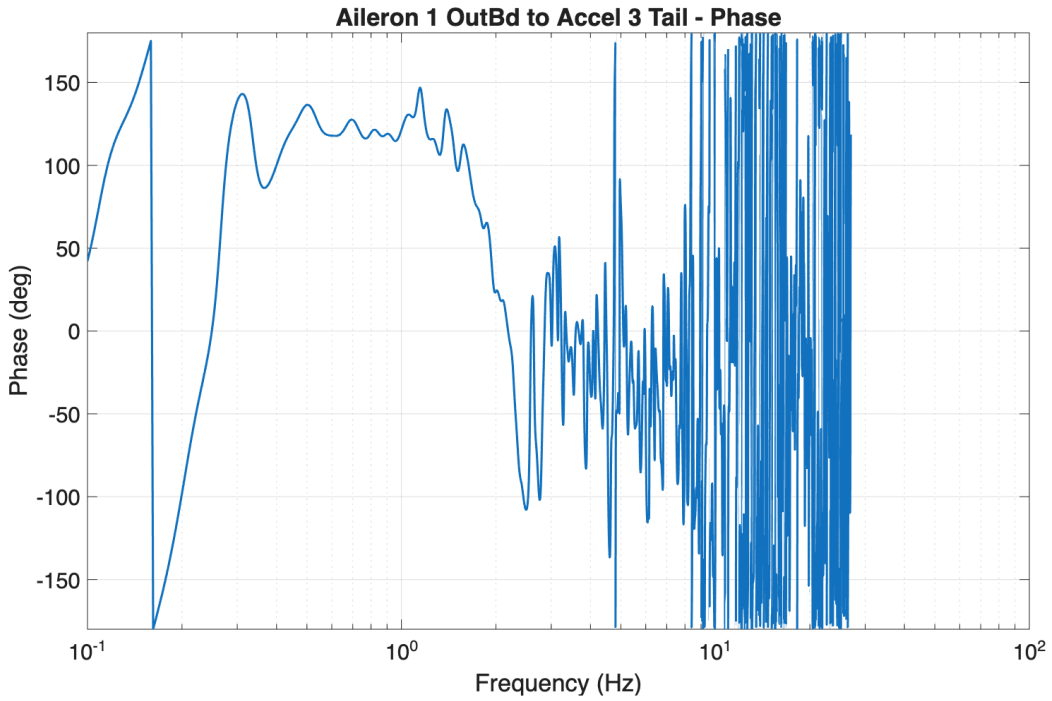



Figure 3.54: 250 Pa outboard aileron sweep 0-25 Hz tail accelerometer FRF phase estimate

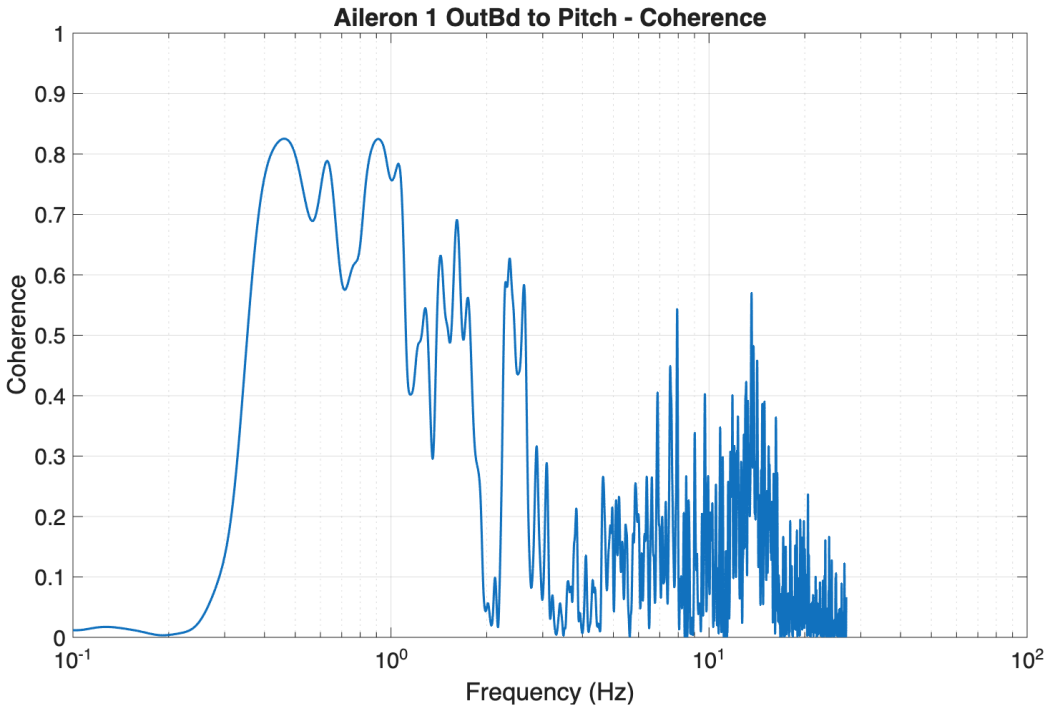



Figure 3.55: 250 Pa outboard aileron sweep 0-25 Hz pitch FRF coherence estimate

*Hall Effect (pitch) FRF Estimates*

The Hall Effect FRF coherence estimate plot shows poor coherence overall. The ailerons do not produce enough pitching moment, probably because of the short moment arms involved, and do not excite root rotational motions enough. The resulting gain and phase plots do not provide useful information (Figures 3.56 and 3.57).

*Power Spectral Density (PSD) Analysis*

All of the PSD plots (Figures 3.58, 3.59, 3.60, 3.61, 3.62, 3.63, 3.64) that follow show the same type of information with a peak at the 2.3 Hz first wing bending mode shape and another at the 17.3 Hz second wing bending mode. They do not seem to capture the short-period frequency.

Even the tail accelerometer PSD captures the 2.3 and 17.3 Hz peaks despite the

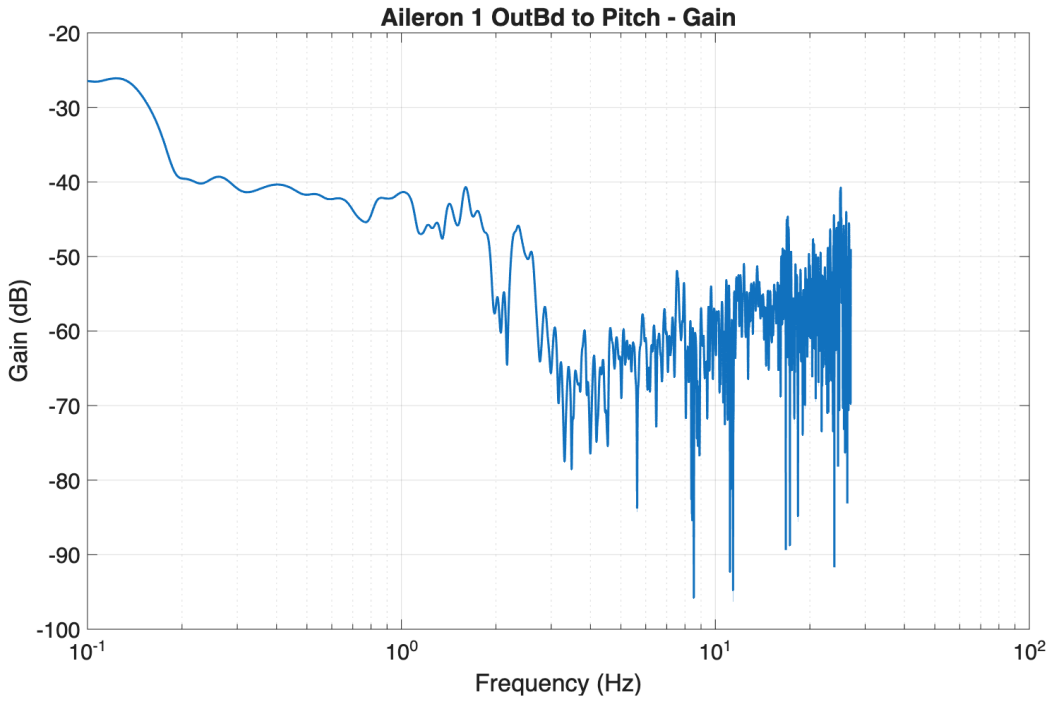



Figure 3.56: 250 Pa outboard aileron sweep 0-25 Hz pitch FRF gain estimate

sensor not being ideally placed to provide useful FRFs.

The Hall-Effect Sensor does not "see" much response in the low frequency range as reflected by the PSD plot, but it still manages to pick up the 17.3 Hz second wing bending mode.

### *3.2.3 Wind Tunnel Entry 1 Lessons Learned*

The results of the exploratory wind tunnel tests, shown in the figures discussed above, demonstrate some concrete successes in obtaining useful FRFs for MARGE-II in its very early stage of development. Areas of improvement for the model were also identified based on the tests. PSD results confirmed, in general, the presence of aeroelastic modal participation in the dynamics of the system with key observable peaks appearing at 2.3 Hz, and 17.3 Hz. In the FRF estimation work, poor FRF coherence was observed for various input-output pairs - particularly in the strain

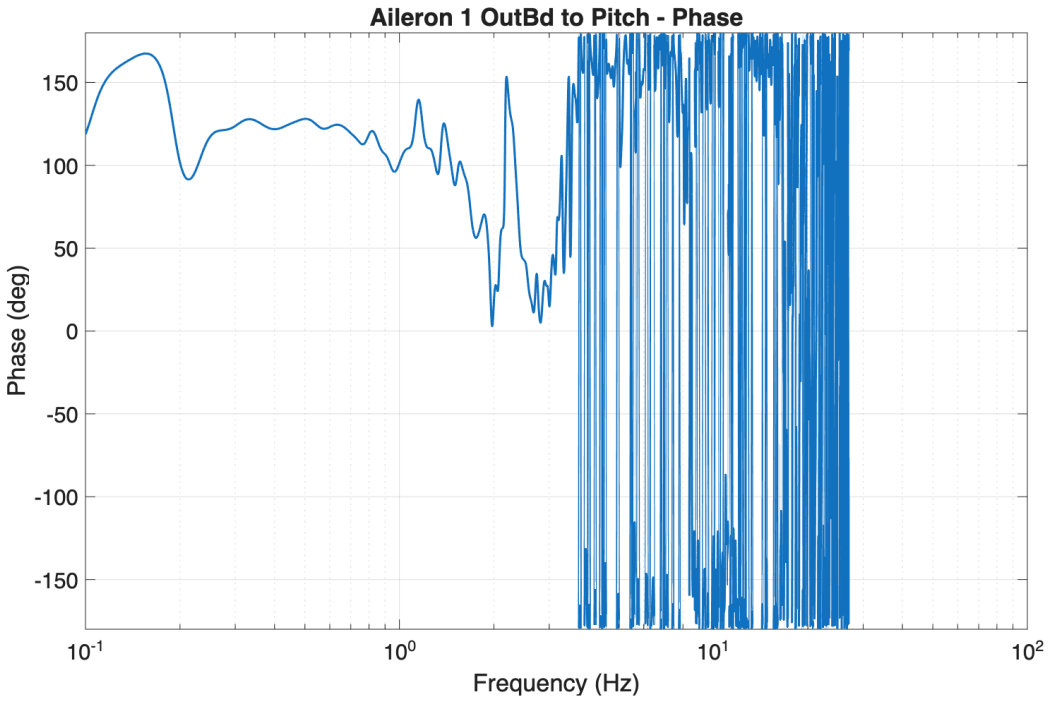



Figure 3.57: 250 Pa outboard aileron sweep 0-25 Hz pitch FRF phase estimate

gauge results. Some of the strain gauge results were excluded from this report, as they had particularly poor coherence and did not show much in the way of modal content. The conclusion was, of course, that there was a need to change locations of certain sensors.

In almost all cases the sensors as placed originally on MARGE-II failed to observe the 6.4 Hz first fuselage bending mode. When initially evaluated in a clamped state for the first GVT that was performed to confirm that structural mode shapes were within controllable frequency ranges, the fuselage bending mode was observed, however slightly, with the laser vibrometer (Figure 3.2). The fuselage torsion mode that should show around 15.4 Hz was also not observed by the sensors in the first week of wind tunnel testing. This failure is due to poor sensor placement for the fuselage strain gauges and accelerometer.

Because the wind tunnel model is free to rotate around the pitch axis, the first fuse-

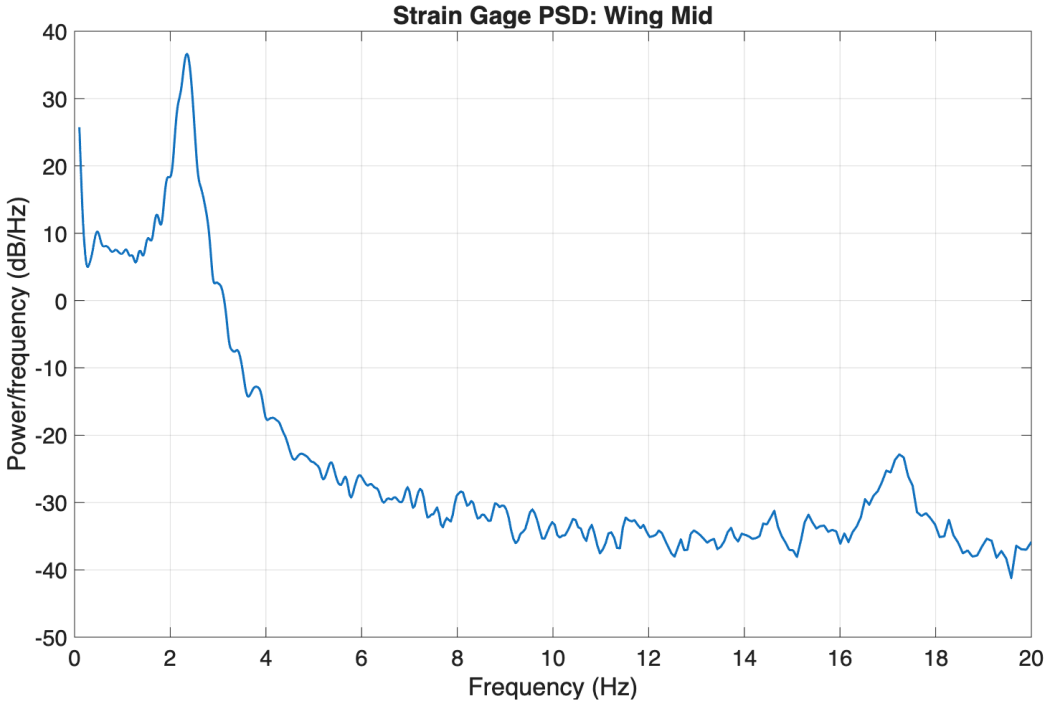



Figure 3.58: 250 Pa outboard aileron sweep 0-25 Hz mid-wing strain gauge power spectral density

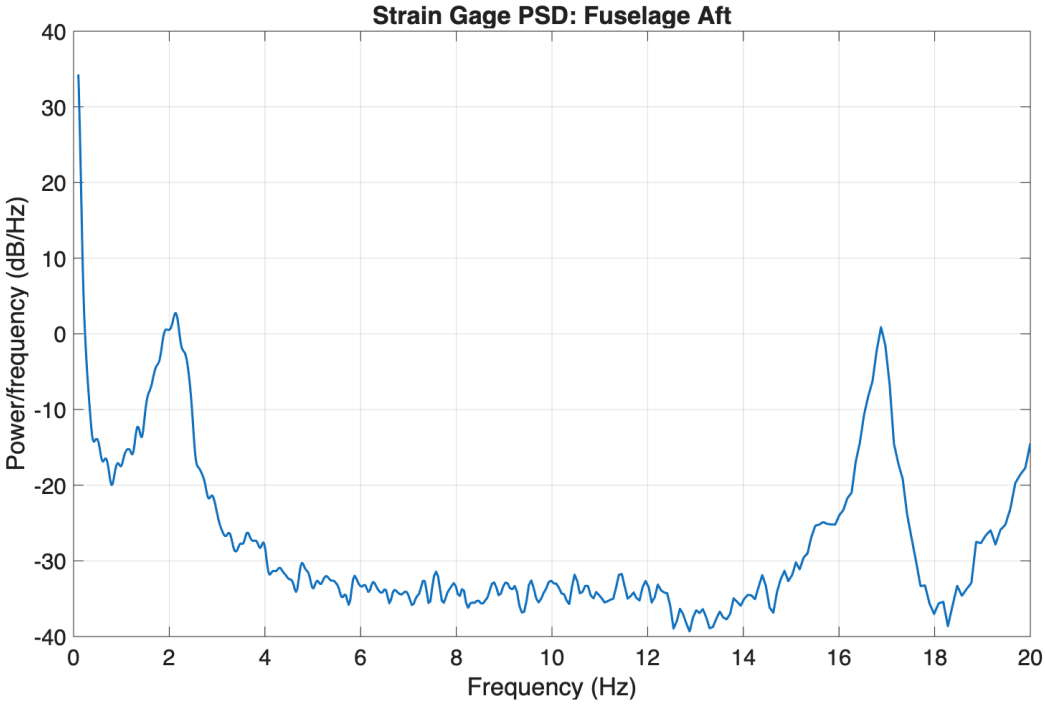



Figure 3.59: 250 Pa outboard aileron sweep 0-25 Hz aft fuselage strain gauge power spectral density

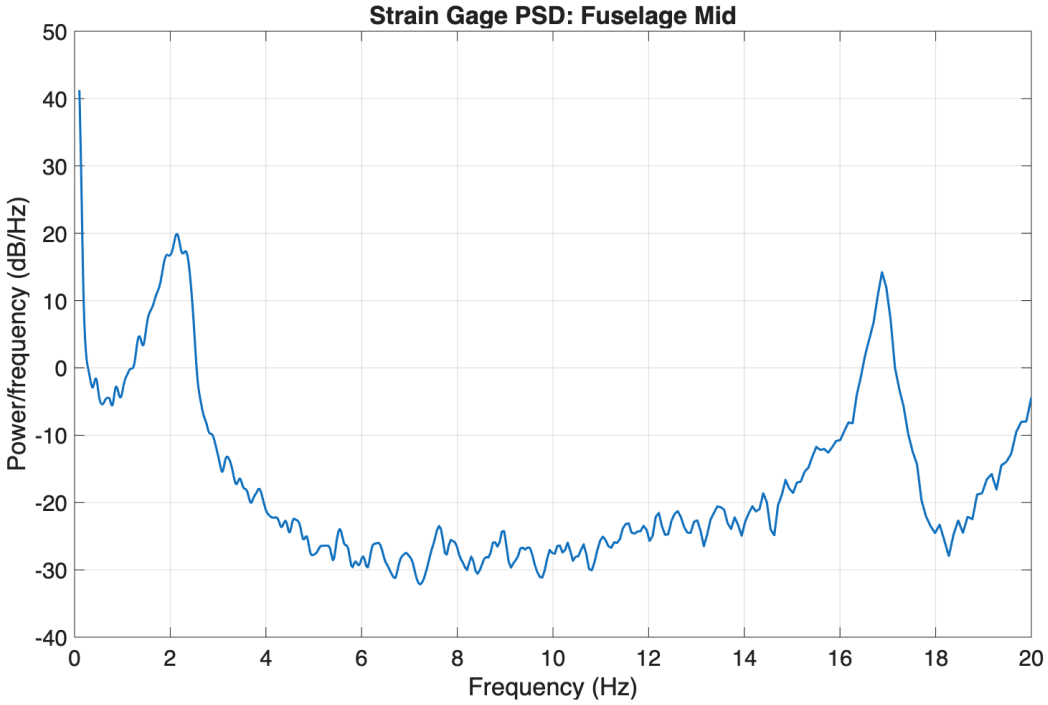



Figure 3.60: 250 Pa outboard aileron sweep 0-25 Hz mid-fuselage strain gauge power spectral density

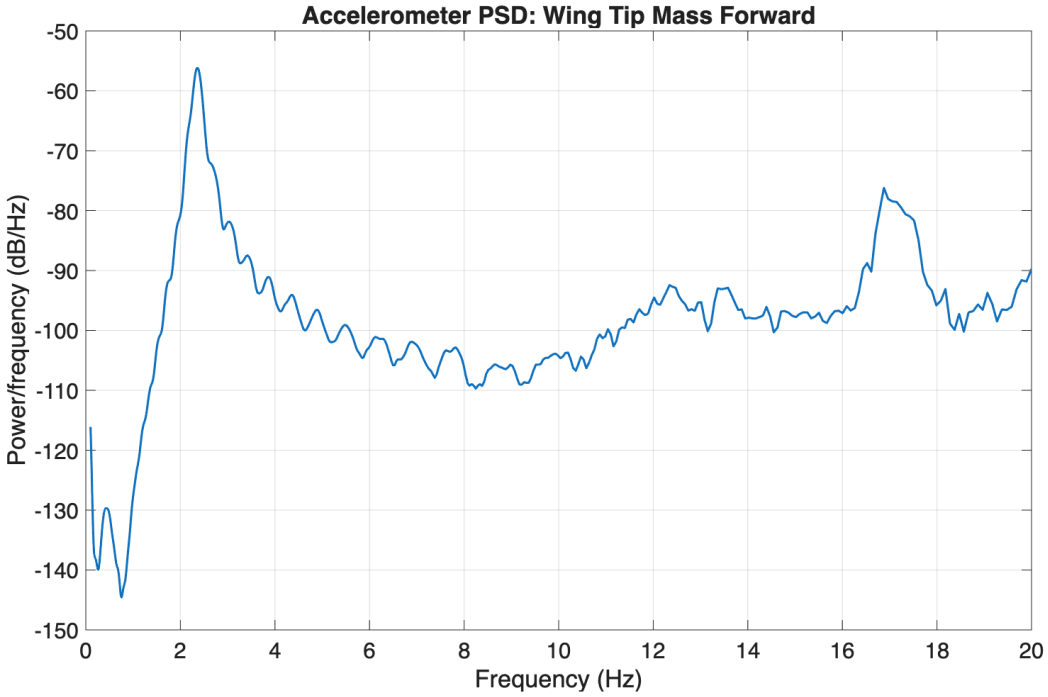



Figure 3.61: 250 Pa outboard aileron sweep 0-25 Hz forward wingtip accelerometer power spectral density

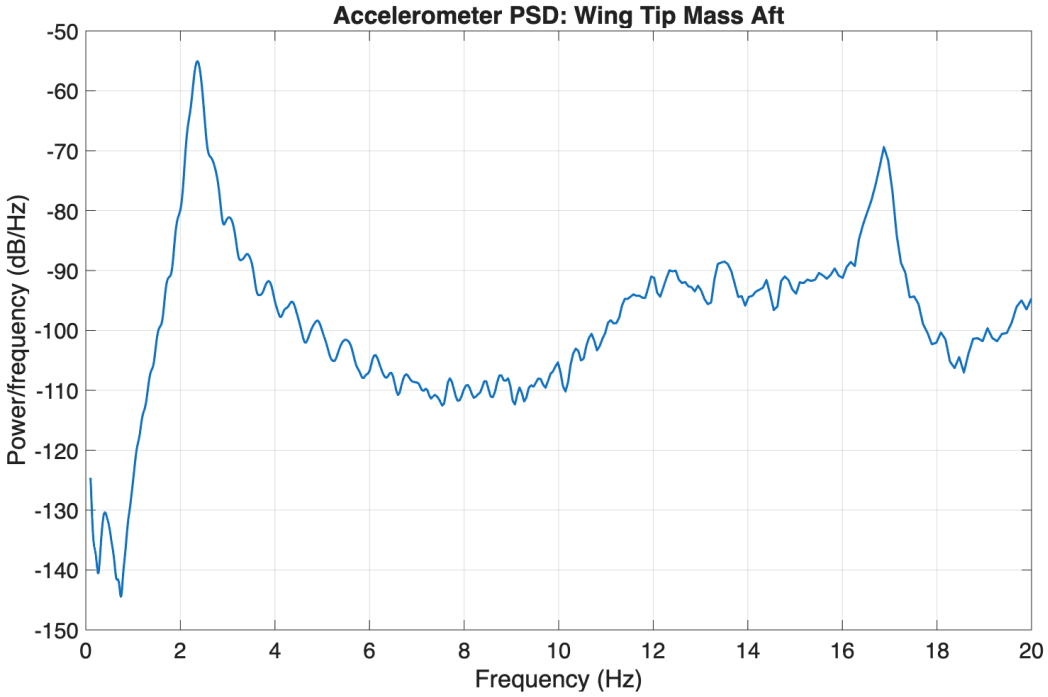



Figure 3.62: 250 Pa outboard aileron sweep 0-25 Hz aft wingtip accelerometer power spectral density

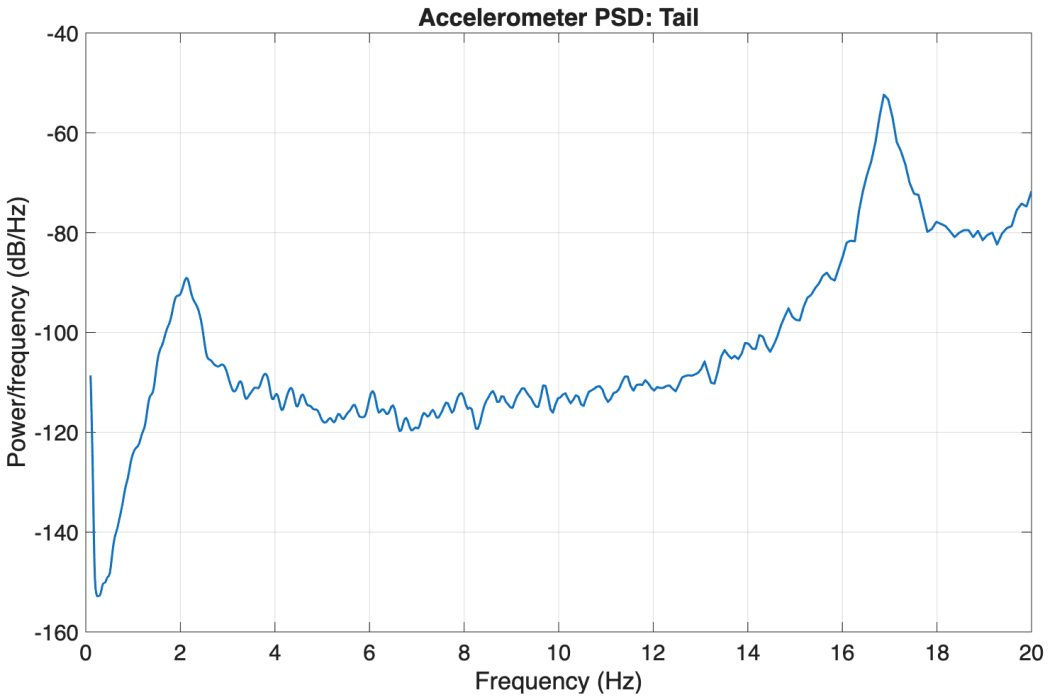



Figure 3.63: 250 Pa outboard aileron sweep 0-25 Hz tail accelerometer power spectral density

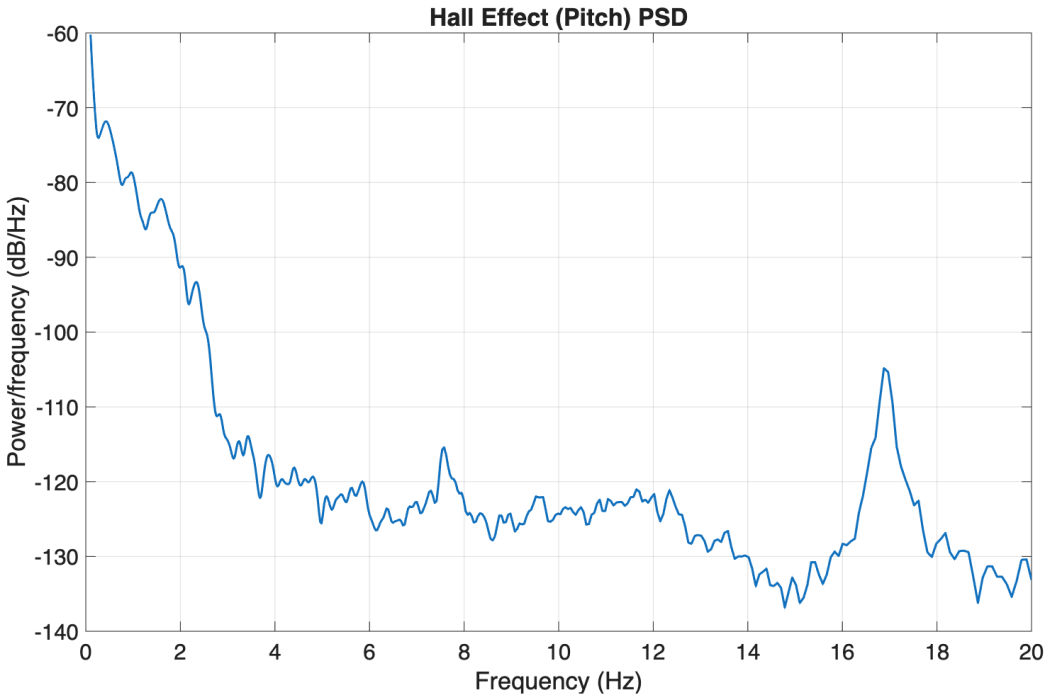



Figure 3.64: 250 Pa outboard aileron sweep 0-25 Hz Hall-Effect sensor power spectral density

lage bending mode differs from the fixed-root condition observed during the Ground Vibration Test (GVT). Due to this pinned, free-to-rotate boundary condition, the fuselage accelerometers and strain gauges fell directly on the modal nodes, making it impossible to capture certain modal content. Similarly, the torsion mode was difficult to detect; sensors placed along a thin beam experience minimal displacement because of their small moment arms relative to the center of rotation.

Additionally, a "rocking" mode was visually observed, pointing to freeplay in the rotational shaft housing assembly. This observation led to improvements later that reduced the freeplay.

The tests (both GVT and wind tunnel tests) were very useful for identifying areas of weakness and guiding necessary improvements. The thesis focuses on the initial development of MARGE-II and the exploratory testing that was required to guide improvements. Later work, to be described in upcoming papers [20, 21], implemented the required improvements.

Overall, several steps were identified that were needed to improve input to output coherence for MARGE-II. In addition to the longitudinal stability fixes as described, there is freeplay at various connection points in the model that required tightening up. Electrical noise is also an issue in the sensor output signal, and there are several small fixes that can be implemented to reduce noise. Finally, the model in its original configuration was aerodynamically "noisy", especially around the flat sharp edges of the pivot block and the tip mass. "Cleaning up" the airflow was required to reduce flow field turbulence and the resulting input and output noise.

### *3.3 Next Steps*

These initial results drove the decision to utilize Week 2 of the exploratory wind tunnel entry to make several changes to the model. The most pressing adjustments were fixing the pitch instability. The wing's axis of rotation was moved from 45% chord to 29% chord through a minor structural modification, and the tail span was

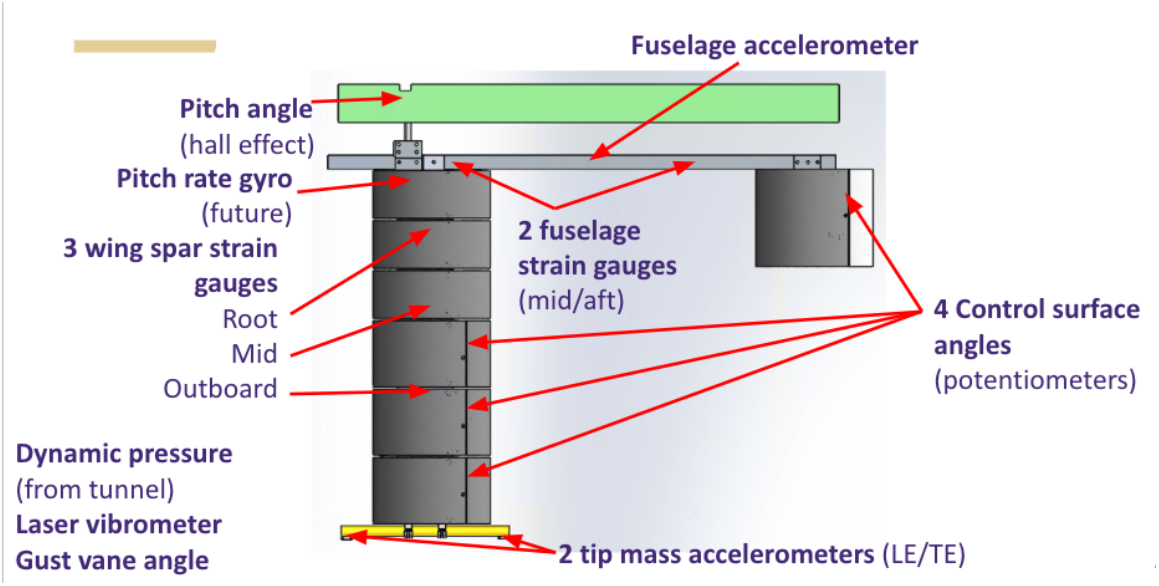



Figure 3.65: MARGE-II with updated sensor locations

increased by 2 inches by printing a longer aero-shell.

To improve test observability, one accelerometer was moved from the model's tail to a mid-fuselage location, and two strain gauges were moved: one from the wing root chordwise orientation to an outboard location spanwise orientation on the wing spar, and the other wing root spanwise oriented strain gauge was moved 2" further outboard of the wing root (see Figure 3.65). These model changes enable the sensors to capture all of the structural modes of interest much more effectively.

The noise issues were addressed by adding a capacitor to the shield-to-ground drain circuits on the signal conditioning boards, which reduced electrical noise generated by the gust-generator system motor. MOLEX connections in the sensing circuits were also replaced with directly soldered connections which also contributed to reduced data noise.

The main bearing at the model's pitch axis was shimmed to reduce the rocking motion due to the freeplay. Aerodynamic fairings were also added to the model both at the wing tip and the model's root in an effort to greatly clean up the model's



Figure 3.66: MARGE-II in 3x3 wind tunnel with updates

aerodynamic characteristics.

Upcoming SciTech papers ([20] and [21]) describe those improvements. The model in its current state (at the time of completing this thesis) is shown in Figure 3.66

# Chapter 4

# CONCLUSION

The thesis described the development of the MARGE-II active aeroelastic wind tunnel model in its early stages, including design goals, design and construction details, ground and wind tunnel exploratory tests, and the needed improvements that the results of those tests called for and guided.

The resulting Model for Aeroelastic Response to Gust Excitation II (MARGE-II) is a low-cost accessible test platform for active aeroelastic control experimentation. It improves on the success of its predecessor, MARGE-I, by providing expanded control and sensing capabilities, improved noise characteristics, and additional modal characteristics that are controllable via higher bandwidth servo motors. MARGE-II maintains the modular design philosophy of MARGE-I and provides greater ease of access for model adjustments. The model remains in active development in the University of Washington's 3x3 Wind Tunnel and will be used as an extremely versatile test platform in the years to come.

# BIBLIOGRAPHY

[1] Jake Quenzer. *Tools and Methods Toward the Advancement of Flight Control for Flexible Aircraft*. PhD thesis, University of Washington, 2019.

[2] J. D. Quenzer, A. Zongolowicz, K. A. Hinson, B. Barzgaran, E. Livne, M. Mesbahi, and K. Morgansen. Model for aeroelastic response to gust excitation. In *SciTech 2019 Forum*, page 2031. AIAA, 2019. doi: 10.2514/6.2019-2031.

[3] B. Barzgaran, J. D. Quenzer, A. Zongolowicz, K. A. Hinson, M. Mesbahi, K. Morgansen, and E. Livne. Low-cost wind tunnel studies of gust alleviation control techniques. In *18th International Forum on Aeroelasticity and Structural Dynamics*, page 008. International Forum on Aeroelasticity and Structural Dynamics (IFASD), 2019. URL $\texttt{https://www.asdjournal.org/public/Proceedings/IFASD}_2019/IFASD - 2019 - 008.pdf$.

[4] B. Barzgaran and M. Mesbahi. Robust analysis and sensitivity design of model predictive control. *IFAC-PapersOnLine*, 53(2):7111–7116, 2020. doi: 10.1016/j.ifacol.2020.12.510.

[5] B. Barzgaran, J. D. Quenzer, M. Mesbahi, K. Morgansen, and E. Livne. Real-time model predictive control for gust load alleviation on an aeroelastic wind tunnel test article. *AIAA*, 2021. doi: 10.2514/6.2021-0500. AIAA Paper 2021-0500.

[6] K.Y. Ting, M. Mesbahi, and E. Livne. Aeroservoelastic wind tunnel evaluation of preview h2 and h-infinity gust load alleviation. *Journal of Guidance, Control, and Dynamics*, 46(11):2044–2062, 2023. doi: 10.2514/1.G007450.

[7] J.K. Berg, Kuang-Ying Ting, E. Livne, and K. Morgansen. Destabilize/stabilize approach to experimental active flutter suppression technology development. *Journal of Guidance, Control, and Dynamics*, 48(5):968–981, 2025. doi: 10.2514/1.G008589.

[8] K.-Y. Ting, J. Berg, M. Mesbahi, , and E. Livne. Aeroservoelastic wind tunnel evaluation of h$\infty$ active flutter suppression. *AIAA SCITECH Conference 2026*, January 2026. doi: 10.2514/6.2026-1058. AIAA Paper 2026-1058.

[9] F. Paltera. Flutter response to damage of composite aircraft control surfaces. Master's thesis, University of Washington Mechanical Engineering Department M.S.M.E. Dissertation, 2008.

[10] M. Noble. Nonlinear aeroelastic behavior of tail / rudder systems with freeplay and actuator failure. Master's thesis, University of Washington William E. Boeing Department of Aeronautics and Astronautics M.S.A.A. Dissertation, 2013.

[11] E. Rishel. Aeroelasticity of nonlinear tail / rudder systems with freeplay. Master's thesis, University of Washington William E. Boeing Department of Aeronautics and Astronautics M.S.A.A. Dissertation, 2015.

[12] Tyler Mundt. Development of an active aeroelastic continuous trailing edge wind tunnel wing model for drag and gust load minimization. Master's thesis, University of Washington, 2019.

[13] J. Berg, K.-Y. Ting, T.J. Mundt, M. Mor, E. Livne, and K. Morgansen. Exploratory wind tunnel gust 1. alleviation tests of a multiple-flap flexible wing. *AIAA Journal*, January 2022. doi: 10.2514/6.2022-2488. AIAA Paper 2022-2488.

[14] C.J. Forte, N.T. Nguyen, J. Berg, K.-Y. Ting, and L. Livne. Hamiltonian gust load alleviation control with adaptive gust estimation: Analy-

sis and wind tunnel test correlation. *AIAA Journal*, January 2026. URL https://doi.org/10.2514/6.2026-2895. AIAA Paper 2026-2895.

[15] Eli Livne. Aircraft active flutter suppression: State of the art and technology maturation needs. *Journal of Aircraft*, 55(1):410–452, 2018.

[16] S. Ricci, F. Toffol, A. De Gaspari, L. Marchetti, F. Fonte, L. Riccobene, P. Mantegazza, J. Berg, E. Livne, and K. Morgansen. Wind tunnel system for active flutter suppression research: Overview and insights. *AIAA Journal*, 60:6692–6714, October 2022. doi: 10.2514/1.J061985.

[17] Patrick S. Heaney and John F. Quindlen. *Overview of the Integrated Adaptive Wing Technology Maturation Wind-Tunnel Test Objectives*. AIAA, 2024. doi: 10.2514/6.2024-2509. URL https://arc.aiaa.org/doi/abs/10.2514/6.2024-2509.

[18] John F. Quindlen, Patrick S. Heaney, Daniel Ortega, Gregory J. Clark, Heather S. Hussain, Patrick J. Bentley, David A. Coulson, Ian M. Giles, Garrett McHugh, Jennifer L. Pinkerton, James M. Ramey, and William L. Stevens. *Summary of the Integrated Adaptive Wing Technology Maturation Wind Tunnel Tests of a High Aspect Ratio Commercial Transport Aircraft*. AIAA, 2026. doi: 10.2514/6.2026-1652. URL https://arc.aiaa.org/doi/abs/10.2514/6.2026-1652.

[19] John David Anderson. *Aircraft performance and design*. McGraw-Hill, 1st edition, 1999. ISBN 978-0070019713.

[20] B. Sarıgöl, A.F. LaFranchi, E. Livne, and K. Morgansen. Aeroservoelastic math modeling - a comparison of various analytical and test data based approaches. *AIAA SCITECH 2027 Forum*, January 2027. to be presented at the AIAA SciTech2027 Forum, January 2027.

[21] A.F. LaFranchi, B. Sarigol, R. Johnson, J. Berg, K. Morgansen, and E. Livne. Development and system identification of the uw's marge ii aeroservoelastic wind tunnel model and gust generation system. *AIAA SCITECH 2027 Forum*, January 2027. to be presented at the AIAA SciTech2027 Forum, January 2027.

[22] Robert K. Tischler, Mark B.and Remple. *Aircraft and Rotorcraft System Identification*. AIAA, 2006. ISBN 978-1-56347-837-6.

# Appendix A

# STATIC MARGIN CALCULATIONS

*Wing Geometry Metrics*

$$\text{Wingspan } b_w = 2 \times 29.036 \text{ in} = 58.072 \text{ in} = \mathbf{1.4750} \text{ m}$$

$$\text{MAC} = 8.465 \text{ in} = \mathbf{0.2150} \text{ m}$$

$$\text{Wing Area } S_w = 1.4750 \text{ m} \times 0.2150 \text{ m} = \mathbf{0.3171} \text{ m}^{\mathbf{2}}$$

$$AR_w = \frac{b_w}{\text{MAC}} = \frac{1.4750}{0.2150} = \mathbf{6.8605}$$

$$\text{Aerodynamic Center } X_{ac,w} = 0.25 \times 0.2150 \text{ m} = \mathbf{0.0538} \text{ m} \quad \text{(from leading edge)}$$

*Wing Lift Curve Slope ($a_w$)*

Applying Prandtl's lifting-line framework under subsonic compressible flow conditions ($\beta = \sqrt{1 - M^2} \approx 1.0$):

$$a_w = \frac{a_0}{\beta + \frac{a_0}{\pi \cdot AR_w}} = \frac{5.86}{1.0 + \frac{5.86}{\pi \times 6.8605}} = \frac{5.86}{1.0 + 0.2719} = \mathbf{4.6073} \text{ rad}^{-\mathbf{1}} \tag{A.1}$$

*Downwash Gradient ($\frac{d\epsilon}{d\alpha}$)*

Applying Prandtl's lifting-line theory again, for simplicity:

$$\frac{d\epsilon}{d\alpha} = \frac{2 \cdot a_w}{\pi \cdot AR_w} = \frac{2 \times 4.6073}{\pi \times 6.8605} = \frac{9.2146}{21.5529} = \mathbf{0.4275} \tag{A.2}$$

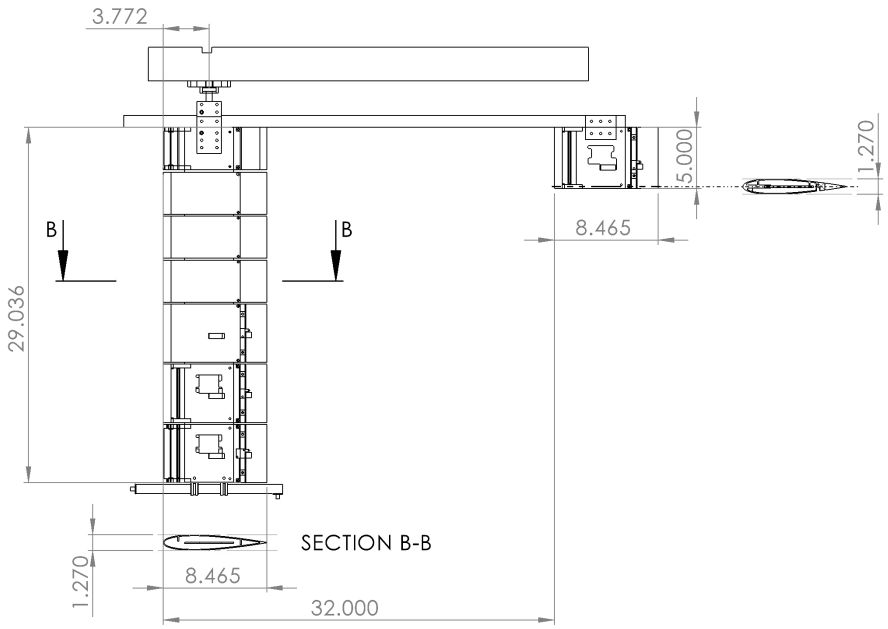



Figure A.1: MARGE-II Assembly Aerodynamic Dimensions

*Original Unstable Input Geometry & Volume Metrics*

$$\text{Tail Span } b_t = 2 \times 5 \text{ in} = 10 \text{ in} = \mathbf{0.2540} \text{ m}$$

$$\text{Tail Chord } c_t = 8.465 \text{ in} = \mathbf{0.2150} \text{ m}$$

$$\text{Tail Area } S_t = 0.2540 \text{ m} \times 0.2150 \text{ m} = \mathbf{0.0546} \text{ m}^\mathbf{2}$$

$$\text{Tail Aspect Ratio } AR_t = \frac{0.2540}{0.2150} = \mathbf{1.1814}$$

$$\text{Tail Arm } L_t = \mathbf{0.8128} \text{ m}$$

$$\text{X cg driven by pivot point: } X_{CG} = \mathbf{0.0958} \text{ m}$$

*Tail Volume Coefficient ($V_h$)*

$$V_h = \frac{S_t \times L_t}{S_w \times \text{MAC}} = \frac{0.0546 \times 0.8128}{0.3171 \times 0.2150} = \frac{0.04438}{0.06818} = \mathbf{0.6510} \tag{A.3}$$

*Tail Lift Slope via Helmbold Approximation ($a_t$)*

Apply Helmbold's Lift Slope Approximation for low-aspect-ratio straight wing in subsonic compressible flow:

$$a_t = \frac{a_0 \cdot AR_t}{2 \cdot AR_t + \sqrt{4 \cdot AR_t^2 + \left(\frac{a_0}{\pi}\right)^2 \cdot AR_t^4 \cdot \beta^2}} \tag{A.4}$$

$$a_t = \frac{5.86 \times 1.1814}{2(1.1814) + \sqrt{4(1.1814)^2 + \left(\frac{5.86}{\pi}\right)^2 \times (1.1814)^4}} \tag{A.5}$$

$$a_t = \frac{6.9230}{2.3628 + \sqrt{5.5828 + 6.7787}} = \frac{6.9230}{5.8787} = \mathbf{1.1776}\ \text{rad}^{-\mathbf{1}} \tag{A.6}$$

*Neutral Point ($X_{NP}$) & Static Margin (SM)*

$$X_{NP} = X_{ac,w} + \text{MAC} \times \left[V_h \cdot \frac{a_t}{a_w} \cdot \left(1 - \frac{d\epsilon}{d\alpha}\right)\right] \tag{A.7}$$

$$X_{NP} = 0.0538 + 0.2150 \times \left[0.6510 \times \frac{1.1776}{4.6073} \times (1 - 0.4275)\right] \tag{A.8}$$

$$X_{NP} = 0.0538 + 0.2150 \times [0.0953] = \mathbf{0.0743}\ \text{m} \tag{A.9}$$

$$\text{SM} = \frac{X_{NP} - X_{CG}}{\text{MAC}} = \frac{0.0743 - 0.0958}{0.2150} = -\mathbf{10.00}\% \tag{A.10}$$

After the adjustments described in the Pitch Instability Discussion section (moving the wing forward by 1.25 inches, and extending the tail span by 2 inches from their locations in Figure A.1), the following calculations show the estimate for MARGE-II's new static margin:

*Revised Input Geometry & Volume Metrics*

$$\text{Revised Tail Span } b_t = 2 \times 7 \text{ in} = 14 \text{ in} = \mathbf{0.3556} \text{ m}$$

$$\text{Tail Chord } c_t = 8.465 \text{ in} = \mathbf{0.2150} \text{ m}$$

$$\text{Tail Area } S_t = 0.3556 \text{ m} \times 0.2150 \text{ m} = \mathbf{0.0765} \text{ m}^{\mathbf{2}}$$

$$\text{Revised Tail Aspect Ratio } AR_t = \frac{0.3556}{0.2150} = \mathbf{1.6540}$$

$$\text{Revised Tail Arm } L_t = 0.8128 \text{ m} + (1.25 \text{ in} \times 0.0254) = \mathbf{0.8445} \text{ m}$$

$$\text{Revised X cg } X_{CG} = 0.0958 \text{ m} - (1.25 \text{ in} \times 0.0254) = \mathbf{0.0640} \text{ m}$$

*Revised Tail Volume Coefficient ($V_h$)*

$$V_h = \frac{S_t \times L_t}{S_w \times \text{MAC}} = \frac{0.0765 \times 0.8445}{0.3171 \times 0.2150} = \frac{0.06460}{0.06818} = \mathbf{0.9475} \tag{A.11}$$

*Revised Tail Lift Slope via Helmbold Approximation ($a_t$)*

$$a_t = \frac{5.86 \times 1.6540}{2(1.6540) + \sqrt{4(1.6540)^2 + \left(\frac{5.86}{\pi}\right)^2 \times (1.6540)^4}} \tag{A.12}$$

$$a_t = \frac{9.6924}{3.3080 + \sqrt{10.9429 + 26.0402}} = \frac{9.6924}{9.3894} = \mathbf{1.0323} \text{ rad}^{\mathbf{-1}} \tag{A.13}$$

*Revised Neutral Point ($X_{NP}$) & Static Margin (SM)*

$$X_{NP} = X_{ac,w} + \text{MAC} \times \left[ V_h \cdot \frac{a_t}{a_w} \cdot \left(1 - \frac{d\epsilon}{d\alpha}\right) \right] \tag{A.14}$$

$$X_{NP} = 0.0538 + 0.2150 \times \left[ 0.9475 \times \frac{1.0323}{4.6073} \times (1 - 0.4275) \right] \tag{A.15}$$

$$X_{NP} = 0.0538 + 0.2150 \times [0.1216] = \mathbf{0.0799} \text{ m} \tag{A.16}$$

$$\text{SM} = \frac{X_{NP} - X_{CG}}{\text{MAC}} = \frac{0.0799 - 0.0640}{0.2150} = +\mathbf{7.40}\% \tag{A.17}$$